

A Branching Ratio Measurement of the  
Charmless Hadronic Decay  $B^+ \rightarrow \rho^0 \pi^+, \rho^0 \rightarrow \pi^+ \pi^-$   
Using the BaBar Detector

Richard Penny



Experimental Particle Physics Group  
School of Physics & Astronomy  
University of Birmingham UK

June 2004

A thesis submitted to the University of Birmingham  
for the degree of Doctor of Philosophy

## Abstract

An analysis of the  $B^+$  decay mode to  $\rho^0\pi^+$  with subsequent decay  $\rho^0 \rightarrow \pi^+\pi^-$  has been undertaken. Data consists of  $88.9 \times 10^6$   $B^+B^-$  pairs produced in the BaBar detector by the PEP-II collider at Stanford Linear Accelerator Center during the period 1999-2002. A full selection process for these events from all data allows measurement of the branching fraction

$$Br[B^+ \rightarrow \rho^0\pi^+, \rho^0 \rightarrow \pi^+\pi^-] < (10.22 \pm 2.00 \pm 4.22) \times 10^{-6}$$

including charge conjugate states. This corresponds to 179 observed events, however the 90% confidence level upper limit for the  $B \rightarrow \pi^+\pi^-\pi^+$  decay mode is equivalent to 30 of these events.

A search for direct CP violation via a charge asymmetry measurement  $A$  through the  $B^+ \rightarrow \rho^0\pi^+, \rho^0 \rightarrow \pi^+\pi^-$  and  $B^- \rightarrow \rho^0\pi^-, \rho^0 \rightarrow \pi^+\pi^-$  channels is also presented, although asymmetry measurement results are inconclusive owing to lack of statistics.

## Acknowledgements

The opportunity to present this thesis could not have been initialized without financial support from PPARC and the cooperation of the University of Birmingham in allowing the author to undertake a Ph.D. in particle physics. I am humbly grateful for the help of these two bodies for providing the foundation for an interesting and insightful experience in the world of cutting edge scientific research.

At an individual level, the greatest thanks must go to my supervisor Alan Watson whose combination of resilience, friendliness and willingness to help when faced with the oddest code behavior or misguided question sets a very high standard for any future mentor to follow. The other BaBar scientists at Birmingham have also all provided help upon request and for this I must thank them. Numerous other research staff and students in both SLAC and Birmingham have provided perhaps less in direct help, but their comradeship, enlightening conversation and general support have been most welcome.

Purely personal thanks throughout this Ph.D. are extended to friends and a stream of characters who all add colour and spice to life in their own particular way, ensuring that personal growth and academic growth have remained in balance. And finally I must thank my family for the love and support that has underpinned everything I have achieved in my educational life.

## Declaration

I hereby declare that no portion of this thesis has been previously presented to the University of Birmingham, or any other university as part of the requirements of a higher degree. The work presented in this thesis was conducted at the University of Birmingham and the Stanford Linear Accelerator Center in California. Contributions to the BaBar collaboration as a member since the year 2000 have been to ensure the smooth operation of the detector, analyze data, and provide quality assurance to ongoing analysis package developments.

# Contents

<b>1</b>	<b>Introduction</b>	
1.1	Historical Overview	10
1.2	The Standard Model	11
1.3	Applying the Standard Model to the Cosmos	12
1.4	Studying CP Violation in B Mesons	14
<b>2</b>	<b>Theory of CP Violation</b>	
2.1	Introduction	16
2.2	Defining the C, P and T Transformations	16
2.3	Considerations of CP Violation	18
2.4	Mixing	19
2.5	The Strange Affair of K Mesons	21
2.6	Universal Symmetries in C, P and T Violated	22
2.7	Mass and CP Eigenstates	25
2.8	The CKM Mixing Matrix	28
2.9	Unitarity Triangles	30
2.10	Measurements in B Meson Physics	31
2.11	Measuring the Unitarity Triangles	34
2.12	The BaBar Mission	36
<b>3</b>	<b>The BaBar Detector</b>	
3.1	A B Meson Factory	38
3.2	An Overview of the BaBar Detector	40
3.3	The Silicon Vertex Tracker	42

3.4	The Drift Chamber	45
3.5	The DIRC	48
3.6	The Electromagnetic Calorimeter	51
3.7	The Instrumented Flux Detector	53
3.8	The Trigger	56
<b>4</b>	<b>Method of Analysis</b>	
4.1	Introduction	59
4.2	Analysis Overview	60
4.3	Event Preselection	63
4.4	Track Selection	65
4.5	Particle Reconstruction	67
4.6	Event Shape Variables	69
4.7	Background Characterization	71
4.8	Selection Optimization	75
<b>5</b>	<b>Analysis Results</b>	
5.1	$B^+ \rightarrow \rho^0 \pi^+, \rho^0 \rightarrow \pi^+ \pi^-$ Initial Results	77
5.2	Selection Optimization	87
5.3	Background Events	94
5.4	Efficiency corrections	97
5.5	Calibration Checking	100
5.6	Estimation of Branching Fraction	104
5.7	Charge Asymmetry Measurement	106
5.8	Conclusion	107

## List of Figures

1. *Feynman diagrams illustrate the tree and penguin processes*
2. *Experimental setup used by Christenson et al. in CP violation discovery*
3. *The unitarity triangle with greatest relevance to B meson studies*
4. *A combinatorial triangle example for measuring  $\gamma$*
5. *B meson decay with W boson emission*
6. *B meson decay with penguin contribution*
7. *Layout of the PEP-II electron-positron collider facility, also known as the "B factory"*
8. *Plan view of magnet layout in interaction region with stretched vertical scale*
9. *Schematic layout of the BaBar detector*
10. *Cross-sectional view of the SVT along the beam axis*
11. *Cross-sectional view of the SVT across the beam axis*
12. *Side view of the drift chamber. Note dimensions are in mm*
13. *100 ns contours of equal ion drift times for an axial superlayer cell*
14. *Cellular layout of wires with sequential pattern of axial (A) and stereo (U,V) angled cells*
15. *Schematic diagram of the DIRC layout*
16. *A DIRC silica bar and imaging section*
17. *Longitudinal layout of an EMC section. Distances shown are in units of mm*
18. *Layout of the RPC modules in the barrel*
19. *A multi-hadron event as shown on the Level 3 trigger event display*
20. *Tree and penguin decay processes for  $B^+ \rightarrow \rho^0 \pi^+$*
21. *Penguin decay process for  $\rho^0 \rightarrow \pi^+ \pi^-$*
22. *Forward-striped and backward-striped regions indicates areas used for  $m_{ES}$  and  $\Delta E$  characterization respectively*
23. *The relevant optimization fits applied on the  $m_{ES}$  characterization region*
24. *The relevant optimization fits applied on the  $\Delta E$  characterization region*
25. *Multiplicity in on-resonance data events*
26. *Multiplicity in Monte Carlo events*

27.  $m_{ES}$  Monte Carlo distribution for initial set of cuts
28.  $\Delta E$  Monte Carlo distribution for initial set of cuts
29.  $\Delta E : m_{ES}$  plane for Monte Carlo with signal and blind boxes
30.  $|\cos \theta_{thr}|$  in Monte Carlo and data
31. Fisher discriminant in Monte Carlo and data
32. Resonant Mass in Monte Carlo and data
33. Helicity angle in Monte Carlo and data
34.  $m_{ES}$  upper sideband with Argus shape for on-resonance data
35.  $m_{ES}$  upper sideband with Argus shape for off-resonance data
36.  $m_{ES}$  lower sideband with Argus shape for on-resonance data
37.  $m_{ES}$  lower sideband with Argus shape for off-resonance data
38.  $m_{ES}$  combined upper and lower sidebands with Argus shape for on-resonance data
39.  $m_{ES}$  combined upper and lower sidebands with Argus shape for off-resonance data
40.  $\Delta E$  distribution fitted with first order polynomial for on-resonance data
41.  $\Delta E$  distribution fitted with first order polynomial for off-resonance data
42.  $m_{ES}$  upper sideband with Argus shape for optimized on-resonance data
43.  $m_{ES}$  upper sideband with Argus shape for optimized off-resonance data
44.  $m_{ES}$  lower sideband with Argus shape for optimized on-resonance data
45.  $m_{ES}$  lower sideband with Argus shape for optimized off-resonance data
46.  $m_{ES}$  combined upper and lower sidebands with Argus shape for optimized  
on-resonance data
47.  $m_{ES}$  combined upper and lower sidebands with Argus shape for optimized  
off-resonance data
48.  $\Delta E$  distribution fitted with first order polynomial for optimized on-resonance data
49.  $\Delta E$  distribution fitted with first order polynomial for optimized off-resonance data
50.  $m_{ES}$  upper sideband with Argus shape for optimized continuum Monte Carlo
51.  $m_{ES}$  lower sideband with Argus shape for optimized continuum Monte Carlo
52.  $m_{ES}$  combined upper and lower sidebands with Argus shape for optimized continuum  
Monte Carlo

53.  *$\Delta E$  distribution fitted with first order polynomial for optimized continuum Monte Carlo*
54.  *$m_{ES}$  continuum Monte Carlo distribution for calibration channel*
55.  *$\Delta E$  continuum Monte Carlo distribution for calibration channel*
56.  *$m_{ES}$  on-resonance data distribution for calibration channel*
57.  *$\Delta E$  on-resonance data distribution for calibration channel*
58.  *$\Delta E : m_{ES}$  calibration channel plane for Monte Carlo*
59.  *$\Delta E : m_{ES}$  calibration channel plane for on-resonance data*
60.  *$\Delta E$  vs.  $m_{ES}$  distribution plot for unblinded on-resonance data*

# Chapter 1

## Introduction

### 1.1 Historical Overview

The first recorded suggestion that matter may consist of separate particles was made in the 5th century BC, probably by Leucippus of Miletus. His pupil, Democritus, adopted the now commonly used word atom from the Greek *atomos* meaning indivisible. John Dalton (1766—1844) revived the word at the start of the 19th century and provided a scientific basis for this simple Greek idea; Dalton suggested that the atom was the invisible particle that takes part in chemical reactions. This view of separate indivisible building blocks was overturned in 1897 by J. J. Thompson's discovery that "atoms" could 'emit' smaller, negatively charged particles, which are known as electrons. The discovery gave a good indication that the atom had some internal structure, which was duly confirmed by Rutherford in 1911 with his famous interpretation of the gold foil-alpha particle scattering experiment. Results from this and later experiments determined the structure of the atom as a cloud of negatively charged electrons orbiting a densely packed nucleus of positive charge. This nucleus consists of positive protons equal in number to the orbiting electrons, and these constantly interact with a similar number of neutral neutron particles to stabilize the structure.

Physicists then turned their attention to investigating the properties of the burgeoning number of particles that were being discovered experimentally in cosmic-ray and accelerator-based experiments. After many years from the start of this hunt there are now far more particles recorded than elements in the periodic table. Our understanding of the sub-atomic world has improved by many orders of magnitude: in the 1920's energies of a few electron-volts probed distances of some  $10^{-10}$  m, while today energies exceeding 100 million electron-volts have been used for distances

smaller than  $10^{-18}$  m. As of now, many of the properties of particles can be predicted with a very high level of accuracy by a collection of theories known as *the standard model*.

## 1.2 The Standard Model

The beauty of the Standard Model is in the fact that the most basic form can be expressed in a few sentences and diagrams. It is believed that the material world consists of 24 elementary spin  $\frac{1}{2}$  fermions. These include six leptons which can exist as free particles: the electron  $e$ , the muon  $\mu$  and the tau  $\tau$  carry unit negative electric charge and their respective neutrinos  $\nu$  are not charged. The neutrinos are generally treated as massless although recent experiments [1] have determined very small but unmistakably finite mass values. We arrange these particles into three generations shown below:

$$\begin{pmatrix} e^- \\ \nu_e \end{pmatrix} \quad \begin{pmatrix} \mu^- \\ \nu_\mu \end{pmatrix} \quad \begin{pmatrix} \tau^- \\ \nu_\tau \end{pmatrix}$$

There are 6 quarks (q) which are confirmed only to exist in bound combinations called baryons ( $qqq$ ) and mesons ( $q\bar{q}$ ). The up u, charm c and top t quarks all carry charge  $(+\frac{2}{3})$  while the down d, strange s and bottom b quarks carry  $(-\frac{1}{3})$  charge. They are also arranged into generations seen here where r, g, and b represent the 3 ‘colour charges’ red, green and blue respectively:

$$\begin{pmatrix} u \\ d \end{pmatrix}_{r,g,b} \quad \begin{pmatrix} c \\ s \end{pmatrix}_{r,g,b} \quad \begin{pmatrix} t \\ b \end{pmatrix}_{r,g,b}$$

Each particle also has a corresponding anti-particle with opposite quantum numbers. For example, the electron  $e^-$  has an anti-particle in the positron  $e^+$  and the up quark u has an anti-up  $\bar{u}$  quark. These generations of matter and anti-matter counterparts comprise the total of 24 elementary spin  $\frac{1}{2}$  fermions we currently believe to exist.

It is interesting to note that the six massive leptons and quarks fall into three generations as denoted by the parentheses, each successive generation simply being a heavier version of the previous one, with the same basic quantum numbers. Everyday matter only consists of the lightest generation. The fundamental reason behind both these observations is not known.

We postulate that the forces between these fundamental fermions are mediated by the exchange

of spin 1 gauge bosons. The electromagnetic force is mediated by the massless photon  $\gamma$ , the weak nuclear force by the massive  $W^\pm$  and  $Z^0$  bosons and the strong nuclear force by an octet of massless, 'coloured' gluons. The gravitational force is not accounted for within the standard model, mainly because the many theories that provide a remedy have yet to be experimentally validated. This omission is not considered to be significant here due to gravity's negligible strength at the level of energies currently attainable for study of the fundamental interactions of matter.

The interactions of these gauge bosons and the fundamental fermions are described within the framework of the standard model using a set of relativistically invariant theories known as gauge field theories. Twelve gauge bosons exist in the framework of the standard model. A single gauge boson couples to a pair of fermions, this gauge interaction not being affected by the fermion generation. Another type of interaction also exists and is known as the Yukawa interaction of two fermions coupling to a Higgs scalar doublet. It is the latter interaction that gives rise to quark masses through "spontaneous symmetry breaking." Physical systems can have equations of motion obeying particular symmetry transformations, but solutions to these equations exist that spontaneously break the symmetry and lead to changes in the physical system. Our observation of massive particles participating in a weak interaction requires present models to have a local gauge symmetry breaking of the Lagrangian. This breaking of the symmetry is attributed to the Higgs mechanism, whereby all massive particles are coupled to a scalar Higgs field with self-couplings that stabilize to a nonzero expectation value in the lowest energy state. The resulting transformation to a mass basis necessitates a diagonalization of the mass matrices in order to represent charged current interactions. At this point we can isolate the matrix which relates the weak eigenstates to mass eigenstates. CP violation is allowed in the Standard Model as the result of a non-trivial phase element in this mixing matrix, as we will see in the next chapter.

### **1.3 Applying the Standard Model to the cosmos**

It is widely believed that the universe began in what is known as the Big Bang approximately 13 billion years ago at our current best guess. Modern theories in particle physics predict all matter and antimatter should have been created in equal quantities. A particle and antiparticle that happen

to meet can annihilate and change into energy, a reverse process to their creation in the Big Bang.

Yet despite the theoretical symmetry of particles and antiparticles we can see only matter around us. Large quantities of antimatter cannot exist anywhere in the universe - if this were not the case we would see an energy emission from the matter-antimatter boundary. So what caused this imbalance in nature?

Physicists studying the effects of particle property operators in the 1960s began to recognize that not all particles exhibited the same properties as their antiparticles. The phenomenon of CP violation was first observed as a tiny effect in the decay of K mesons, particles which will be henceforth also referred to as kaons. A particle is transformed into its antiparticle and vice versa by the combination of a charge operator C that changes the polarity of a particles quantum numbers together with the Parity P operator that inverts spatial coordinates. If the laws of physics governing the CP particle $\Rightarrow$ antiparticle and CP antiparticle $\Rightarrow$ particle operations are not symmetric then an imbalance between matter and antimatter can arise. A violation of the CP symmetry is necessary to explain the dominance of matter that we see today.

Physicists believe that CP violation is 100 times bigger in B mesons than in kaons, and study of how these particles and their conjugates decay will lead to very precise measurements of the CP violation effect. B meson particles are heavier cousins of the kaons first seen to exhibit CP violation, and it is the many B decay modes being linked to quark mixing matrix elements with the b quark component that gives a greater asymmetry significance than found in the kaon system. The presence of the large CP phase in the mixing matrix element  $V_{tb}$  is also highly significant. Vast quantities of data are needed for a thorough study since many B meson decay modes used as measurements relating to the CKM matrix values have very small branching fractions, and the increase in sample sizes cause CP violation to become more tightly constrained by experiment [2].

The standard model allows for a degree of CP violation in the electroweak sector, although we believe that a larger factor is needed to account for the cosmological matter-antimatter asymmetry. A thorough study into CP violation will clearly push our understanding of the standard model to the limit and possibly beyond even that.

## 1.4 Studying CP violation in B Mesons

Physicists first discovered the bottom quark simultaneously with the  $\Upsilon$  resonance in 1977, when they found the  $\Upsilon$  meson to be a bound state of  $b\bar{b}$  bottom quarks [3]. B mesons contain a b quark and a light antiquark, with the B system having many decay modes. Likelihoods of particular decays can be measured and compared with their conjugate process to ascertain the degree of any CP violation effect, i.e. we have CP symmetry only when the likelihoods  $B(x \rightarrow yz) = B(\bar{x} \rightarrow \bar{y}\bar{z})$ . CP violation is accommodated in the Standard Model by a phase parameter within the CKM quark mixing matrix responsible for relating quark mass eigenstates to weak interaction eigenstates. The phase parameter arises from a non-equivalence of mass eigenstates and CP eigenstates in a three generation system whereby the number of degrees of freedom allow the consequence that one phase factor is irreducible after transitions. Many observables depend on this parameter, and the loosely constrained nature of the CKM matrix in turn implies that a number of different experiments can be undertaken to detect and constrain any measurement inconsistencies. The study of multiple B meson decay modes follows from the fact that many element amplitudes in the CKM matrix can be related to the branching fractions of particular B decay modes. We can furthermore use predictions on the relative strengths of different effects to check that separate processes in measuring  $\sin 2\beta$  give equivalent answers consistent with CKM matrix being the sole source of CP violation. We must look to new physics for explanations if our answers do not match.

The collision of  $e^-$  and  $e^+$  leptons at energies of 10.54 GeV in the centre-of-mass system has about a 30% chance of creating the  $\Upsilon(4S)$  resonance. This specific resonance will always decay to a  $B\bar{B}$  meson state. The  $B^+B^-$  or  $B^0\bar{B}^0$  pairs produced have very little momentum in the  $\Upsilon(4S)$  rest frame, a situation that is unfavourable for accurate measurement of any time-dependant observables. This problem is solved by making the colliding lepton beams have unequal energy, thus the subsequent  $\Upsilon(4S)$  will be moving in a lab rest frame and any decay products will travel a measurable distance before further decays.

Precision measurements of CP violation can arise from the particular amplitude sensitivities in the charmless hadronic B decays; these are modes when b quarks decay either to u quarks through emission of the W weak force carrier, or d or s quarks by means of penguin loops [4] where the W

boson recouples during a decay process. Example diagrams of the two processes are shown here:

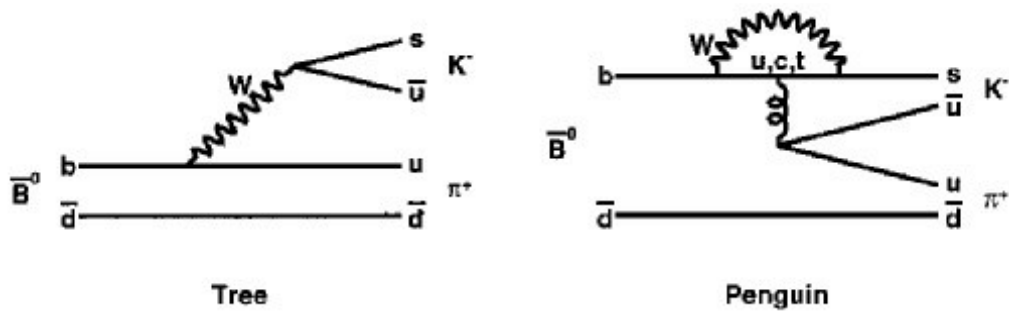


Figure 1: Feynman diagrams illustrate the tree and penguin processes

The primary importance of charmless hadronic B decays is in the suppression of their tree process amplitudes by the CKM matrix to a comparable level with the penguin process amplitude. Interference between these two amplitudes could lead to discovery of significant CP violation. Furthermore the penguin processes are poorly understood and charmless decays often previously unobserved, so results of studies should attract a wide level of interest. A major drawback for charmless studies is the high likelihood of substantial penguin processes, which in turn introduces uncertainty to any interpretation of measured asymmetries.

The large theoretical uncertainties in some of the decay mechanisms and present lack of sufficient data mean that a good understanding of CP violation is still some years away. Nevertheless contemporary study of the relative branching fractions of charmless decay channels and any CP asymmetries that subsequently come to light will give important insights into decays. Furthermore, charmless B decay measurements will provide a test of models currently used as a basis for obtaining a number of quantitative details in our Standard Model theory of particle properties [2].

# Chapter 2

## Theory of CP Violation

### 2.1 Introduction

The origin of CP violation has been described as one of the two most important questions to be understood in particle physics, the other one being the origin of mass. After many years of hard work we are finally in a position to test the prediction of substantial CP violation being allowed in the weak interaction with 6 quarks and a unitary mixing matrix. A theoretical solution of the CP violation problem completely verified by experiments will affect the fabric of particle physics in a most profound way. The majority of theories in physics are fundamentally concerned with invariances within physical systems while these systems undergo symmetry transformations. We find conservation laws associated with any symmetries can be continuous or discrete, and these conservation laws have corresponding conserved quantum numbers. The three discrete symmetries of charge C, parity P and time reversal T play an essential part in our attempts to understand matter and anti-matter asymmetry through the effect of CP violation.

### 2.2 Defining the C, P and T Transformations

Although we touched on the C and P operators in the Introduction chapter, a formal definition of these transformations is a first step in any study of CP violation [5]. C, P and T are the three known fundamental discrete symmetry transforms. The charge conjugation operator C acting on a particle which is described by wave function  $|F(\vec{p}, \vec{s})\rangle$ , with  $\vec{p}$  and  $\vec{s}$  denoting the momentum and spin respectively, will change the particle into an antiparticle. Hence polarity of every internal quantum number (baryonic number, electric charge etc.) related to the particle becomes reversed while  $\vec{p}$  and  $\vec{s}$  remain untouched. We can thus express the process including a phase factor  $\eta_c$  in the following form:

$$C|F(\vec{p}, \vec{s})\rangle = \eta_c |\bar{F}(\vec{p}, \vec{s})\rangle.$$

Transformations of parity P change a space vector  $\vec{r}$  into  $-\vec{r}$ . As momentum  $\vec{p}$  is defined  $\vec{p} = m \frac{d\vec{r}}{dt}$ , the reversal of the  $\vec{r}$  sign will also reverse the sign of  $\vec{p}$ . However, orbital angular momentum  $\vec{L} = \vec{r} \times \vec{p}$  stays unchanged as does spin  $\vec{s}$  and internal numbers. Employing another phase factor  $\eta_p$  allows us to write:

$$P|F(\vec{p}, \vec{s})\rangle = \eta_p |F(-\vec{p}, \vec{s})\rangle.$$

The time reversal transformation T replaces time  $t$  with  $-t$ . Both momentum and spin have time components so they are also changed to opposite polarity. The phase factor in the transformation description is partially dependent on spin, hence the denotion  $\eta_T^s$ . We can now show the time reversal operation as

$$T|F(\vec{p}, \vec{s})\rangle = \eta_T^s |F(-\vec{p}, -\vec{s})\rangle^*.$$

The wave function in this case has been replaced by its complex conjugate as  $\psi(\vec{r}, t)$  and  $\bar{\psi}(\vec{r}, t)$  satisfy the spin 1/2 particle Dirac equation for fundamental particles

$$i\hbar \frac{\partial}{\partial t} \psi(\vec{r}, t) = H_d \psi(\vec{r}, t) = 0$$

for a free particle with Hamiltonian  $H_d = \frac{\hbar c}{i} \boldsymbol{\alpha} \cdot \vec{\mathbf{v}} + \beta mc^2$ , where  $a_x^2 = a_y^2 = a_z^2 = \beta^2 = 1$  and  $a_x, a_y, a_z$  and  $\beta$  anti-commute in pairs. We find  $\psi = Const \times e^{i\frac{p}{\hbar} \cdot r} \times e^{\pm iEt/\hbar}$ , though  $\psi(\vec{r}, -t)$  and  $\bar{\psi}(\vec{r}, -t)$  do not satisfy the Dirac equation. The space-time interpretation says that any momentum operator  $\mathbf{p} = \frac{\hbar}{i} \vec{\mathbf{v}}$  solutions will have time-progression  $e^{+iEt/\hbar}$  and time-reversal  $e^{-iEt/\hbar}$ , and so the Dirac equation is satisfied with a pair of space-reversed states in positive energy E. It is also worth noting that helicity  $\lambda = \frac{\vec{p}}{|\vec{p}|} \cdot \vec{s}$  can be seen to switch polarity under a P transformation yet remain unchanged by C and T operations following the above considerations of the wave function components.

Disregarding the phase factors, we find the principle of CPT invariance

$$CPT|F(\vec{p}, \vec{s})\rangle = |F(\vec{p}, \vec{s})\rangle$$

following from the considerations  $CP|F(\vec{p}, \vec{s})\rangle = T|F(\vec{p}, \vec{s})\rangle$  and  $|F(-\vec{p}, \vec{s})\rangle = |F(-\vec{p}, -\vec{s})\rangle^*$ .

## 2.3 Considerations of CP Violation

Any Hamiltonian operator  $H$  invariant under Lorentz transformations is believed to be invariant under the combined transformation CPT of Charge, Parity and Time reversal. Tests of CPT invariance generate high levels of interest since this invariance is a consequence of quantum mechanics and Lorentz invariance in local field theory, so evidence of CPT violation would therefore invalidate our belief in at least one of these foundations. Very sensitive testing of CPT invariance has been carried out by investigating the particle and antiparticle mass differences in the  $K^0$  system, and gives an upper limit of  $|(m_{\bar{K}^0} - m_{K^0})/m_{K^0}| < 10^{-18}$  [6]. This is a low limit indeed, and physicists have found no such indications of CPT violation. This important consequence of general symmetry in any field underpins quantum mechanics although it is not necessary that the individual C, P or T symmetries are exact. As of now we have no reason to doubt that each symmetry is conserved by only three of the four fundamental interactions in nature; strong nuclear force, electromagnetism and gravitation will respect C, P and T symmetry operations while the weak nuclear force does not have such universal consistency.

If a process is to undergo CP violation then it follows that time transformation T should be also violated to equal magnitude when assuming CPT is invariant. Time reversal  $e^{-iEt} \leftrightarrow e^{iEt}$  changes the Hamiltonian operator  $H$  into its complex conjugate  $H^*$ , and T is violated when  $H \neq H^*$ .

Consider a particle to have an eigenstate  $m - \frac{i\Gamma}{2}$  with  $m$  signifying the mass and  $\Gamma$  the decay width. Invariance of particle and antiparticle in a CPT transformation means mass and lifetime must remain the same, yet partial decay widths can vary with more than one decay channel present. Measuring differences in decay times of CP conjugate states will show the effects of CP violation. Interference amongst various terms of two amplitudes with different weak phases causes an asymmetry in the likelihood of a process for a decay and its conjugate. Such a CP violating mechanism is known as direct CP violation and may occur in both neutral and charged decays.

Each combination of fields and derivatives appearing in the Lagrangian will transform under a CP operation to its Hermitian conjugate. The coefficients of these expressions represent coupling constants or particle masses. If any of these quantities are complex then the coefficients of terms related to CP will be complex conjugates of each other. CP may not be symmetrical under the

Lagrangian in these cases, thus allowing a possibility of CP-violating effects such as rate differences between pairs of CP conjugate processes.

Two further types of CP violation arise from a neutral B meson oscillating between the mixed states of  $B^0$  and  $\bar{B}^0$  due to second order weak interactions. CP violation can be directly attributed to this mixing, whereby the two neutral mass eigenstates cannot be redefined into CP eigenstates. This manifestation is known as indirect CP violation. Interference between decays with and without mixing causes another form of CP violation, subject to the condition that the decay final states are common to both the  $B^0$  and  $\bar{B}^0$  mesons. These latter two examples of CP violation both have a measurable time dependent CP asymmetry.

In summary, there exist three possibilities for measuring CP violation in B systems:

- Directly from the decay of charged or neutral B mesons. Decay amplitudes  $A_f \neq \bar{A}_f$ . This does not involve mixing or time dependence.
- Indirectly from the  $B^0\bar{B}^0$  mixing. Neutral mass eigenstates are not equivalent to CP eigenstates. This measurement is time dependent.
- Indirectly from the interplay between the decay and the mixing of neutral B mesons.  $B^0 \rightarrow f$  and  $\bar{B}^0 \rightarrow f$ . This is also time dependent.

## 2.4 Mixing

Mixing occurs between two neutral pseudoscalar mesons of contrasting flavour. This group includes the B and K mesons. Pseudoscalars are field quantities that when subjected to parity transforms have negative parity, the time component magnitude being flipped while the spatial component stays the same. The pseudoscalar mesons capable of mixing will have their charged conjugate states retaining symmetry under a transition operation with any electromagnetic or strong force Hamiltonian, and hence the mesons remain stable. Weak force decays can violate flavour to cause asymmetric transitions, and in this case the conjugate states are not eigenstates of the total Hamiltonian. Two pseudoscalars  $A^0$  and  $\bar{A}^0$  of opposite flavour may have transitions to the same intermediate transition state  $T$  during a flavour-violating weak decay i.e.  $A^0 \Rightarrow T \Rightarrow \bar{A}^0$ . Such a transition process can change  $A^0$  into  $\bar{A}^0$  and is known as mixing.

The mixing process requires that the evolution of these states is written in a series. This series includes terms for the two pseudoscalar states and any intermediate states accessible to  $A^0$  and  $\bar{A}^0$ , all with coefficients containing a time factor relative to the start of mixing. This series can be expressed as shown with regards to time  $t$  :

$$|\psi(t)\rangle = a(t)|A^0\rangle + b(t)|\bar{A}^0\rangle \text{ along with intermediate states available to both pseudoscalars.}$$

Generally we are solely interested in the coefficients of the two pseudoscalar meson states, which are the only non-zero coefficients set at the start of mixing. Elimination of intermediate state considerations is achieved by setting the coefficient time factors beyond the time scale of all strong interactions. Now we consider the probability amplitudes  $A_0(t)$  and  $\bar{A}_0(t)$  of finding the state  $A^0$  and  $\bar{A}^0$  respectively from an evolving combinatorial state  $|\psi(t)\rangle$ ,

$$|\psi(t)\rangle = A_0(t)|A^0\rangle + \bar{A}_0(t)|\bar{A}^0\rangle.$$

If we consider a single particle at rest, we can rewrite the Schrödinger equation  $i\hbar \frac{d}{dt}|\psi(t)\rangle = H|\psi(t)\rangle$  as  $\frac{d}{dt}|\psi(t)\rangle = -i\frac{mc^2}{\hbar}|\psi(t)\rangle$ , and furthermore set both  $c$  and  $\hbar$  to unity. The eigenvector solution is  $|\psi(t)\rangle = e^{-imt}$ . Adding an particle instability factor where the decay is exponential gives us  $\frac{d}{dt}|\psi(t)\rangle = -im|\psi(t)\rangle - \frac{\Gamma}{2}|\psi(t)\rangle$ . The  $\frac{1}{2}$  fraction comes as a necessity of satisfying the probability condition  $\langle\psi|\psi\rangle \propto e^{-\Gamma t}$ .

Applying the Schrödinger equation  $i\hbar \frac{d}{dt}|\psi(t)\rangle = H|\psi(t)\rangle$  to the linear combination of the two states  $|A^0\rangle$  and  $|\bar{A}^0\rangle$  is shown thus

$$i\hbar \frac{d}{dt} \begin{pmatrix} A_0(t) \\ \bar{A}_0(t) \end{pmatrix} = \begin{pmatrix} \langle A^0|\hat{T}|A^0\rangle & \langle A^0|\hat{T}|\bar{A}^0\rangle \\ \langle \bar{A}^0|\hat{T}|A^0\rangle & \langle \bar{A}^0|\hat{T}|\bar{A}^0\rangle \end{pmatrix} \begin{pmatrix} A_0(t) \\ \bar{A}_0(t) \end{pmatrix}$$

where  $\hat{T}$  is the weak interaction transition operator to some transition state between  $A^0$  and  $\bar{A}^0$ . Strong or electromagnetic transition operators on corresponding charged conjugate states are symmetric and would give matrix elements equivalent to zero.

CPT conservation imposes the constraint that the mass and lifetime of both states are equal. This effectively means that diagonal terms of the above matrix are equal, and we can regroup the matrix elements in question into a Hermitian and non-Hermitian combination.

Thus the matrix describing the Hamiltonian in the two state linear combination can be rewritten as  $H = M - \frac{i\Gamma}{2}$ ,  $M$  and  $\Gamma$  being the mass and decay width matrices respectively.

The two coupled modes can be decoupled by treating  $|A^0\rangle$  and  $|\bar{A}^0\rangle$  as linear combinations and diagonalizing the  $2 \times 2$  matrix. Introducing these matrices will give rise to the two mass eigenstate solutions of the Hamiltonian,  $|\psi_+\rangle = p|A^0\rangle + q|\bar{A}^0\rangle$  and  $|\psi_-\rangle = p|A^0\rangle - q|\bar{A}^0\rangle$  with the condition  $|p|^2 + |q|^2 = 1$ .

If we assume CP symmetry in the two state Hamiltonian then the non-diagonal matrix entries are equivalent, and it follows  $p = q = \frac{1}{\sqrt{2}}$ .

## 2.5 The Strange Affair Of K Mesons

We will look at CP violation possibilities first in the simplified context of K mesons. The formalisms for K and B systems are generally the same, with the exception being the higher significance lifetime difference between the Kaon eigenstates. Studies of the *K* meson system are responsible for many of the standard model ideas which we take for granted today including the realization of parity violation, quarks and the quark flavour concept. The profound discovery of CP violation stems from K meson studies, with the implied requirements leading to predictions of the 3<sup>rd</sup> generation top and bottom quarks.

K mesons were discovered in cosmic radiation, and their decays first fully observed in cloud chamber pictures. Such reactions as  $K^0 \rightarrow \pi^+\pi^-$  and  $K^\pm \rightarrow \pi^\pm\nu$  clearly showed the K particle comes both in neutral and charged versions.

Since the 1950's K mesons have been produced at accelerators, and the physicists studying pictures of the nuclear interactions produced found a small number of particles which decay over several centimetres in every thousand interactions. If we assume these particles travel about 3 cm from relativistic and lifetime considerations, their lifetime is of the order of  $10^{-10}$  seconds which is typical of weak interactions. We conclude that the decay of K particles is weak while the production is via the strong force. This is very curious since pions and nucleons appear both at the beginning and at the end of the process. This strange property of *K* mesons and other particles known as hyperons led to the introduction of a new additive quantum number, the strangeness *S*. Strangeness is conserved in strong interactions, while a first order weak interaction can induce transitions where the value of strangeness is changed by one unit.

Today we describe these properties in terms of quarks with different “flavours”, first suggested in 1964 independently by Gell-Mann and Zweig who reformulated the SU(3) flavor to approximate global symmetry. The “normal particles” are bound states of quarks: the  $q\bar{q}$  mesons, or  $qqq$  baryons.

K mesons contain a strange quark,  $s$  as follows:

$$K^0 = d\bar{s} \text{ and } K^+ = u\bar{s} \text{ have strangeness } S = +1$$

$$\bar{K}^0 = \bar{d}s \text{ and } K^- = \bar{u}s \text{ have strangeness } S = -1$$

The assignment of negative strangeness to the  $s$  quark is arbitrary but maintains the original assignment of positive strangeness for  $K^0$  and  $K^+$ , and negative strangeness for  $\bar{K}^0$ ,  $K^-$  and the most prominent of the hyperons. An important consequence of the fact that K mesons carry strangeness is that the  $K^0$  and  $\bar{K}^0$  mesons can be seen as distinct particles. For example, consider the charge conjugation operator C acting on the K meson eigenstates;

$$C|K^0\rangle = |\bar{K}^0\rangle \text{ and } C|\bar{K}^0\rangle = |K^0\rangle$$

as expected, while a strangeness S operation gives

$$S|K^0\rangle = |K^0\rangle \text{ and } S|\bar{K}^0\rangle = -|\bar{K}^0\rangle$$

An experiment which shows an observable difference between the  $K^0$  and  $\bar{K}^0$  particles is the process  $p\bar{p} \rightarrow \pi^- K^+ \bar{K}^0$  where the  $\bar{K}^0$  mesons in turn produce  $\Lambda$  hyperons detectable due to processes such as scattering, while the  $K^0$  particles generated from  $p\bar{p} \rightarrow \pi^+ K^- K^0$  do not lead to production of such hyperons.

## 2.6 Universal Symmetries in C, P and CP Violated

The invariance principle of charge and parity conjugation hold for the strong and electromagnetic interactions, but in weak processes we find a different story involving the neutrino. Charge and parity violation observations follow when the neutrino is considered as an approximately massless particle with no frameboost and hence has handedness as a Lorentz invariant property. Handedness results from choosing an axis in space and projecting particle spin onto it to give one of two possible outcomes. Using the preferred direction of the neutrino velocity we may find a spin component in the same direction upon which we then label the neutrino as

right-handed. Similarly an absolute spin component onto the opposite direction of a velocity vector signifies a left-handed neutrino. The charge conjugation operation C will change a left-handed spin neutrino into a left-handed spin antineutrino and right-handed neutrino to a right-handed antineutrino as expected. Yet we do not witness processes that involve right handed-neutrinos or left-handed antineutrinos. So it is clear that charge conjugation symmetry does not apply universally within weak processes. An absence of right-handed spin antineutrinos and left-handed spin neutrinos in particular decays show individual C and P violation respectively. Nevertheless the combined CP conservation holds.

We further find the strong interactions conserve strangeness while the weak interactions do not. In fact, not only do they violate the strangeness quantum number S with  $\Delta S = 1$  and parity as seen below, they also violate charge conjugation C. The symmetry of C is seen to be experimentally conserved in strong and electromagnetic interactions, yet we witness the environment around us to be made of matter and this fact appears to be a consequence of C violation during some time in the evolution of the universe.

Parity violation was initially observed through the so-called  $\tau - \theta$  decay modes of K mesons where the different decay processes were first thought to originate from different particles. It should be noted that the  $\tau$  here is not the heavy lepton introduced in chapter one, but rather a postulated neutral particle which decays into three pions in a process which we describe today as  $K_L^0 \rightarrow \pi^0 \pi^+ \pi^-$  with parity P=-1. The  $\theta$  refers to another postulated neutral particle which decays into a pair of charged pions, which we would write as  $K_S^0 \rightarrow \pi^+ \pi^-$  with P=1. The question of the day was whether these two particles were the same particle with two decay modes, or two different ones. Differing lifetimes of the  $\tau$  and  $\theta$  favoured a two particle explanation. Also if they were the same particle, how could the two different final states have opposite parity?

The solution of this puzzle was not apparent until Dalitz introduced an argument which enabled determination of the  $\tau$  particle spin by looking at the decay distribution of the three pions in a “Dalitz” (or phase space) plot. The result was consistent with  $\vec{L} + \vec{S} = \vec{J} = 0$ . The spin of the  $\theta$  was inferred to be zero because it did not generally decay into a pion and a photon (since a photon cannot be emitted in a  $0 \rightarrow 0$  spin transition).

Two of the principal decay modes for neutral kaons are to two or three pions. The properties of

the neutral two and three pion systems with zero total angular momentum are given as follows, with  $\ell=0, 1, 2, \dots$  where  $\ell$  is the angular momentum of the charged pions in their centre of mass.

$\pi^+\pi^-, \pi^0\pi^0$  have  $P=+1, C=+1$  and combined (multiplicative)  $CP=+1$

$\pi^+\pi^-\pi^0$  have  $P=-1, C=(-1)^\ell$  and  $CP=\pm 1$

$\pi^0\pi^0\pi^0$  have  $P=-1, C=+1$  and  $CP=-1$

States with  $\ell > 0$  are suppressed by the angular momentum barrier. Bose statistics requires that  $\ell$  is even for any identical pion pair in the last process considered above. Note that the two pion and three pion states have opposite parity and hence we see parity violation in the CP eigenstates of the neutral Kaon. Investigations into cobalt 60 beta decay during the late 1950's then clearly established the phenomenon of parity violation. C.S. Wu et al. [7] forced cobalt nuclei to spin in a clockwise direction (as viewed from above) via a downward magnetic field and noted that electron emissions generally travelled in the upward direction. A mirror-image of a parity conserving experiment should have shown the cobalt nuclei spinning anti-clockwise as a result of the magnetic field pointing upwards and electrons emitted preferentially downwards. The experimentalists observed that electrons still preferred to travel up, therefore constituting a violation of parity. Nevertheless every time parity conservation was violated, the charge conjugation rule of changing each particle into its own antiparticle also happened to be violated.

For some years after the discovery that C and P are violated in the weak interactions, there was no suspicion that CP might not be conserved. Nevertheless CP violation was unexpectedly discovered in 1964 by Christenson et al.[8] through observing the decay  $K_L \rightarrow \pi^+\pi^-$ . The experiment was conceptually very simple as seen in figure 2;

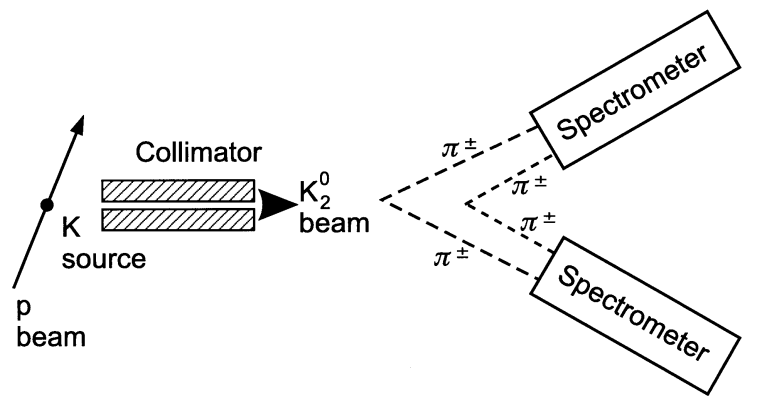


Figure 2: Experimental setup used by Christenson et al. in CP violation discovery.

A  $K_L$  beam passed through a long collimator and decays in an empty space, with the decay products viewed by spark chambers and scintillation hodoscopes in the spectrometers. Two pion decay modes are distinguished by the reconstructed invariant mass  $M_\pi$  and the direction  $\theta$  of their resultant momentum vector relative to the beam. A number of events were almost exactly collinear with the beam, demonstrating for the first time that  $K_L$  decayed into two pions and thus CP was shown to be violated! There is a single two pion decay found for every thousand three pion decays, and the CP violating decay  $K_L \rightarrow \pi^0\pi^0$  was also observed later.

## 2.7 Mass And CP Eigenstates

Neutral B and K mesons both have different neutral states to describe physical processes: the two flavour eigenstates are a formulation for particle production and decay, while the Hamiltonian eigenstates are used for states involving definite mass and lifetimes that propagate through space. The weak interaction manifestly violates the combined CP symmetry and causes the mass eigenstates to be different from CP eigenstates, providing an opportunity for matter and anti-matter asymmetry. We illustrate by firstly assuming that CP is a symmetry of our world. Thus define an arbitrary phase by:

$$CP|K^0\rangle = |\bar{K}^0\rangle$$

and then further define the simultaneous mass and CP eigenstates as follows

$$|K_1\rangle = \frac{|K^0\rangle + |\bar{K}^0\rangle}{\sqrt{2}} \text{ with CP} = +1, |K_2\rangle = \frac{|K^0\rangle - |\bar{K}^0\rangle}{\sqrt{2}} \text{ with CP} = -1$$

The CP eigenstates above follow from the observation of  $K^0 \rightarrow \pi^+\pi^- \rightarrow \bar{K}^0$  and vice versa.  $K_1$  and  $K_2$  are also the physical mass eigenstates undergoing the CP operation with outcome  $CP|K_1\rangle = |K_1\rangle$  and  $CP|K_2\rangle = -|K_2\rangle$ .

While  $K^0$  and  $\bar{K}^0$  are degenerate states in mass, as required by CPT invariance, the weak interactions induce second order  $K^0 \leftrightarrow \bar{K}^0$  transitions i.e. two weak interactions in the same process. This in turn induces a small mass difference between  $K_1$  and  $K_2$  which we will label as  $\Delta m$ . The  $K_1$  mass is the expectation value of  $\langle K_1|H|K_1\rangle$  using the  $K_1$  definition found in the previous paragraph. Using the analogous result for  $K_2$ , we find

$$m_1 - m_2 = \langle K^0|H|\bar{K}^0\rangle + \langle \bar{K}^0|H|K^0\rangle$$

describes the mass difference due to  $K^0 \leftrightarrow \bar{K}^0$  transitions induced by a  $\Delta S = 2$  interaction.

If the total Hamiltonian conserves CP i.e. we have the condition that  $[H, CP] = 0$ , the decays of  $K_1$  and  $K_2$  states must conserve CP. Thus the  $K_1$  particles with CP = +1 must decay into two pions (or three pions in a  $\ell = 1$  state, surmounting a particular angular momentum barrier), while the  $K_2$  particles with CP = -1 can only decay into three pion final states. The energy available in the two pion decay mode is approximately 220 MeV while that for the three pion decay mode is only about 90 MeV. Therefore phase space considerations lead the lifetime of the  $K_1$  to be much shorter than that of the  $K_2$ .

The mass eigenstates  $K_1$  and  $K_2$  evolve in a vacuum and in their rest frame according to the time-dependent Heisenberg equation  $i \frac{d}{dt} \Psi = H \Psi = M \phi$ , where M is the complex mass  $M_{1,2} = m_{1,2} - \frac{i\Gamma_{1,2}}{2}$ . The state evolution is therefore given by:

$$|K_{1,2}, t\rangle = |K_{1,2}, t = 0\rangle e^{-im_{1,2}t - \frac{\Gamma_{1,2}}{2}t}$$

If the initial state has definite strangeness, for example as a  $K_0$  from the production process  $\pi^- p \rightarrow K^0 \Lambda^0$ , it must first be rewritten in terms of the mass eigenstates  $K_1$  and  $K_2$  which then evolve in time as described above. Since the K state amplitudes change phase differently with time due to different masses and decay rates, the pure  $S = 1$  state at  $t=0$  acquires an  $S = -1$  component at  $t > 0$ . The wave function at time t gives the corresponding intensity of  $K^0$  and  $\bar{K}^0$  which can be seen to exhibit oscillations whose frequency depends on the mass difference.

The appearance of  $\bar{K}^0$  particles from an initially pure  $K^0$  beam can be detected by the production of hyperons, according to various reactions. The  $K_L - K_S$  mass difference can therefore be obtained from the oscillation frequency. Pion decays from  $K^0$  and  $\bar{K}^0$  have differing distributions of intensity, and a plot of time-dependent asymmetry shows most systematics cancel. Residual differences in the two kaon states are then determined.

The placement of a piece of material in the path of a  $K_2$  beam allows regeneration of  $K_1$  particles, and interference between differently aligned regenerator beams will enable determination of the  $K_1$  and  $K_2$  mass difference. We can take the standard reaction  $\pi^- p \rightarrow K^0 \Lambda^0$  with the initial state wave function of the  $K_0$ ,  $\Psi(t = 0) = |K_0\rangle = \frac{|K_1\rangle + |K_2\rangle}{\sqrt{2}}$ .

The  $K_1$  component decays away quickly via the two pion decay modes, leaving a virtually pure

$K_2$  beam with equal  $K^0$  and  $\bar{K}^0$  components which interact differently in matter. For example, only the  $\bar{K}^0$  produces hyperons via strangeness conserving transitions. These different interactions cause  $K_1$  regeneration through greater absorption of  $\bar{K}^0$  to leave  $\Psi$  as a mixture of  $K_1$  and  $K_2$  again. The apparent rebirth of  $K_1$  particles emerging from the blocking material has an important property in that the  $K_1$  is produced at a non-zero angle to the incident  $K_2$  beam; regeneration on different nuclei in a regenerator material is incoherent while at zero degree the amplitudes from different nuclei add up coherently. The intensity for coherent regeneration depends on the  $K_1$  and  $K_2$  mass difference, and precision mass measurements show the ratio of coherent to diffraction regeneration from two or more regenerators and allows us to determine that the  $K_2$  meson is heavier than the  $K_1$  meson. The  $K_1$  and  $K_2$  amplitudes after regeneration are coherent and thus can interfere if CP is violated. We find  $K_2$  decays with the wrong CP eigenstates.

Since CP is violated in K decays, the mass eigenstates cannot be regarded as equivalent to CP eigenstates anymore and must be rewritten, assuming CPT invariance, as:

$$K_S = p|K^0\rangle + q|\bar{K}^0\rangle, \quad K_L = p|K^0\rangle - q|\bar{K}^0\rangle$$

with  $p \neq q$  to avoid equivalence with the CP eigenstates. Furthermore the unitarity condition  $p^2 + q^2 = 1$  must be satisfied.

CP violation can be described by the quantities  $\epsilon$  and  $\epsilon'$  as

$$\frac{p}{q} = \frac{1 + \epsilon}{1 - \epsilon}, \quad \frac{A(K_L \rightarrow \pi^+\pi^-)}{A(K_S \rightarrow \pi^+\pi^-)} = \epsilon + \epsilon' \quad \text{and} \quad \frac{A(K_L \rightarrow \pi^0\pi^0)}{A(K_S \rightarrow \pi^0\pi^0)} = \epsilon - 2\epsilon'$$

whereby the  $\epsilon$  observable provides a test of indirect CP violation with  $K_1$  CP states mixing and the  $\text{Re}(\epsilon'/\epsilon)$  measures the level of direct CP violation in a decay and depends on the channel, for example  $K \rightarrow \pi\pi$  decays.

A question arises whether CP is violated directly in  $K_0$  decays, i.e. is the  $|\Delta S|=1$  amplitude  $\langle \pi\pi|K_2 \rangle \neq 0$  or does CP violation have only one manifestation of introducing a small impurity of  $K_1$  in the  $K_L$  state, via  $K^0 \leftrightarrow \bar{K}^0$   $|\Delta S|=2$  transitions? Observation of the parameter  $\epsilon'$  being non-zero is proof of  $|\Delta S|=1$  direct CP violation, that is CP violating transitions with  $K_2 \rightarrow \pi\pi$  having a finite likelihood. Most observations of CP violation are examples of indirect  $|\Delta S|=2$  violation, due to  $K^0 \leftrightarrow \bar{K}^0$  transitions introducing a small CP impurity in the mass eigenstates  $K_S$  and  $K_L$ . The smallness of both  $\epsilon$  and  $\epsilon'$  mean most results and parameter values given earlier for  $K_1$  and  $K_2$  remain valid after the substitutions for  $K_S$  and  $K_L$  respectively.

The NA48 experiment performed at CERN [9] gives the value of the real part of  $\frac{\epsilon'}{\epsilon} = (23 \pm 6.5) \times 10^{-4}$ , indicating that direct CP violation definitely exists. CP violation has only been seen in  $K_L$  decays ( $K_L \rightarrow \pi\pi$  and semileptonic decays) because the necessary pure  $K_L$  beam is easy to produce. The approximately equal decay times of  $B_S$  and  $B_L$  means that no such beam decay CP measurement is plausible in the B system. However, if the picture of CP violation we have developed so far is correct, we can predict quite accurately the values of some decay branching ratios and the leptonic asymmetry. It is important to check such predictions experimentally to aid theoretical refinement. In order to test CP violation within the Standard Model it becomes clear the Kaon system alone is insufficient to give us a detailed representation, and the major role must be played by the numerous non-leptonic  $B$  meson decays.

## 2.8 The CKM Mixing Matrix

The observation that only a charged weak interaction current from  $|\Delta S|=1$  particle decays mixes the quark generations led to a conclusion that strong and weak interactions couple to different quark eigenstates. A  $2 \times 2$  unitary (that is,  $M^\dagger M = 1$ ) rotation matrix including a Cabibbo mixing angle  $\theta_c$  described quark mixing to four quark flavours [10]:

$$\begin{pmatrix} d' \\ s' \end{pmatrix} = V_{C\&GIM} \begin{pmatrix} d \\ s \end{pmatrix}, \text{ where } V_{C\&GIM} = \begin{pmatrix} V_{ud} & V_{us} \\ V_{cd} & V_{cs} \end{pmatrix} = \begin{pmatrix} \cos \theta_c & \sin \theta_c \\ -\sin \theta_c & \cos \theta_c \end{pmatrix}$$

Electroweak theory postulates the existence of four gauge fields with their respective force carriers in the form of vector bosons. Interplay with the carrier quanta gives rise to the four fundamental interactions seen in nature. It was the discovery of CP violation following on from the noted absence of strangeness changing neutral currents which inspired Kobayashi and Maskawa to expand the original  $2 \times 2$  matrix into  $3 \times 3$  dimensions [11]. A  $3 \times 3$  unitary matrix can have nine independent parameters (counting the real and imaginary parts of a complex element as two parameters). In this case there are six possible fermions involved in the charged weak processes and so we can have five relative phase transformations, thereby absorbing five of the nine parameters. This means that whereas the  $2 \times 2$  Cabibbo matrix has only one parameter, the  $3 \times 3$  CKM matrix has four independent parameters which cannot be chosen as zero values by a

redefinition of the fields. If the CKM matrix were real it would only have three independent parameters. Some of the elements may be complex, and it is this possibility that provides a mechanism for the violation of CP conservation as described near the start of this chapter. Three general conditions must be satisfied in order to get CP violation: two local amplitudes, a weak and a strong phase, and just one phase changes sign under a CP transformation.

An additional generation of quarks is also implied in the new matrix, and these are now known as the b and t quarks which match the 3<sup>rd</sup> generation  $\tau$  lepton-neutrino pair in the Standard Model.

Three generation quark mixing is described by the matrix operation

$$\begin{pmatrix} d' \\ s' \\ b' \end{pmatrix} = V_{CKM} \begin{pmatrix} d \\ s \\ b \end{pmatrix},$$

$$\text{with } V_{CKM} = \begin{pmatrix} C_{12}C_{13} & S_{12}C_{13} & C_{13}e^{-i\delta} \\ -S_{12}C_{23} - C_{12}S_{23}S_{13}e^{i\delta} & C_{12}C_{23} - S_{12}S_{23}S_{13}e^{i\delta} & S_{23}C_{13} \\ S_{12}S_{23} - C_{12}C_{23}S_{13}e^{i\delta} & -C_{12}S_{23} - S_{12}C_{23}S_{13}e^{i\delta} & C_{23}C_{13} \end{pmatrix}$$

In the above notation,  $C_{xy}$  represents  $\cos\theta_{xy}$  and analogously  $S_{xy}$  denotes  $\sin\theta_{xy}$ . Note there are three mixing angles, and also one phase angle we label here as  $\delta$ .

While a phase can be introduced in the unitary matrix  $V$  which mixes the quarks, the theory does not predict the magnitude of the effect (or indeed any of the angles). The constraint that the mixing matrix be unitary corresponds to the desire of having a universal weak interaction.

Our present knowledge of the magnitude limits of the  $V_{ij}$  elements is given below as a reference:

$$\text{Using the } V_{ij} \text{ notation } \begin{pmatrix} d' \\ s' \\ b' \end{pmatrix} = \begin{pmatrix} V_{ud} & V_{us} & V_{ub} \\ V_{cd} & V_{cs} & V_{cb} \\ V_{td} & V_{ts} & V_{tb} \end{pmatrix} \begin{pmatrix} d \\ s \\ b \end{pmatrix},$$

$$\begin{pmatrix} d' \\ s' \\ b' \end{pmatrix} = \begin{pmatrix} 0.9745 - 0.9757 & 0.219 - 0.224 & 0.002 - 0.005 \\ 0.218 - 0.224 & 0.9736 - 0.9750 & 0.036 - 0.047 \\ 0.004 - 0.014 & 0.034 - 0.046 & 0.9989 - 0.9993 \end{pmatrix} \begin{pmatrix} d \\ s \\ b \end{pmatrix}$$

The diagonal elements are close but definitely not equal to unity. If such were the case there could be no CP violation. However, if the  $\epsilon \neq 0$  CP violation is explained by the non-unity of the mixing matrix, then in general we expect  $\epsilon' \neq 0$ . It is difficult to determine the value of  $\epsilon'$ . A

fundamental task of experimental physics today is the determination of the four parameters of the CKM mixing matrix, including the phase which results in CP violation. The BaBar collaboration is undertaking such a task.

Wolfenstein parameterized the 3x3 mixing matrix in a convenient way which reflects more immediately our present knowledge of some element values and has the CP violating phase appearing in only two off-diagonal elements [12]. He noticed a rough geometrical pattern in the known values of the matrix elements;  $|V_{11,22,33}| \approx 1$ ,  $|V_{12,21}| \approx \lambda$ ,  $|V_{23,32}| \approx \lambda^2$ ,  $|V_{13,31}| \approx \lambda^3$ . The Wolfenstein *approximate* parameterization of the mixing matrix including up to  $\lambda^3$  terms is

$$V = \begin{pmatrix} V_{ud} & V_{us} & V_{ub} \\ V_{cd} & V_{cs} & V_{cb} \\ V_{td} & V_{ts} & V_{tb} \end{pmatrix} = \begin{pmatrix} 1 - \frac{1}{2}\lambda^2 & \lambda & A\lambda^3(\rho - i\eta) \\ -\lambda & 1 - \frac{1}{2}\lambda^2 & A\lambda^2 \\ A\lambda^3(1 - \rho - i\eta) & -A\lambda^2 & 1 \end{pmatrix}$$

$\lambda$  is the Cabibbo angle as seen before; a real number,  $\lambda = 0.2215 \pm 0.0015$  and describes mixing of s and d quarks.  $A$ , also real, is  $0.84 \pm 0.06$  and  $|\rho - i\eta| \sim 0.3$ . CP violation occurs only if  $\eta \neq 0$ , though  $\eta$  and  $\rho$  are not really known to any degree of confidence at the present time. The Wolfenstein representation is useful for relating CP violation to specific decay rates.

## 2.9 Unitarity Triangles

The unitarity condition  $V^\dagger V = 1$  contains the relations  $\sum_i V_{ij}^* V_{ik} = \sum_i V_{ji}^* V_{ki} = \delta_{jk}$  which means that if we take the products, term by term of any one column (row) element with the complex conjugate of another column (row) element, their sum is equal to zero. One relation among several requiring the sum of three complex quantities to disappear is  $V_{ud}V_{ub}^* + V_{cd}V_{cb}^* + V_{td}V_{tb}^* = 0$ . Geometrically such relations mean that the three terms are sides of a triangle in the complex plane; the sides in the particular equation quoted above being found to have similar magnitude and thus large (measurable) triangle angles. An illustration of the triangle is shown below, the openness of the angles indicating a large amount of CP asymmetry in the B meson system in contrast to the flatness of the other relational triangles. Each triangle base is given unit length, and we divide each triangle side by  $|V_{cd}V_{cb}^*|$  choosing a field convention where  $V_{cd}V_{cb}^*$  is real. This is used when discussing CP violation measurements in the B system such that the

triangle has a peak point at  $(\bar{\rho}, \bar{\eta}) = (1 - \frac{1}{2}\lambda^2)(\rho, \eta)$ .

$$\rho - i\eta = \frac{V_{ud} V_{ub}^*}{V_{cd} V_{cb}^*}$$

$$\frac{V_{td} V_{tb}^*}{V_{cd} V_{cb}^*} = 1 - \rho - i\eta$$

$$\frac{V_{cd} V_{cb}^*}{V_{cd} V_{cb}^*} = 1$$

Figure 3: The unitarity triangle with greatest relevance to B meson studies

$$\alpha = \text{Arg}\left(-\frac{V_{td}V_{tb}^*}{V_{ud}V_{ub}^*}\right), \quad \beta = \text{Arg}\left(-\frac{V_{cd}V_{cb}^*}{V_{td}V_{tb}^*}\right) \quad \text{and} \quad \gamma = \text{Arg}\left(-\frac{V_{ud}V_{ub}^*}{V_{cd}V_{cb}^*}\right)$$

The relations described that follow from the unitarity consideration  $V^\dagger V = 1$  show that triangle areas are equal regardless of mixing parameter choice, and CP violation is proportional to the area of these unitary triangles. Jarlskog [13] shows  $J = C_{12}C_{23}C_{13}^2 S_{12}S_{23}S_{13} \sin \delta$ , or in terms of the Wolfenstein parameters approximately  $J = A^2 \lambda^6 \eta$ , where  $\frac{J}{2}$  is the triangle area with size  $(2.7 \pm 1.1) \times 10^{-5}$  according to present knowledge [14]. An important constraint on the unitarity triangle is the  $\epsilon$  observable measurement which implies that the Wolfenstein parameter  $\eta$  has a positive value. Determinations of  $\text{Re}(\epsilon'/\epsilon)$  are highly intricate and beset by hadronic uncertainties, thus proving an unsuitable test for CP violation within the Standard Model. The  $\epsilon'$  parameter is found by measurements in a number of decay channels with particular mixing matrix elements. The acute smallness of the triangle area further illustrates why the  $\epsilon'$  experiments are so difficult despite the large value of the angles in the unitarity triangle, and thus the need for B-producing factories in order to study CP violation in the intricate B system.

## 2.10 Measurements in B Meson Physics

The 1977 discovery of the  $\Upsilon$  particle as a narrow resonance of mass  $9.5 \text{ GeV}/c^2$  was immediately taken as proof of the existence of the b quark, heralded by Kobayashi and Maskawa. The b quark has quantum number  $B = -1$ . The fourth resonance state of  $\Upsilon$  is barely above threshold for decaying exclusively into a charged or neutral pair  $B\bar{B}$ , the B mesons composed of  $b\bar{d}$ ,  $b\bar{u}$  and

their charge conjugate states. There is a complete analogy with charged and neutral kaons, including the characteristic that  $B^0$  and  $\bar{B}^0$  are not self-conjugate states. The fact that the  $\Upsilon(4S)$  decays only to such pairs was demonstrated by not finding low energy ( $\sim 50$  MeV) photons from  $B^*$  (the first excited state of B meson) decays, nor finding high-energy photons indicative of  $4S$  decaying directly into photons plus hadrons. The neutral  $B$  mesons are produced in the same state as the neutral Kaons, and can be used for CP studies in the B system once the short B lifetime problem is overcome.

In fact the B meson lifetime at  $10^{-12}s$  is found to be longer than the  $10^{-15}s$  that theory had predicted from several considerations. Couplings in weak decays show a relationship of  $\tau \propto m^{-5}$  for a particle with lifetime  $\tau$  and mass  $m$ ; furthermore the B lifetime is expected to be shorter than the D lifetime since the mass of the b quark gives a larger phase space for decay products. We can account for the lifetime difference between prediction and measurement when we contrast the quark mass eigenstate with its weak eigenstate, in which case the mixing matrix introduces an additional factor within calculations. This factor  $\frac{1}{|V_{cb}|^2}$  is responsible for the  $10^3$  lifetime increase, and from this we infer that  $|V_{cb}| \approx 0.032$  is approximately equal to the Wolfenstein parameter  $\lambda^2$ . The value of  $|V_{cb}|$  means that the sides of the unitarity triangle most relevant to the B system are comparable in size, allowing the potential of observing large CP violation effects through weak phases associated with the corresponding large triangle angles. Relevant CP-violating phases described by the CKM matrix occur in first order in the B meson system, while the CP violation in the K meson system is only accounted from higher order processes and thus CP violation will be less prominent in K decays. The hadronic uncertainties in relating CP violation parameters of the K system to CKM phases are greatly reduced or not present in the B meson system, and as such all recent progress in CP violation studies has used B mesons. Furthermore the  $b$  quark mass allows for useful approximations to be made in asymmetry calculations.

The large mass of  $B$  mesons allow them to decay weakly into many more channels than the Kaons: we owe the long lifetime of the  $K_L$  to the smallness of the phase space for 3 body decays. The  $B$  meson leptonic mode has a branching ratio of about 20% and a distinctive signature of a lepton with energy up to half that of the parent  $\Upsilon$  particle. Elementary leptonic decays of the b quark are  $b \rightarrow c\ell^-\bar{\nu}$ , with  $\ell^-$  denoting a lepton. These lead to semi-leptonic decays of the  $B$  meson,

and CP violation would be seen in the charge asymmetry  $a_f$  where

$$a_f = \frac{\Gamma(\bar{B}^0(t) \rightarrow \ell^+ \bar{\nu} X) - \Gamma(B^0(t) \rightarrow \ell^- \nu X)}{\Gamma(\bar{B}^0(t) \rightarrow \ell^+ \bar{\nu} X) + \Gamma(B^0(t) \rightarrow \ell^- \nu X)}.$$

In practice the small amount of CP violation possible in neutral mixing is coupled with large hadronic uncertainties, and so far has yielded no evidence for CP violation in  $B$  mesons. Indirect CP violation in the  $K$  system is responsible for  $\text{Re}(\epsilon) = 0$ , which give CP-violating asymmetries in leptonic decay rates. Such effects are expected to be tiny in the  $B_d$  system, where both the factor  $\left| \frac{p}{q} \right| - 1$  and the difference in lifetimes are of the order  $10^{-2}$ . While the lifetime difference in the  $B_s$  system is much greater the  $\left| \frac{p}{q} \right| - 1$  quantity is even smaller. [15]

Indirect CP violation can be found by neutral B measurements of decay times in a generalized equation

$$a_f = \frac{\Gamma(B^0 \rightarrow f) - \Gamma(\bar{B}^0 \rightarrow f)}{\Gamma(B^0 \rightarrow f) + \Gamma(\bar{B}^0 \rightarrow f)} \approx -\sin(2\phi) \sin(\Delta m \Delta t)$$

where  $f$  represents a final state, the  $\sin(2\phi)$  amplitude factor is the parameter of interest,  $\Delta m$  is the mass oscillation frequency measured [16] and  $\Delta t$  the measured difference in decay times of the two B mesons. Evidence for direct CP violation can be obtained from the decays of charged B mesons, as the CP invariance requires equality of the partial rates for  $B^\pm \rightarrow f$  and  $B^\mp \rightarrow \bar{f}$ . The asymmetry caused by direct CP violation in charged B mesons is

$$a_f = \frac{1 - |\bar{A}_{\bar{f}}/A_f|^2}{1 + |\bar{A}_{\bar{f}}/A_f|^2}$$

Estimates of direct CP violation in neutral B mesons involve large theoretical uncertainties arising from the contribution of strong phases and various diagrams. This input of strong phase uncertainties is also found in a number of decay measurements connected with mixing. As of yet, there exists no unambiguous evidence that CP violation observed in neutral B meson decays cannot be accounted for by interference of the two indirect types of CP violation. Nevertheless we have limits at the  $2.5\sigma$  level on measurements.

Sensitivity to CP violation in the B system is usually discussed in terms of the 3 interior angles  $\alpha$ ,  $\beta$  and  $\gamma$  of the unitarity triangle described previously. It will be useful to measure the three triangle angles in a number of experimentally independent tests. A number of methods for finding CKM elements are:

- $|V_{ud}|$  with  $\beta$  decays.
- $|V_{us}|$  with charged kaon decays.
- $|V_{ub}|$  from the study of  $b \rightarrow u\ell\bar{\nu}$  branching fraction.
- $|V_{cs,cd}|$  with the decay of mesons containing a charm quark.
- $|V_{cb}|$  through the  $b \rightarrow c\ell\bar{\nu}$  branching fraction.
- $|V_{td}|$  from measured  $B^0\bar{B}^0$  oscillations.
- $|V_{ts}|$  from measured  $B_s^0\bar{B}_s^0$  oscillations.
- $|V_{tb}|$  from the observation of top quark decays.
- The  $\delta$  CKM phase angle follows from measurement of CP violation in B decays.

We can see that B mesons provide the opportunity of measuring many of the CKM mixing matrix elements.

## 2.11 Measuring the Unitarity Angles

The unitarity triangle can be constrained by methods involving indirect CP violation;  $b \rightarrow c\ell\bar{\nu}$  and  $b \rightarrow u\ell\bar{\nu}$  decays,  $B^0\bar{B}^0$  mixing and indirect CP violation in  $K^0$  mesons. The  $\beta$  angle is the most simple to measure, found when we observe indirect CP violation due to interference between mixing and non-mixing decays. Our CP asymmetry equation

$$a_f = \frac{\Gamma(B^0 \rightarrow f) - \Gamma(\bar{B}^0 \rightarrow f)}{\Gamma(B^0 \rightarrow f) + \Gamma(\bar{B}^0 \rightarrow f)} \approx -\sin(2\phi) \sin(\Delta m \Delta t)$$

has approximations that can be assumed or made negligible for certain decay channels. One important channel,  $B^0 \rightarrow J/\psi K_s^0$ , has negligible direct CP violation as a result of a pure tree decay, and the unitarity triangle angle involved is  $\beta$ . In this case an asymmetry indicates a direct relationship. One finds the time difference  $\Delta t$  between decays from the separation between B decay vertices. Selection of events where one of the B pair passes all identification criteria for a  $B \rightarrow J/\psi K_s^0$  decay, and the other B has flavour content determined will yield an asymmetry evaluation. Other decay channels that are asymmetric to  $\beta$  are used to produce a weighted average for the  $\sin 2\beta$ . Effects of misidentification can be reduced by comparing identification of the second B decay when the first B meson is determined as either a CP or a non-CP eigenstate decay. BaBar has already produced a measurement of  $\sin 2\beta$  that contributes to a world average

$$\sin 2\beta = 0.701 \pm 0.053 \text{ [17].}$$

The  $\alpha$  angle is a little more difficult to determine due to the requirement  $b \rightarrow u\bar{u}d$ . This condition allows a significant number of penguin processes to complicate predictions, and thus so-called penguin pollution causes large theoretical uncertainties. The CP asymmetry when the final state is a CP eigenstate is  $a_f = -\sin 2\alpha \sin(\Delta m \Delta t)$  in the absence of penguin processes. The non-CP final eigenstates need more careful study. One typically uses two or three pion final states to attempt a determination of  $\sin 2\alpha$ . One aid is the isospin conservation law, namely that only tree (i.e. non-penguin) processes have an  $\Delta I = \frac{1}{2}$  rule. Unfortunately such analysis requires a very large volume of data, and measurements of the  $B \rightarrow \pi\pi$  decay branching fractions do not yet have sufficient precision.

$\gamma$  is an even more difficult measurement. The  $K^0$  results require  $\gamma \neq 0$  but there is a large allowed range. The most promising proposed direct methods for constraining the  $\gamma$  range include studying the triangle relations among various decay amplitudes,  $B_s\bar{B}_s$  mixing, and the  $B^\pm \rightarrow D^0 K^\pm$  and  $B_{u,d} \rightarrow \pi K$  processes.

The key to triangle relational studies is to find the amplitudes of two decays to the same final state, where one has a weak phase and a strong phase relative to the other decay. We can use geometric models to indicate  $\gamma$  angle size if we examine the magnitudes of combinatorial amplitudes with no  $\gamma$  phase. An example diagram is shown below for a decay amplitude  $A_3$  expressed as the sum of two contributions  $A_1$  and  $A_2$  in the relation  $A_3 = A_1 + A_2 = A_1 + |A_2|e^{i\gamma}e^{i\delta}$ .

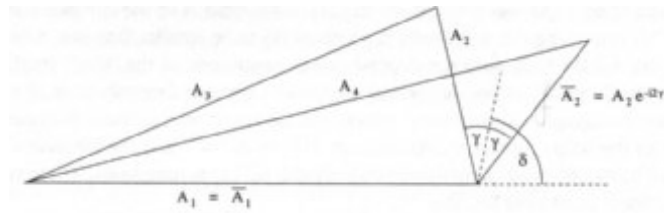


Figure 4: A combinatorial triangle example for measuring  $\gamma$

A number of  $B_s$  decays can probe  $\gamma$ , yet the  $B_s$  particle is too heavy to be produced in the  $\Upsilon(4S)$  decays that are created at BaBar. Furthermore the rapid oscillation would require excellent time resolution equipment unavailable to the collaboration for a few years yet. The  $B^\pm \rightarrow D^0 K^\pm$  and  $B_{u,d} \rightarrow \pi K$  channels are more experimentally feasible. There is a CP violating phase factor of

$e^{2i\gamma}$  between the decays  $B^+ \rightarrow D^0 K^+$  and  $B^+ \rightarrow \bar{D}^0 K^+$ , the value of which we can determine through comparison of the decay amplitudes from  $B^\pm \rightarrow D^0 K^\pm$ ,  $B^\pm \rightarrow \bar{D}^0 K^\pm$  and  $B^\pm \rightarrow D_\pm^0 K^\pm$  where  $D_\pm^0$  is a CP eigenstate with eigenvalue  $\pm 1$  found via the  $D_\pm^0$  decays. The amplitude relationships allow for an exact representation with two triangles in the complex plane, the  $e^{2i\gamma}$  value being proportional and hence determinable, shown figuratively in figure 4. Unfortunately a major setback is that these tree-level processes are highly infrequent, and need years of B-factory accumulated data for acceptable accuracy. On the other hand,  $B_{u,d} \rightarrow \pi K$  and  $B_{u,d} \rightarrow \pi\pi$  are common, but there is a large degree of theoretical uncertainty due to unwanted contributions from electroweak or gluonic penguins.

## 2.12 The BaBar Mission

The  $\Upsilon(4S)$  provides an ideal laboratory for study of B mesons due to an excellent signal-to-background ratio of about 3.5 : 1 [2], powerful kinematic constraints, low multiplicity and excellent efficiency for full reconstruction. A storage ring with beams of unequal energy Lorentz boosts the  $\Upsilon(4S)$  resonance in the direction of the higher energy beam, resulting in appreciable momenta and measurable decay paths of the B mesons. Even so, many millions of B mesons are needed for significant measurements.

The BaBar collaboration use a purpose-built B-Meson production factory and asymmetric storage ring PEP-II, providing vast quantities of data. Such data quantities allow precision measurements of small branching fractions associated with some interesting B decays. A particular area of interest involves the charmless hadronic B decays, the main motivation being a  $\sin 2\alpha$  measurement through study of  $b \rightarrow u$  with mixing, interference and study of the charged conjugate. Charmless processes may also decay via a poorly-understood but highly interesting penguin process.

The charmless hadronic B meson b quark can emit a W boson and decay into a u quark, as seen in the figure 5 below. However this W tree amplitude is suppressed by a factor of  $10^{-5}$  by the CKM matrix elements involved. Thus the possibility exists of accurately observing the b quark decaying to d or s quarks in a penguin loop of similar amplitude as seen in figure 6.

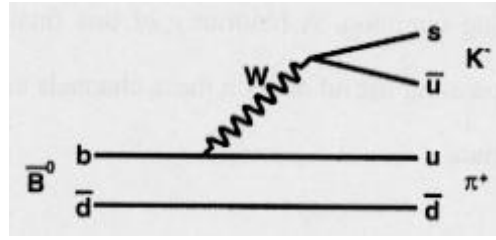


Figure 5:  $B$  meson decay via  $W$  boson emission

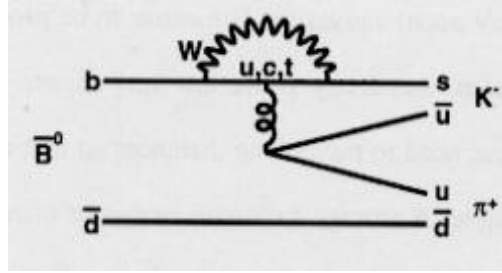


Figure 6:  $B$  meson decay via penguin contribution

The similarity of tree and penguin amplitudes in a number of charmless decays gives rise to interference effects and the possibility of large-scale CP violation. In addition to shedding light on the penguin process, charmless hadronic decays allow an improvement in CKM parameter measurements and testing of associated predictive models.

BaBar has a principal goal of obtaining accurate values of the three unitarity angles  $\alpha$ ,  $\beta$  and  $\gamma$ . One is highly interested in seeing if the angles add up to the  $180^\circ$  needed to make a closed triangle; if they do then the Standard Model fully contains the CP violation mechanism in  $B$  decays. A further consequence is that we can calculate the  $(\bar{\rho}, \bar{\eta})$  point on the triangle and hence the values of  $\rho$  and  $\eta$  that determine the degree of CP violation. Measurements in diverse processes within different systems could show this not to be the case, and one hopes more for a discovery that  $\alpha$ ,  $\beta$  and  $\gamma$  do *not* make a complete triangle. In such a scenario the CKM matrix and the Standard Model as we know it do not contain enough information to describe CP violation and this opens the door to a number of extensions to the Standard Model. The field equations currently used in Lagrangian CP calculations would need to take into account additional fields with asymmetric complex conjugates. In the case of an open triangle, BaBar's measurement of decay amplitudes of particular channels could prove illuminating in directing us to these additional contributions.

# Chapter 3

## The BaBar Detector

### 3.1 A B Meson Factory

The BaBar collaboration has two main objectives in the lifetime of the experiment. One of these is to measure the degree of CP violation in different  $B$  decay channels, and the other lies in understanding where exactly this violation occurs. Finding an open or closed unitarity triangle may give some indication of the energy scale at which further CP violation effects operate in order to account for our observed matter-antimatter asymmetry.

Understanding of differences between matter and antimatter must require measurements of CP violating effects. Theory predicts that processes exhibiting these effects should be more numerous in the decays of B mesons than K mesons, and that the effect is large in some specific rare channels. Some important CP asymmetries can be observed only in particular rare decay modes of  $B$  mesons, but for these modes extraction of CKM parameters for CP violation have technical or theoretical difficulties. Many tens of millions of  $B$  decays must be recorded and measured to study the phenomenon.

An asymmetric  $e^+e^-$  collider PEP-II has been built; the asymmetry overcomes the short  $B$  lifetime problem yet PEP-II still profits from the coherent properties of the  $B$  mesons produced via the  $\Upsilon(4S)$ . PEP-II uses a high energy 9 GeV  $e^-$  beam colliding with a 3.1 GeV  $e^+$  beam such that the center of mass energy of the system is at the 10.58 GeV  $\Upsilon(4S)$  resonance. Beam energies are slightly above the energy level for  $\Upsilon(4S)$  production to allow extra accuracy in measuring the low momenta of a produced  $B$  meson. A big advantage for choosing an  $e^+e^-$  environment over hadronic oness is the higher signal-to-background ratio; the process of  $e^+e^- \rightarrow \Upsilon(4S) \rightarrow B^0\bar{B}^0$  or  $B^+B^-$  pairs has little interference from background. Hadronic processes in contrast tend to have low B purity. Nevertheless it can be useful to work with energies below the  $\Upsilon(4S)$  limit to produce data containing no B mesons. Such data is labelled "offpeak" and contributes to our understanding of the

impact of background events on B meson measurements. The large numbers of B mesons needed for extensive analysis set the requirement that the PEP-II collider has luminosity of order  $3 \times 10^{33} \text{cm}^{-2} \text{s}^{-1}$ .

An electron gun creates bunches of electrons which are then accelerated to 9 GeV and injected into the high energy ring (HER). Contemporaneously other electrons are collided with beryllium to form positrons, and these antimatter particles are accelerated to 3.1 GeV before injection into the low energy ring (LER). The corresponding beams of electrons and positrons are collided at the detector point with the aid of magnetic focussing systems. The BaBar detector is situated in the PEP-II electron-positron collider facility. These processes are illustrated below in figure 7:

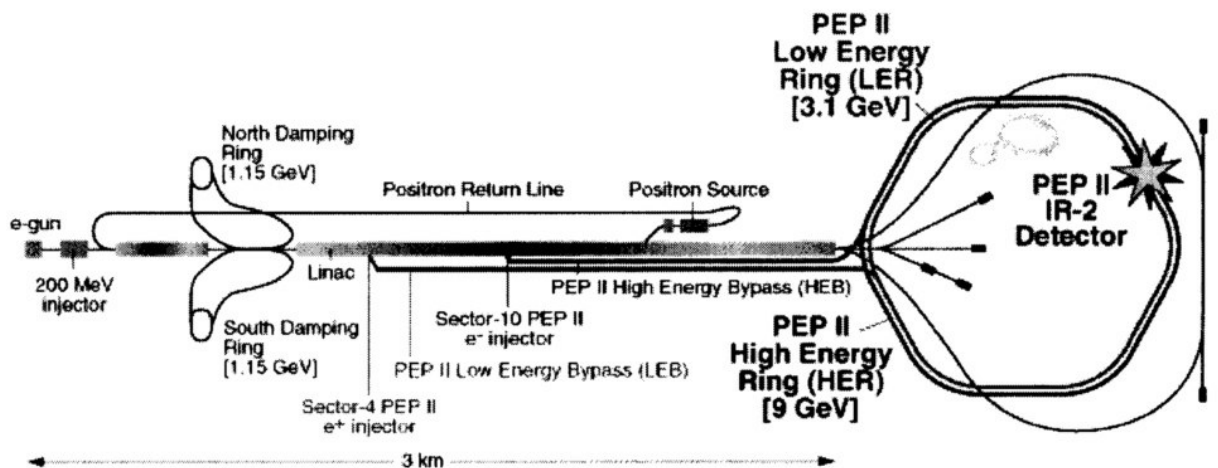


Figure 7: Layout of the PEP-II electron-positron collider facility, also known as the "B factory"

The high beam strengths pose problems of background for the detector. Some of this is synchrotron radiation from nearby magnets and reduced by the use of copper masks. Another source of unwanted effects are the particles that interact with beam gases, which are minimised by maintaining a strong vacuum. The other main contribution to background are those beam particles which become scattered by collisions with other beam particles into the nearby equipment, and subsequently give rise to electromagnetic showers picked up by the detector. This last contribution is known as luminosity background. Luminosity is measured by finding the ratio of the number of hadronic events enriched with  $B\bar{B}$  pairs to lepton pairs. Calibration of the absolute centre-of-mass energy uses fully reconstructed B decays.  $B\bar{B}$  pairs have a beam axis separation of  $\sim 200 \mu\text{m}$  between their respective decay vertices due to a  $\beta\gamma \sim 0.56$  boost. High luminosities are achieved by a combination of high beam currents and strong beam focussing magnets. The strengths of the

currents require the beams to be divided into large numbers of packets so as to reduce the effects of beam-beam interaction.

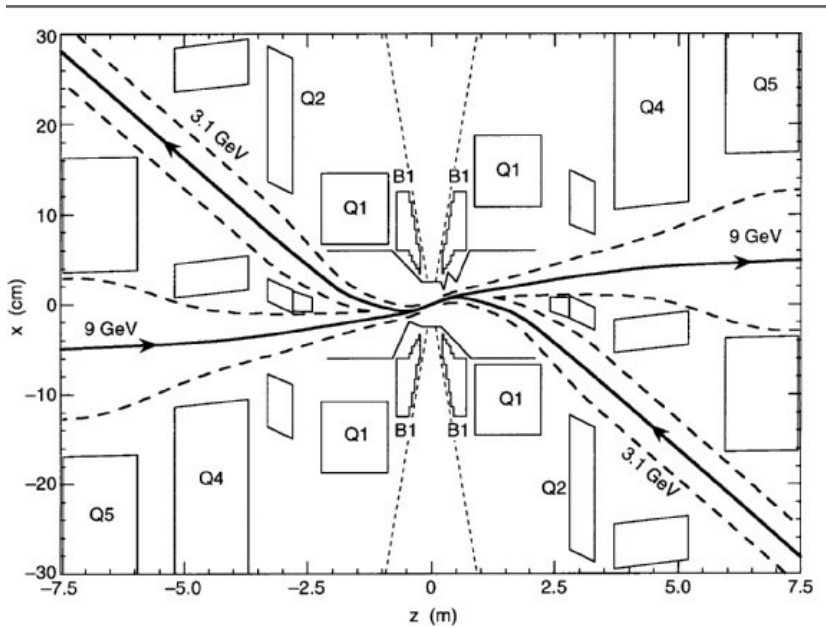


Figure 8: Plan view of magnet layout in interaction region with stretched vertical scale.

The experiment started running in May 1999, and first results on CP violation from B decays were published during the year 2000. BaBar will continue to accumulate data for many years, allowing measurements in many different B decay channels, to provide a comprehensive test of the theory of CP violation. General studies of the physics of B mesons, as well as that of charm mesons, tau leptons and quantum chromodynamics (QCD), will also be possible with unprecedented accuracy.

## 3.2 An Overview of the BaBar Detector

If the collaboration is to achieve the physics goals stated at the start of this chapter then the BaBar detector needs to meet several very exacting design requirements. It should have excellent particle tracking resolution and efficiency. At a most general level there should be maximum possible acceptance in the centre-of-mass system. Foremost considerations are the full reconstruction of  $B^0$  final CP eigenstates, a knowledge of the time difference between production and decay of a  $B^0$  meson and flavour identification of the other  $B^0$  meson. Otherwise, the detector concept is that of a relatively standard  $e^+e^-$  collision detector, with slight modifications to

accommodate the boost of the centre of mass system and an emphasis on particle identification indicating a bias towards  $B$  physics. A schematic of the detector is shown here with major components labelled:

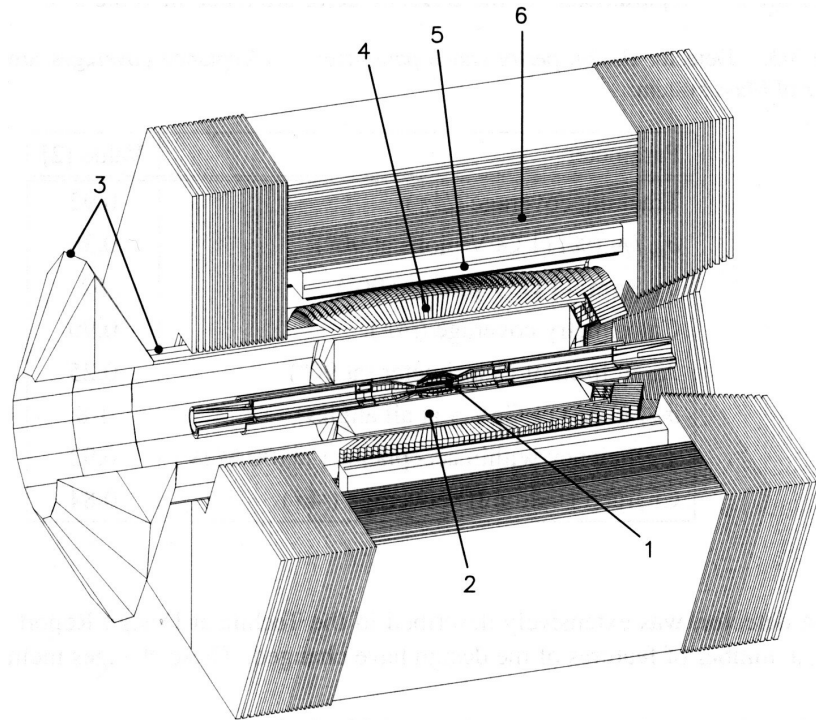


*Figure 9: Schematic layout of the BaBar detector.*

Labelled parts are summarized as follows:

1. The Silicon Vertex Tracker (SVT) which provides precise information on the position of charged tracks; it is the only device that can track very low-momentum charged particles.
2. A Drift Chamber (DCH) which is filled with a helium-based gas to minimize multiple scattering. This component provides the main momentum measurement for most charged particles, and energy loss measurements are used to aid particle identification.
3. A Detector of Internally Reflected Cerenkov light (DIRC). This is designed for charged hadron identification.
4. A Caesium Iodide Electromagnetic Calorimeter (EMC). It has a forward endcap, but none in the backward direction, for reasons of economy, as the boost directs all but a tiny fraction of particles away from the backward direction. The calorimeter provides good electron identification down to about 0.5 GeV, and information on neutral hadrons and photons.
5. A superconducting coil surrounds the above components, providing a 1.5 T axial

magnetic field essential to momentum measurement.

6. An Instrumented Flux Return (IFR) for muon identification down to about 0.6 GeV and neutral hadron identification. These two characteristics are of particular interest in the numerous CP violating time-dependent asymmetries involving  $B^0$  mesons and  $K_L^0$  particles respectively.

Major components are mounted in a zone that is not easily accessible and any intervention requires a shutdown period. Therefore given the high statistics needed for CP violation studies, particular attention was paid to overall detector reliability. A common emphasis was placed on maximizing solid angle coverage around the  $\Upsilon(4S)$  centre of mass, though the surrounding PEP-II equipment limits this. Dimensions of the BaBar detector are about 10m along the longitudinal beam axis and 3.5m in the transverse section.

### 3.3 The Silicon Vertex Tracker

The main function of the BaBar vertex detector is to reconstruct the decay vertices of the two primary  $B$  mesons so that the time between these two decays can be determined. This is vital to the measurement of time-dependent CP asymmetries in  $B^0$  decays. Greatest angular information on a track is provided by the silicon vertex detector since impact parameter resolution improves when the detection point is closer to the production vertex. Precision measurements from the more radially outmost major detector components is limited by multiple scattering and added extrapolation uncertainties. This subdetector provides the only tracking information for charged particles with transverse momenta lower than 100 MeV/c (the drift chamber reaches full efficiency only for tracks with transverse momentum larger than about 180 MeV/c, sub 100 MeV/c charged particles remaining out of measurement reach.) Ionization losses of tracks with momenta below 700 MeV/c can be used for particle identification in the SVT. Tracks are usually reconstructed initially in the drift chamber and then extrapolated to the SVT, and matched up with SVT hits to give the positional information. Crucial checking of the alignment is done using  $e^+e^- \rightarrow \mu^+\mu^-$  and cosmic ray tracks.

The diagrams below indicate the longitudinal and transverse design respectively of the SVT apparatus

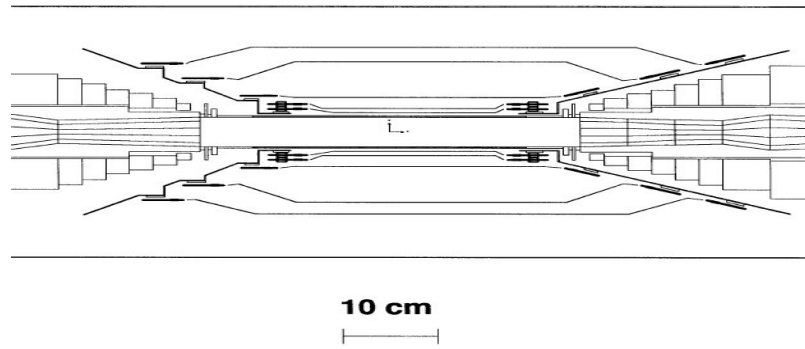


Figure 10: Cross-sectional view of the SVT along the beam axis

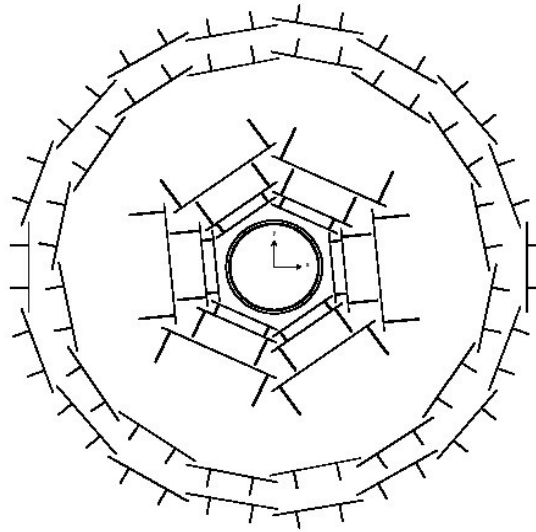


Figure 11: Cross-sectional view of the SVT across the beam axis

The basic requirement of CP violation physics on the silicon vertex tracker is to measure the separation between the two  $B$  vertices along the boost axis at PEP-II. This corresponds to a single vertex precision of better than  $80\mu\text{m}$  and secondary vertices accuracy better than  $100\mu\text{m}$ , both readily achievable with silicon micro-strip detectors. However, obtaining a better precision aids pattern recognition, vertex reconstruction and background rejection. The silicon vertex tracker was designed to reach an optimum practicable resolution, although multiple scattering sets the limit for the useful point resolution. Resolutions of  $10 - 15\mu\text{m}$  for the inner layers and  $30 - 40\mu\text{m}$  for the outer ones ensure that the vertex position resolution is dominated by the uncertainty due to multiple scattering. Under such circumstances the BaBar SVT achieves a resolution of  $25 - 65\mu\text{m}$ . Efficiency of the combined SVT hardware and software, which compares the number of hits to the number of tracks passing the active area, is found to be around 97%.

The SVT structure consists of five concentric cylindrical double-sided layers of 5cm flat silicon

wafer squares. The three innermost layers are 3 to 5cm from the beam axis; each has 6 strips designed to measure distance along the axis of boost and the azimuthal angle about this axis. The fourth layer has 16 strips and the outermost layer 18 detector strips all in an arch pattern for maximizing solid angle coverage and allowing module overlaps, as the primary purpose of these outer layers is for pattern recognition. A total of 340 detectors comprising 150,000 readout channels cover an area of about  $1\text{m}^2$  in the SVT.

A collider detector is generally required to cover as much solid angle as possible. Particular care must be taken to maximally cover the forward region as a result of PEP-II's asymmetric nature, and so machine components such as cooling systems are located in the backward region. Minimizing any necessary dead spaces such as mechanical supports, electronics and cabling allows the active parts of the silicon vertex tracker to cover the polar angle between  $20.1^\circ$  and  $150.2^\circ$ .

A near-perfect overall track reconstruction efficiency is needed to handle the high background level at PEP-II. Moreover, low-momentum tracks, like slow pions in  $D^*$  decays, are mostly contained in the silicon vertex tracker volume; in this case only the silicon vertex tracker information can be used for track reconstruction. In addition, the silicon vertex tracker must be efficient for decay products of particles like  $K_S^0$ , which decay within the SVT volume.

As the vertex position resolution is dominated by the precision of the measurement closest to the interaction point in the inner layers of the five concentric cylindrical layers, both high efficiency and good point resolution are needed for these inner layers, requiring redundancy for this measurement. Also an outer point redundant measurement is needed to allow a better alignment with the drift chamber measurements. The third detector, placed in the middle region, helps the track reconstruction in particular when the tracks' helices are completely contained in the silicon vertex tracker volume.

Electronic signals initiated by passing charged tracks are transferred to the Front End Electronics (FEE), hybrid circuit boards distributing power and signals to mounted processing chips hardened against radiation. At this point the Time Over Threshold (TOT) length is compared with a TOT limit, and charges induced on strips whose TOT length exceeds the TOT limit are stored on a logarithmic scale in data crates for future processing, along with the corresponding location and time stamp. The TOT length has a relationship with charge through the ionization

losses, and these give a cleaner indication of charge than other methods such as counting pulse magnitudes. Information streams are sent from the L1 hardware trigger processors to a Fast Control Trigger System (FCTS). This in turn combines each stream and issues an accept signal for the commencement of the data crate buffer readout to the L3 event builder. Given a L3 accept command an event is then stored for future reconstruction offline.

## 3.4 The Drift Chamber

The drift chamber is the primary tracking device and charged particle detector of BaBar. In tandem with the silicon vertex tracker it provides spatial, momenta and angle measurements with excellent precision. Up to 40 measurements of space coordinates per track ensure a high reconstruction efficiency for tracks with transverse momentum greater than 100 MeV/c. The BaBar drift chamber system is exclusively responsible for providing information for  $B$  meson reconstructions, such as processes involving  $K_S^0$  particles, outside the SVT.

Performance goals of the drift chamber are to provide spatial resolution better than 140  $\mu\text{m}$  averaged over the radial - azimuthal angle plane, and to supply particle identification for low momentum tracks by measurement of ionization loss ( $dE/dx$ ). A  $dE/dx$  resolution of 7% over a total of 40 measurements allows discrimination between pions and kaons of momenta up to 700 MeV/c. The angular acceptance in the forward region extends down to the beam-line components, adhering to the general detector principle of maximal acceptance. In addition, the drift chamber provides a principal trigger for the experiment with event time feeds of less than 0.5  $\mu\text{s}$  uncertainty.

Momentum resolution for low momentum tracks is limited by multiple scattering in both the silicon vertex tracker and the inner cylinder of the drift chamber. Decay vertices occurring outside the SVT rely solely on the drift chamber for transverse and longitudinal positioning with a resolution approaching 1 mm. The following figure shows a longitudinal section of the drift chamber.

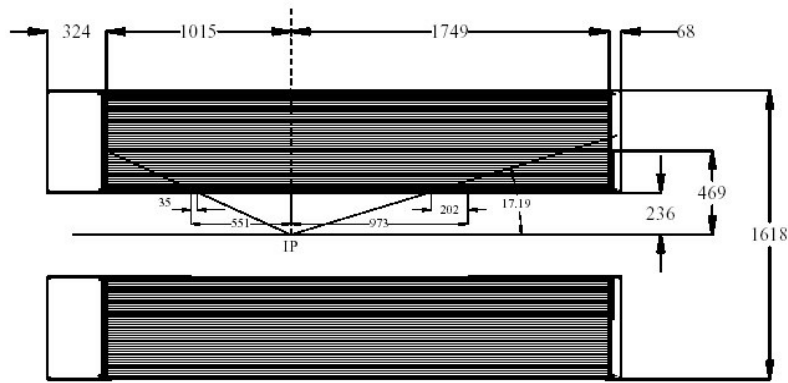


Figure 12: Side view of the drift chamber. Note dimensions are in mm

As illustrated in the picture, the cylinder is about 3 m long and situated asymmetrically about the interaction point such that centre of mass solid angle is maximized. The material in the drift chamber affects performance of the DIRC and electromagnetic calorimeter. The mechanical structure of the drift chamber essentially comprises light wires stretched between the endplates: 20  $\mu\text{m}$  diameter sense wires of gold-plated tungsten-rhenium and 80 or 120  $\mu\text{m}$  diameter gold-plated aluminium field wires. A 80:20 helium:isobutane low mass gas mixture with trace water vapour fills the drift chamber. Helium minimizes multiple scattering effects and isobutane provides the gas mixture with the critical density to evenly spread throughout the chamber, while the addition of water vapour prolongs the effective lifetime of the equipment.

Wires are arranged in 40 circular layers of hexagonal cells, each cell being about 1 cm in size and containing one sense wire surrounded by six field wires. A sense wire has a positive high voltage applied to create a near radial field over much of the cell. Any charged particles will ionize the gas mixture and initiate a drift of electrons towards the sense wire that culminates in an electron avalanche in the immediate vicinity of the wire. The distance from the sense wire at which gas ionization occurs is related to the time taken for the electrons to reach the wire. Precision measurements of the drift time undertaken with  $e^+e^-$  and  $\mu^+\mu^-$  lead to the contours illustrated in figure 13. Combining the measurements for sense wire detections and ionization loss for particles above 140 MeV/c transverse momentum with information from other detector components provides a very reliable measurement of track parameters. Four wires comprise a superlayer, each layer being offset half a cell from the next. Transverse directional ambiguities are resolved by the offsetting of cells. Six of the ten superlayers, the so-called stereo layers, have wires that are

arranged at small angles between  $\pm 40$  mrad and  $\pm 76$  mrad to the beam axis; longitudinal positioning information is enabled from the configuration of the sequential pattern of axial angle and opposite magnitude same angle pairs. We see the superlayer arrangement with the axial (A) and stereo (U,V) cells as indicated in figure 14 below.

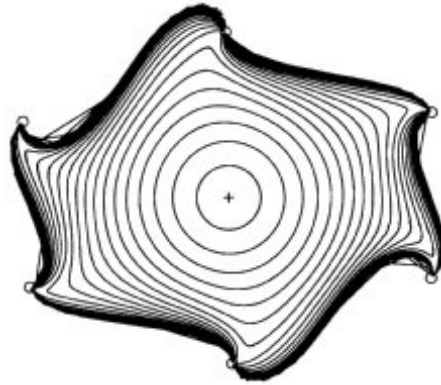


Figure 13: 100 ns contours of equal ion drift times for an axial superlayer cell.

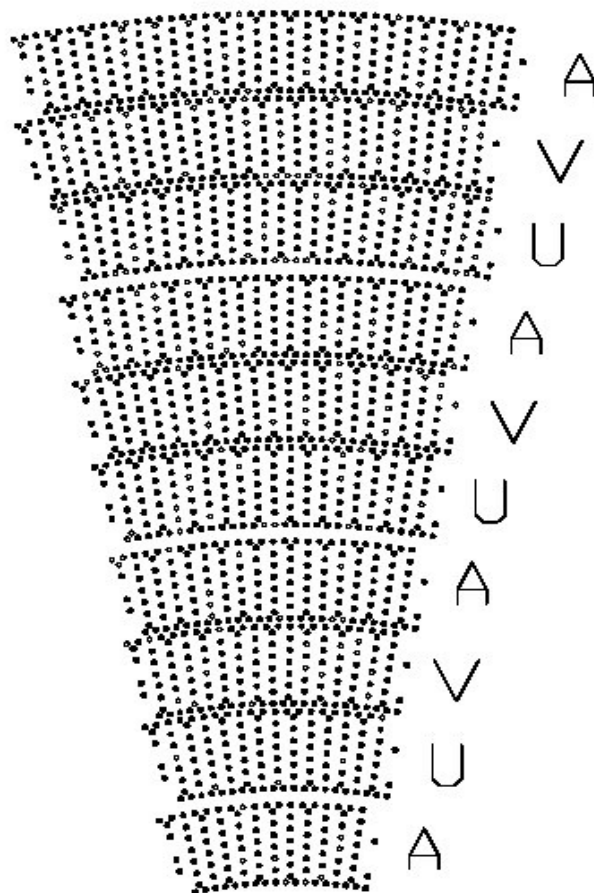


Figure 14: Cellular layout of wires with sequential pattern of axial (A) and stereo (U,V) angled

*superlayers.*

Read-out electronics are mounted on the rear endplate to minimize the material in the forward region. Time to 1 ns resolution and total deposited charge over  $1.8 \mu\text{s}$  are recorded for each cell signal and are corrected by various factors: gain constants, cell geometry and any voltage or time offsets, as found from  $e^+e^-$  and  $\mu^+\mu^-$  calibrations. Digitized versions of these measurements are then stored in data crates and fed through the L1 and L3 trigger systems; the drift chamber trigger, as part of the L1 trigger, receives a 32 MHz stream of true or false hits for every channel. Drift chamber hits in each of a superlayer cell across a small azimuthal angle range are combined with other superlayer hits postulated to be from the same track into helical tracks and fitted. SVT hits are then matched with these data from the drift chamber, and charged tracks are reconstructed from SVT and drift chamber data combined. Offline reconstruction involves using a series of fitting algorithms for finding additional track hits in the drift chamber, and extrapolating to allow the combining of additional information from other detector components. A final Kalman filtering method fits the tracks, considering any effects the detector material and magnetic field may have had on detection and selecting hit information. Any SVT tracks with no correlated drift chamber information are fitted using a computation method designed for track detection in a single subsystem. Track efficiency largely depends on the drift chamber and currently almost approaches the 98% charged track efficiency design specifications, and the ionization loss resolution of 7.5% nearly matches the 7% hoped for in the technical reports. Tracks with transverse momentum above 1 GeV/c have a  $\Delta P_t / P_t$  resolution of  $0.3\% \times P_t$ , where  $P_t$  is the transverse momentum in GeV/c, as found from differences in fitting the upper and lower sections of muonic cosmic rays.

### **3.5 The DIRC**

The BaBar DIRC (Detection of Internally Reflected Cherenkov light) subdetector is a ring imaging optical detector devoted to particle identification. This device relies on the principle of detecting the Cherenkov photons trapped in the radiator due to total internal reflection, the magnitude of angles to the beam axis remaining constant through reflection on a flat surface parallel to the axis. A foremost design criterion of the DIRC was that it would provide the excellent

kaon identification essential for particle ID tagging purposes; kaon momenta lie in the sub 2.0 GeV/c range yet the drift chamber and SVT cannot provide particle ID above 700 MeV/c momenta. Studying rare charmless  $B$  meson decay processes such as  $B^0 \rightarrow K^\pm \pi^\mp$  and  $B^0 \rightarrow \pi^\pm \pi^\mp$  motivates the requirement that the DIRC must be able to separate pions from kaons by 4 standard deviations up to about 4.0 GeV/c momenta through large angles in the laboratory frame in order to distinguish decay modes. Furthermore the DIRC must also participate in identification of muons below 750 MeV/c momenta since the IFR becomes inefficient at this point. The 1.5 T magnetic field determines that the DIRC radiator can only be reached by particles produced at the interaction point with  $P_T$  in excess of 250 MeV/c.

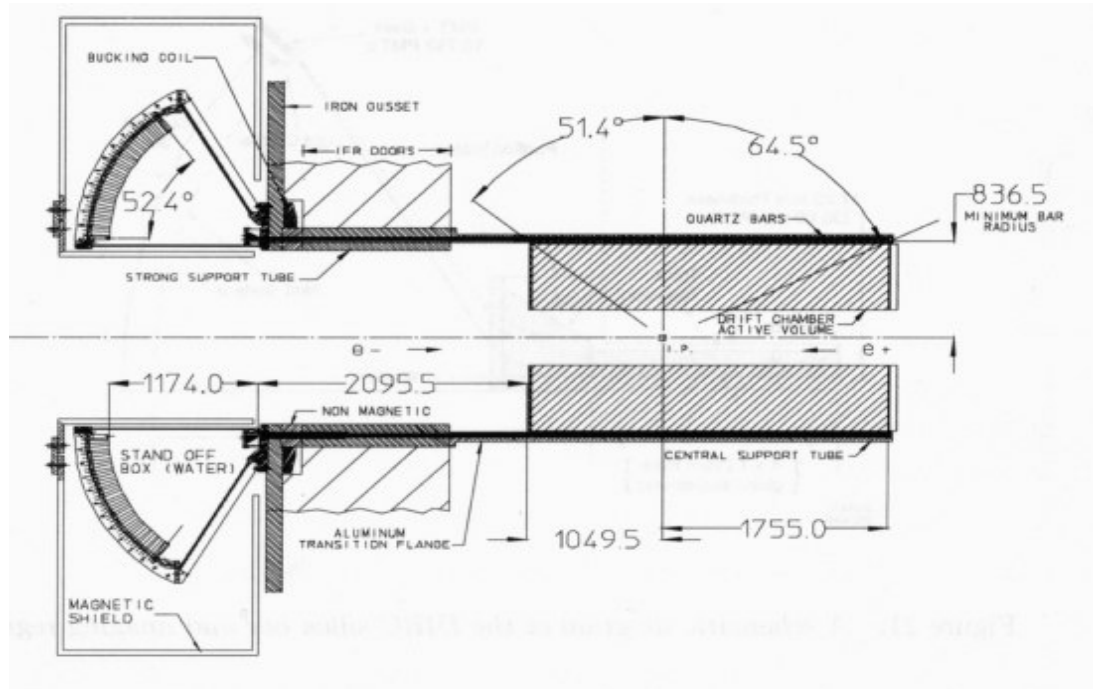


Figure 15: Schematic diagram of the DIRC layout.

A longitudinal view of the DIRC is shown in the diagram above. The particle identification detector is designed with minimal thickness of 80 mm radial dimension in order to distort the electromagnetic calorimeter measurements as little as possible. Charged tracks passing through the radiator bars create some Cherenkov photons which travel down the bars by the mechanism of total internal reflection. This radiator material is a 12-sided polygon barrel of rectangular bar boxes of 4.9 m in length, each box containing 12 synthetic fused quartz silica bars of dimensions 17 mm  $\times$  35 mm and separated by 0.15 mm air gaps. A charged particle of velocity  $\beta$  passing through a

material of reflective index  $n$  emits Cherenkov radiation at an angle  $\theta_C = 1/n\beta$ , providing that  $\beta > 1/n$ . All surfaces of the bars except the instrumented rear end have a refractive index of  $n = 1.472$  when reflecting the photons, the front end employing a mirror to aid reflection and the rear end being extended to avoid the calorimeter end-cap. Snell's law dictates that these photon angle magnitudes will be constant when successively reflecting off flat surfaces. Any photons trapped by total internal reflection will travel out of the rear end of the bars into a 6000 litre water tank and onto a back wall covered with nearly 11,000 densely packed photomultiplier tubes each of 29 mm diameter. The water has a reflective index  $n = 1.346$ , as close as possible to that of the bars, in order to minimize any water surface reflection. A silica wedge reflects any photons with an overly large angle in order to reduce the necessary size of the detection wall. Light-catcher cones further increase the effective area of the wall to about 90%. The configuration of the wedge is such that photons with identical azimuthal and polar angles impact the same photomultiplier tubes. We see the mechanism of photon detection illustrated below in figure 16.

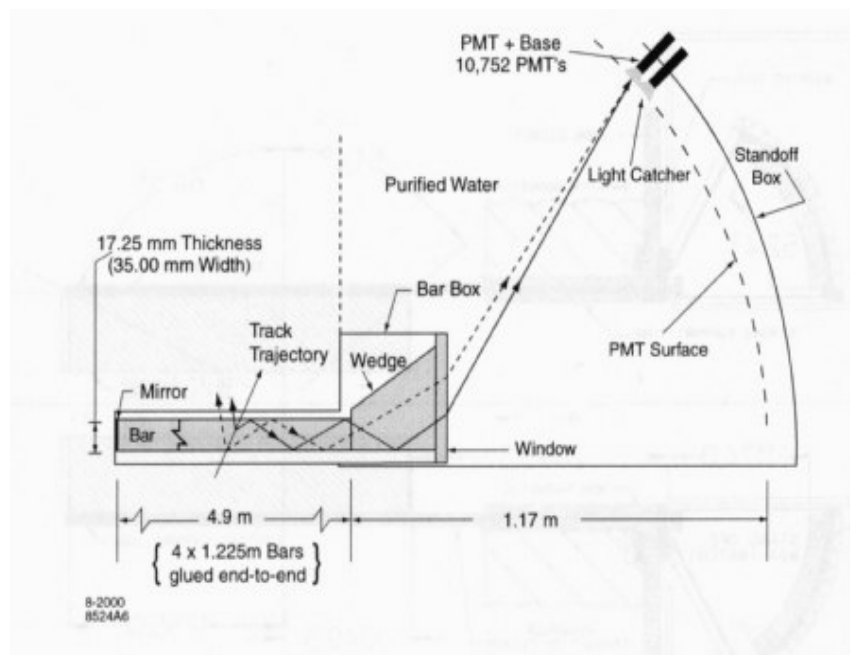


Figure 16: A DIRC silica bar and imaging section.

Any Cherenkov photon detected in the photomultiplier array has the arrival time and individual photomultiplier tube hit data passed to the Front End Electronics (FEE) with about 1.5 ns accuracy in both the FEE and tube section measurements. Data is passed to the read out modules for processing and feature extraction. One then attempts to reconstruct the particle track using event

builder trigger software: photomultiplier signals are matched with temporal and spatial data from other detector components and then fitted with differing mass hypotheses. One stores relevant information for analysis when fits of enough photons at a particular  $\theta_C$  reflection angle are judged to constitute a track path. The use of mass hypotheses in the association of photons with tracks cause a  $\theta_C$  bias for low numbers of photons, so one must cut down on high photon numbers to maintain measurement consistencies. DIRC performance is dependent on the accuracy of track extrapolation, and the best results are found with the Kalman filtering fit that takes into account the effects of scattering and energy loss. Generally the DIRC is robust and the efficiencies are easily calculated from the well known properties of the construction materials and conventional photomultipliers. Any response factors due to the equipment that cause a timing delay are calibrated using a pulsar setup, while DIRC performance is tested with  $e^+e^- \rightarrow \mu^+\mu^-$  where one disregards photomultiplier hits outside a fitted range in the timing of the detected event. Separation between pions and kaons falls off at higher momenta, dropping below the 4 standard deviations design requirement for particles with momenta in excess of about 3 GeV/c.

## 3.6 The Electromagnetic Calorimeter

Processes involving electromagnetic showers are important for calibration and luminosity checks in the BaBar detector. Additionally many decays necessary for CP violation measurements have final state  $\pi^0$  particles requiring reconstruction from photons. The Electromagnetic Calorimeter (EMC) was designed to meet the requirements of measuring photons of energies up to 9 GeV for QED processes like  $e^+e^- \rightarrow \gamma\gamma$  and down to 20 MeV, since many rare charmless decay  $\pi^0$  photons lie in the sub 200 MeV range. Particle mass resolution is dominated by EMC energy resolutions below 2 GeV and angular resolution above. BaBar physics requirements on the angular and energy resolution together with a requirement for excellent efficiency led to a hermetic calorimeter design based on thallium-doped caesium-iodine (CsI(Tl)) crystals.

The calorimeter consists of a cylindrical barrel section and a forward conic endcap. A segmented barrel array of 5760 crystals in 48 rings and on end-caps of 820 crystals in 8 rings provide total photon absorption. Radially, the barrel is located outside the DIRC system and within

the magnet cryostat, and it is supported off each end of the coil cryostat. This barrel is asymmetric about the interaction point, allowing the crystal array's fine segmentations to cover all the polar angle and 90% of the cosine of the azimuthal angle in the center-of-mass frame over a solid angle  $-0.916 \leq \cos \theta \leq 0.895$ . Useful physics coverage is less than this to avoid regions of excessive photon shower leakage from the forward and backward edges. We see the longitudinal layout of the EMC in the following figure

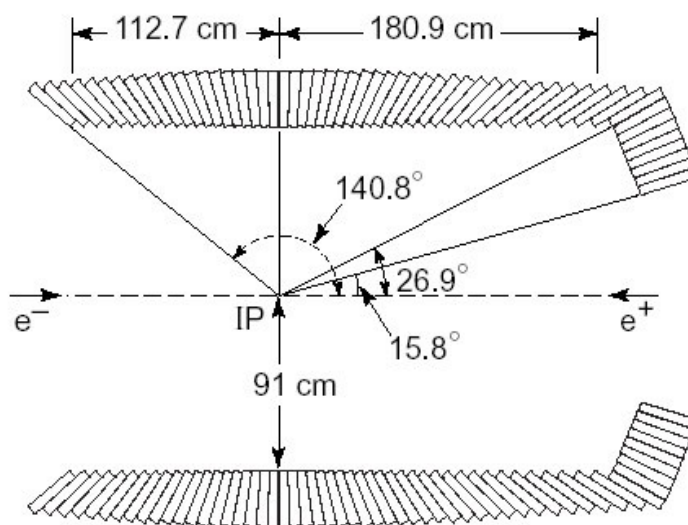


*Figure 17: Longitudinal layout of an EMC section. Distances shown are in units of mm.*

The minimum detectable energy for photons is about 10 – 20 MeV. It is largely determined by material in front of the calorimeter and beam related backgrounds down to energies as low as a few MeV, since the intrinsic crystal efficiency is close to 100%. Caesium-iodine crystals of trapezoidal shape are arranged in a layout so that their axes point slightly to one side or the other of the interaction point. A Molière radius comparable to the transverse dimensions of the crystals results in a shower that spreads over several crystals. Scintillation crystals reflect off polished sides of these crystals until detection by small silicon PIN diodes located on the back of the crystal. Photodiodes are used because the strong magnetic field in which the calorimeter lies means that photo-multiplier tubes are ineffective.

Energy resolution is affected by losses arising from front and rear leakage ( $< 0.5\%$ ), inter-calibration errors (0.25%), and light collection non-uniformity ( $< 0.5\%$ ). Electronic and beam-background noise also worsen the energy resolution. The energy resolution also degrades towards the ends of the barrel as a consequence of the staggered arrangement of crystals and the

increasing amount of inactive material in front of the calorimeter. The angular resolution is determined by the transverse crystal size and distance to the interaction point.

Crystal signals above a 1 MeV threshold are digitized and transferred in a continuous stream to Read Out Modules (ROMs), where calibration correction factors are applied. Data selected by a Level 1 accept command are processed with a feature extraction algorithm that makes a parabolic fit to the signal waveform of each crystal. The energy and time of the signal is the only information retained for reconstruction purposes. Clusters are formed by pattern algorithms combining crystal energies after an electromagnetic shower typically activates a number of adjacent crystal diodes and leaves at least one 10 MeV signal. Surrounding signals count towards a cluster measurement if the signal exceeds 1 MeV or the crystal is situated next to a neighbouring crystal that picked up a signal of 3 MeV or more. Crystals are labelled as local energy maxima  $E_{LocalMax} > E_{NeighbourMax}$  and  $0.5(N - 2.5) > E_{NeighbourMax}/E_{LocalMax}$  where  $N$  represents the number of neighbours with energy above a 2 MeV threshold and  $E_{NeighbourMax}$  the greatest energy of any of these neighbouring crystals. These local maxima are called bumps, and an iterative algorithm assigns bumps either to tracks found the SVT or drift chamber or to neutral particles if no corresponding track is found. Calibration of the EMC detector requires several steps. Light yield varies between crystals and can change following radiation damage. A 6 MeV radioactive source placed inside the detector serves as a low energy calibrator, while 3-9 GeV/c<sup>2</sup> scattered electrons from Bhabha scattering ( $e^+e^-$  elastic scattering) cater for high energy calibration. The energy of an incoming particle is estimated from cluster energies and corrected for factors such as photon leakage from crystals, absorption due to crystal gaps or material in front of the EMC, and crystal signals that are unassociated with the particle tracking.

### 3.7 The Instrumented Flux Return Detector

Efficient detection of muons is highly relevant to the BaBar collaboration's investigation of CP asymmetry in reconstructed events. Many CP decay modes contain final state muon particles, and flavour tagging of the neutral B meson decay is greatly aided with muon identification. Additionally neutral hadron particle identification allows study of numerous neutral  $B$  meson decays to final CP

eigenstates, in particular processes involving the  $K_L^0$  particle. The large iron structure needed as the 1.5T magnetic flux return is segmented and instrumented with single gap Resistive Plate Chambers (RPCs) in order to provide muon identification and neutral hadron detection in tandem with the EMC. This system is called the Instrumented Flux Return (IFR) and consists of a central hexagonal barrel structure with two plugs (end caps) which extend the solid angle coverage down to 300 mrad in the forward direction and 400 mrad in the backward direction. A wide solid angle coverage and good detection efficiency coupled with high background rejection for muons down to 1 GeV momenta are the primary requirements in the IFR particle identification design.

The iron is segmented and finely graded into 18 flat sections. These plates increase in thickness with the radial distance from the interaction region starting at 2 cm for the innermost to 10 cm for the outermost plates in the barrel, with one 5 cm and one 10 cm plate in the end caps. Detailed Monte Carlo studies led to an optimal structure of segmentation by showing that  $K_L^0$  detection and low momentum muon identification improve as the iron thickness decreases for a given amount of absorber. This effect is most important in the first absorption length, and so grading the segmentation strikes a balance in improving performance without excessively increasing the number of layers. The diagram 18 below outlines the structure of the IFR barrel

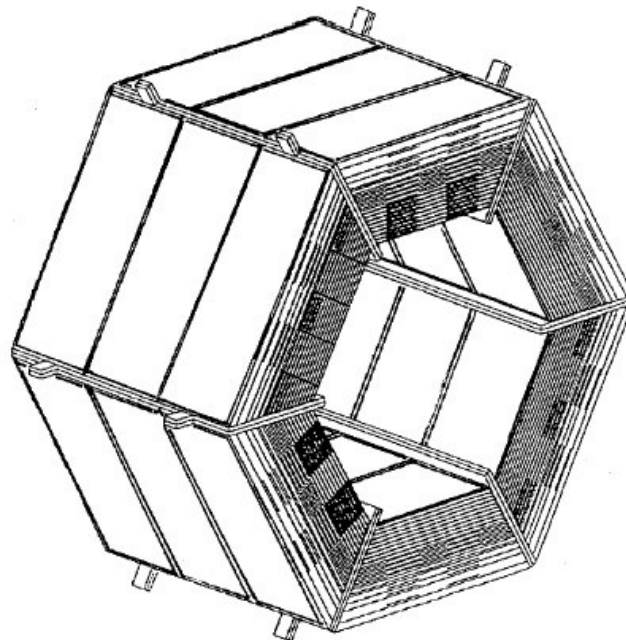


*Figure 18: Layout of the RPC modules in the barrel.*

There are 19 RPC detector layers in the barrel: a double layer cylindrical RPC between the

EMC and coil, and an inner layer of RPCs between the solenoidal coil and the iron together with 17 layers within the gaps. One last layer outside the iron structure completes an IFR total coverage area in excess of  $1000 \text{ m}^2$ . The gaps housing the RPC layers are 3.2 cm wide with the exception of the 3.5 cm gap between the innermost 2 cm barrel plates. Capacitive aluminium readout strips allow an RPC to detect streamers caused by impacting ionizing particles. RPCs are constructed from dual Bakelite sheets of 2 mm thickness which are separated by a 2 mm argon-freon gap. The sheet surfaces have an external graphite coating connected to a 8 kV voltage and ground. A 4 mm layer of insulation separates the graphite from the readout strips on one side that measure boost axis position and the readout strips on the other side that measure the azimuthal angle. The strip electrodes run lengthways and crossways along the chamber in such a way as to provide 3 dimensional information. In total there are 342 RPC modules in the barrel each with 32 boost axis longitudinal strips and 96 azimuthal angle strips. 432 modules individually containing 64 vertical and 64 horizontal strips are positioned on the end-cap doors.

Signals above a threshold limit are shaped by the Front End Electronics and sent to ROMs. The data is stored along with a the time of detection while the ROM waits for a readout acceptance or rejection signal from the hardware trigger. Similarly to the EMC offline reconstruction, nearby hits in the IFR are combined into clusters. Passing particles generate signals in several strips, and initially a one-dimensional cluster is the combination of adjacent readout hits in a single layer. Considering these clusters across multiple layers allows the definition of two dimensional clustering of typically  $1 \text{ cm}^2$  per cluster. The final step in the construction of clusters is the progression to three dimensions by combining different two dimensional clusters in each section. Providing that enough information exists then the full clusters are associated with data from other detector sub-systems to make tracks or energy bumps. IFR efficiency is assessed with cosmic rays and collision data from events that have predictable characteristics inferred from other sub-system measurements; an RPC is deemed efficient if signals are detected within 10 cm of the extrapolated track intersection with the detecting module. Experience has shown that numerous RPC modules have gradually decreased in efficiency with time, though the small impact on IFR performance justifies the BaBar collaboration's decision to construct large number of RPC layers before the start of data taking.

## 3.8 The Trigger

An essential component of the BaBar detector is the data acquisition system for all types of signals ranging from B decays to other events and backgrounds. Signals passing sub-component detection thresholds are processed and digitized by Front End Electronics (FEE), then buffered in dataflow crates while waiting to undergo Level 1 trigger acceptance tests. The BaBar trigger has two levels conventionally denoted by Level 1 which executes in hardware and Level 3 which executes in software after the event assembly. The primary performance measure of a trigger system is its efficiency for benchmark physics processes and background rejection. Total recorded event rates are required to remain below 120 Hz at BaBar, with trigger efficiency above 99% for  $B\bar{B}$  events and 95% for continuum or  $\tau^+\tau^-$  events while exhibiting less than 1% trigger downtime.

The Level 1 trigger system comprises the four following sub-systems and is designed to achieve very high efficiency and good understanding with minimum operational downtime. The charged track trigger, also known as the drift chamber trigger, requires at least two tracks in the drift chamber: one long track with  $P_t > 0.18$  GeV/c and a shorter track with  $P_t > 0.12$  GeV/c. The energy trigger, or electromagnetic calorimeter trigger, requires two clusters in the electromagnetic calorimeter, both with reconstructed energy deposits above a threshold that is efficient for muons. A neutral particle trigger, also labelled the IFR trigger, is solely employed for  $\mu^+\mu^-$  triggering and cosmic ray calibration studies. These three triggering systems continuously send positional and kinematic trigger information primitives to the Global Level 1 Trigger (GLT) which combines it. The independence of the requirements allows good cross-calibration of trigger efficiency. Under nominal background conditions, this ‘open trigger’ produces an output rate of around 1 kHz from triggers activated 12  $\mu$ s after an event, while yielding the required near perfect efficiency inside the fiducial region of the detector for  $B$ ,  $\tau$  and  $\gamma\gamma$  physics. At design luminosity the typical background rates due to the beam are in the region of 20 kHz each for a track greater than 120 MeV/c  $P_t$  in the drift chamber and any hits above 100 MeV in the EMC. Deterioration of beam luminosity means that data taking on BaBar generally lasts for two hours or less at a time.

A continuous stream of GLT events in 134 ns steps are sent from the Level 1 trigger onto the

Fast Control and Timing System (FCTS) whose purpose is to combine data packets and include a Level 1 Accept tag. This tag enables events to be restored in the data crate buffers for eventual event building via the Level 3 trigger, and any event data used in the trigger decision is retained for future efficiency studies.

The Level 3 trigger contains a flexible combination of tools to reduce backgrounds while keeping the essential physics component. Software performs reconstruction and classification, event selection filters and monitoring. Under nominal background conditions, the output rate to mass storage can be kept to the specified value of 120 Hz of which ~90 Hz is physics and ~30 Hz other categories. An online computer farm makes decisions with software filters that has access to the complete event data, including every Level 1 trigger output. The Level 3 system operates a hierarchy of increasingly complex algorithms to obtain more and more accurate precision on track parameters from the Level 1 trigger track segments, the drift chamber hits and the silicon vertex tracker hits. Classifications are used to flag events as passing or failing criteria for cosmic rays, particular events and so on. The Level 3 trigger does not significantly reduce the efficiencies delivered by Level 1, and allows better rejection of beam background. Flags for events accepted by Level 3 are retained for offline reconstruction and analysis, and L3 output lines are based on these. Any L3 output line passing all necessary event criteria is stored for full reconstruction and offline processing. Total  $B$  event efficiency of the trigger systems is over 99%, which can be checked due the independent nature of the sub-system Level 1 triggers. A typical Level 3 trigger event display for a multi-hadron event can be seen below in figure 19.

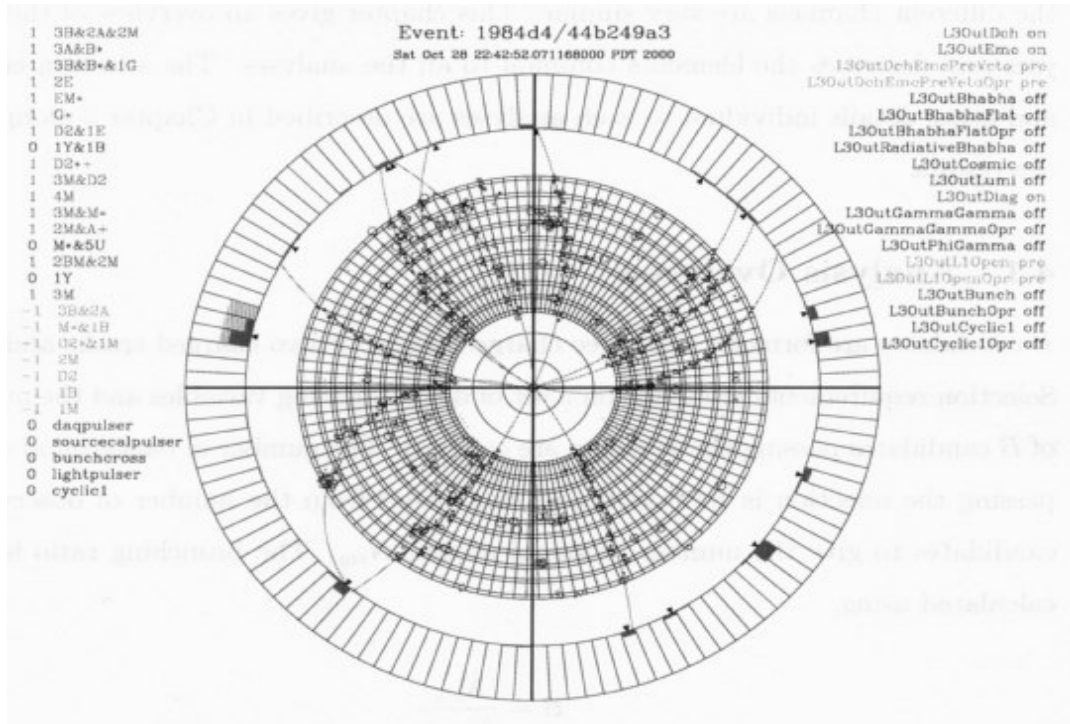


Figure 19: A multi-hadron event as shown on the Level 3 trigger event display. We see the Drift chamber circular hits and the EMC bar hits, along with Level 3 tracks. Bit status of L1 outputs are on the left side while the L3 output status is listed on the right.

# Chapter 4

## Method of Analysis

### 4.1 Introduction

There exist several analyses techniques for determining the branching fractions and any charge asymmetries of decay channels. This chapter will focus on the "cut and count" based analysis method and provides an overview of elements common to general cut and count analyses. The principal decay mode studied in this thesis is  $B^\pm \rightarrow \rho^0 \pi^\pm$  with  $\rho^0 \rightarrow \pi^+ \pi^-$ . Upper limits on these branching fractions have been previously published with a world average of  $B^\pm \rightarrow \rho^0 \pi^\pm$  at  $(8.6 \pm 2.0) \times 10^{-6}$  and  $\rho^0 \rightarrow \pi^+ \pi^-$  fraction giving  $\sim 100\%$  [18]

The  $B^+$  meson consists of  $u\bar{b}$  quark components, decaying to the particular  $u\bar{u}$  and  $d\bar{d}$  mixture known as  $\rho^0$  and the  $u\bar{d}$  bound quark state of the  $\pi^+$ . Analogously the  $B^-$  consists of a  $b\bar{u}$  quark arrangement which decays to a  $\rho^0$  and also a  $\pi^-$  containing  $d\bar{u}$  quark and antiquark. In both these  $B$  decays, the  $\rho^0$  further decays into a  $\pi^+ \pi^-$  pair. The diagrams below illustrate the mechanism of decay for tree and penguin processes:

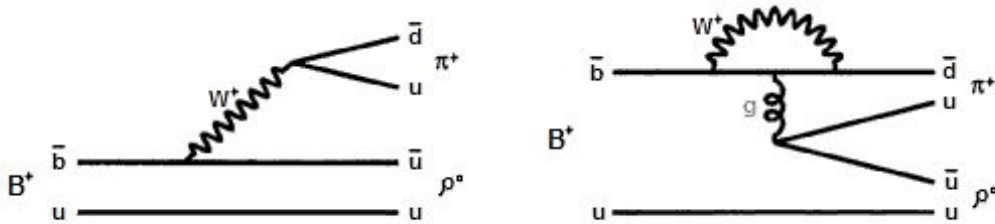


Figure 20: Tree and penguin decay processes for  $B^+ \rightarrow \rho^0 \pi^+$

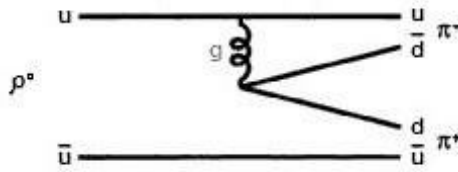


Figure 21: Decay process for  $\rho^0 \rightarrow \pi^+ \pi^-$

The importance of the  $B^\pm \rightarrow \rho^0 \pi^\pm$ ,  $\rho^0 \rightarrow \pi^+ \pi^-$  decay mode is seen in the context of the mixing matrix element magnitudes discussed in chapter 2. Decays proceeding through  $b \rightarrow du\bar{u}$ , including 2,3 and 4 pion modes, provide a method for extracting the unitarity angle  $\alpha$  between  $V_{ub}^* V_{ud}$  and  $V_{tb}^* V_{td}$ . Precise measurements of branching fraction and charge asymmetry for the  $B^\pm \rightarrow \rho^0 \pi^\pm$  decay in question will aid understanding of the strong phase and help in constraining  $\sin(2\alpha)$ . The analysis of charmless hadronic three body decays is an area of interest for several reasons. Tree diagram amplitudes in charmless decays are the same order of magnitude as penguin loop contributions, thus allowing potential observation of significant CP violation. Charmless decays also provide a good possibility of studying these penguin processes and furthermore of measuring each angle of the unitarity triangle. Nevertheless the small size of the branching fraction with a relatively high number of contaminant events ensures that obtaining accurate measurements is not a simple task.

## 4.2 Cut and Count Analysis Overview

A branching ratio for a particular mode is obtained from data sets by applying selection criteria to maximize the desired decay signal to background ratio and suppress specific contaminants. An initial selection of data is made by demanding events that contain  $B$  candidates with the required number of charged or neutral tracks. Successive selections are undertaken with discriminating variables such as the  $B$  meson decay product masses, their decay angles and so on. The final number of  $B$  candidates passing these selection filters will have the estimated quantity of background events subtracted. Two essential issues are background characterization for the

estimation and background suppression for the minimization of events not directly related to the branching fraction decay. A branching ratio can be calculated from the equation

$$\frac{N_{signal}}{N_{B\bar{B}}} \epsilon$$

where  $N_{signal}$  is the number of B candidates minus the estimated background events,  $N_{B\bar{B}}$  the initial number of  $B\bar{B}$  pairs and  $\epsilon$  the estimated efficiency factor of signal selection. The quantity  $\epsilon$  is determined by using a Monte Carlo computational model to generate data and applying the same selection cuts as for real data. Care must be taken since the Monte Carlo techniques can only provide an imperfect picture; it is important to measure and correct these imperfections and use control channel cross-checks when correlating any real data selections with our Monte Carlo results. The branching ratio calculation involves two factors of 2 that cancel each other out: while  $N_{B\bar{B}}$  counts the number of B pairs despite the interest in individual B decays, each  $\Upsilon(4S)$  will decay into the required charged  $B\bar{B}$  pair only half the time.

The charge asymmetry  $A_{CP}$  measurement follows the same selection patterns as the branching ratio measurement, although in addition the numbers of positively and negatively charged signal events ( $N_{signal}^+$  and  $N_{signal}^-$ ) need to be estimated separately.

Monte Carlo signal events are typically used to define the channel *signal region*, a region in the plane defined by two uncorrelated kinematic variables with good signal to background separation. B meson reconstruction and initial beam energies give rise to the variables  $\Delta E$  and  $m_{ES}$  which each feature the required powerful discrimination between signal and background [19]. Here,  $\Delta E$  describes the difference between the reconstructed and expected values of the energy of the B candidate so that

$$\Delta E = E - E_{exp},$$

and the beam-energy substituted mass is

$$m_{ES} = \sqrt{E_{exp}^2 - p^2}.$$

In these two latter definitions  $(E, p)$  is the B candidate 4-momentum calculated from daughter products.  $E_{exp}$  is the beam-energy constrained energy of the B candidate in the lab frame calculated from the 4-momentum  $(E_{beam}, p_{beam})$  of the beams to give a daughter-mass-independent energy of the B candidate in the lab frame:

$$E_{\text{exp}} = \frac{E_{\text{beam}}^2 - p_{\text{beam}}^2 - 2(p_{\text{beam}} \cdot p)}{2E_{\text{beam}}}.$$

In accordance with BaBar analysis policy, the studies are conducted using a blind analysis technique [20]. This means that we must not extract information for any real data contents within the defined signal region while event selection is underway. Such a blind technique will reduce the risk of an experimenter biasing his or her individual results towards prior results or theoretical predictions; the experimenter makes a decision to finish analysis based on external criteria for optimizing the analysis. Thus the Monte Carlo sample is used to define the expected signal distributions, and our use of data is restricted to the task of providing a background representation extrapolated to the signal region where direct observation is not permitted before the decision to "un-blind". The usual boundaries for the signal box are 3 standard deviations from the fitted epicentre of Monte Carlo events in  $\Delta E$  and  $m_{ES}$ , and as such the signal box size is particular to each mode. We typically extend the blind area around the signal region slightly in order to eliminate any chance of influence by boundary signal events. The general area around the signal region is used for the twin purposes of selection optimization and background characterization. We consider random continuum events and  $B$  backgrounds which occur when physically similar decay channels produce reconstructed candidates in the signal region. The latter background studies are typically done by using Monte Carlo simulation to consider contributing channels in isolation and subtract any scaled impacts.

An event occasionally has multiple  $B$  candidates, and one straightforward solution is to select a random candidate from the list. More efficient results may be obtained in other ways; generally the method for resolving ambiguities will depend on the decay channel in question.

Selection criteria are optimized for the decay channel by maximizing the value  $S/\sqrt{S+B}$  over a series of varying cuts, where  $S$  is the number of signal events and  $B$  the number of background events we estimate finding in the signal region. Once we have our optimal cuts and a thorough confidence of the methods employed, values of branching ratio and charge asymmetry are declared and then checked against a now unblinded signal region.

Several types of data are employed in measuring a branching fraction. The large on-peak data set for the  $\Upsilon(4S)$  resonance at PEP-II corresponded to a quantity of  $B\bar{B}$  pairs reconstructed, hopefully containing a significant number of decays in the channel of interest. Half of the  $B\bar{B}$  pairs

produced are  $B^+B^-$  and half are  $B^0\bar{B}^0$  events. Offpeak data at  $40 \text{ MeV}/c^2$  below the  $\Upsilon(4S)$  centre of mass were also taken in the same period as the on-peak collection, and these offpeak data can be used to help understand the typical continuum backgrounds in our analysis of a particular decay channel. Such continuum background can be generally taken as unaffected by the small beam energy difference between the on and off peak runs. A sizable portion of channel-specific Monte Carlo events together with some generalized  $e^+e^- \rightarrow q\bar{q}$  continuum background, charmless samples and  $B\bar{B}$  generated events are generated to determine the calibration, distributions and efficiencies for our branching fraction measurement.

### 4.3 Event Preselection

The branching fraction of decay channels under study can be extremely small e.g.  $10^{-6}$ , and the development of tools and techniques for discriminating a signal from background becomes a central issue. Extensive studies of backgrounds have been undertaken in previous experiments yet issues are often particular to the equipment and the channel investigated. A number of traditional methods have been retained but the BaBar collaboration has developed some unique discriminating tools specifically for the environment at the SLAC detector.

Two major groupings of background occur: (i) the dominant  $e^+e^- \rightarrow q\bar{q}$  continuum production wherein background arising from differing processes can possess identical signal properties to the events in our channel of study and get reconstructed as such, and (ii) a smaller level of background from  $B$  decay channels that share some characteristics with the decay of interest. A machine background due to beam gas interactions, synchrotron radiation and particle scatterings increases the occurrence of low energy clusters in the EMC to create extra combinatorial background. This latter machine background can be generally treated as insignificant for analysis techniques in comparison to the two main backgrounds when filtering with a charged track preselection.

The application of background suppressors to an analysis at BaBar is founded on the idea of adding any required channel-specific discriminating variables to a base of general variables. The initial step is that of filtering the data with preliminary cuts in order to extract relevant subsets; a balance must be struck between the obvious desirability of smaller, more manageable datasets and

the importance of retaining maximum numbers of interesting events. Candidate particles are created from reconstructed detector information and are tagged as either charged, including any relevant EMC, IFR and DIRC information, or as neutral from isolated EMC bump measurements. These candidates, known as BetaCandidates, have characteristics restricted to spatial track information, associated EMC or IFR bumps, and a small number of other variables. The lists of charged or neutral BetaCandidates may be further refined and divided into various groupings such as composite candidates. These BetaCandidates are combined to form  $B$  candidates which are then stored in an ntuple format subject to discriminating variables passing very loose selection criteria, with the possibility that multiple  $B$  candidates can exist in an event. This stage of analysis is known as preselection. We save much computing time by then applying the end selection requirements and checks to these ntuples in a second stage of analysis. The resulting ntuple contains a useful subset of the reconstructed track or cluster parameters plus the analysis-specific quantities calculated in the pre-analysis reconstruction. A key point about the ntuple is that one can perform analysis interactively, rather than by running batch jobs, awaiting results, modifying the code or cuts and rerunning in a cycle.

One common charmless hadronic three-body filtering list used in the preselection stage selects likely  $B^\pm$  decays to final states of three charged tracks, whereby all distinct combinations of three candidates passing loose track criteria (described in the next section) have pion and kaon charged particle mass hypotheses tested on each track. The imperfect selection criteria of the filter unavoidably causes the inclusion of a level of  $q\bar{q}$  background that must be eliminated if we are to achieve a good accuracy in measuring a decay channel branching fraction. The main losses of signal efficiency are in the detector acceptance and track reconstruction, resulting in a signal purity for on- or off-resonance data of around 1.5%. The following preselection requirements are made for each reconstructed  $B$  candidate:

- The total charge of the  $B$  candidate is equal to  $\pm 1$ .
- Beam-energy substituted mass  $m_{ES}$  lies within  $0.1 \text{ GeV}/c^2$  of the  $B$  meson mass  $m_B$ , the kinematic end-point generally set at  $5.29 \text{ GeV}/c^2$ . We do not need to consider the mass hypothesis for the final state particles here.
- $|\Delta E| < 0.45 \text{ GeV}$ .  $\Delta E$  is the difference between the reconstructed energy of the  $B$  candidate

and expected energy, and the constraint is tested against all track mass hypotheses in the final state since  $\Delta E$  is dependent on the daughter mass combinations. Any mass hypothesis passing the selection is a sufficient condition to pass the whole event.

- Events contain more than three GoodTracksLoose tracks (see next section). The acceptability of four or more tracks in an event means that at least one track comes from the other B meson, and we can use this extra information in later analysis.
- The total event energy is less than  $20 \text{ GeV}$  to eliminate completely unfeasible track combinations from a bad reconstruction.

Batch level pre-analysis processing uses the output from this skimmed data and applies some refinements that were not possible to implement previously due to the processing overhead. Typical Batch level event selection efficiencies for charged data in on and off resonance tuples are around the 95% mark since the criteria used in selection is either similar to that used in the earlier data skims or has very loose requirements. Particle identification selectors are run over each track for future analysis though the use of particle identification or resonance selection cuts is avoided. These selectors test for electrons, muons, pions and kaons; the latter two particle hypotheses are checked on a number of differing efficiency and purity characteristics. A simple quick vertex fit is formed from adding four-momenta of charged decay tracks of the  $B$  candidate, and subjected to a very loose cut of  $\chi^2 < 200$  with a refitting to possibly improve daughter energy and momentum resolution. Such a cut thereby eliminates the inclusion of candidates produced using any completely unrelated tracks while maintaining a good signal efficiency. The vertex refitting places a demand that the  $\Delta E$  is also recalculated and again required to pass the  $|\Delta E| < 0.45 \text{ GeV}$  cut for one of the mass hypotheses. Mass and decay angles of all combinations of two  $B$  meson daughters are calculated in order to reconstruct and vertex any intermediate resonance candidates. An additional requirement is that the magnitude of cosine for the angle between the  $B$  candidate momentum and thrust axis of the rest of the event particles in the centre-of-mass frame is less than 0.95, significantly helping to reduce continuum background. In total a large number of variables are stored in ntuple format with information relating to the whole event, tracking,  $B$  candidates and the two particle combinations deemed as potential resonance composition.

## 4.4 Track Selection

Track selection starts when tracks reconstructed from hits in the drift chamber are projected into the SVT and associated with SVT hits. Any suitable SVT hits outside the drift chamber projections may be accommodated into a track selection following the use of an SVT specific tracking algorithm.

We use the SVT for production of tracking efficiency tables as the GoodTracksLoose criteria [21] are almost completely dependent on the drift chamber. GoodTracksLoose is one of a subset of flags indicating the severity of track selection limitations applied to datafiles; other GoodTracks subsets are correspondingly named VeryTight, Tight and VeryLoose. General filtering and charged mode-specific preselection from the GoodTracksLoose list mean that  $B$  candidates are reconstructed from tracks consisting of more than two hundred parameters with the following characteristics:

- Track momentum  $p < 10 \text{ GeV}/c$ .
- Transverse momentum  $p_t > 100 \text{ MeV}/c$ .
- Track must have a minimum of 12 hits in the drift chamber.
- Track distance of closest approach to beam spot in  $x - y$  plane  $< 1.5 \text{ cm}$ .
- Absolute distance of track closest approach to beam spot in  $z$  plane  $< 10 \text{ cm}$ . Both distance cuts are far larger than the track resolutions and any  $B$  decay length.

Monte Carlo results have an extremely high efficiency for tracking when tracks meet the criteria of transverse momentum  $p_t > 100 \text{ MeV}/c$ . Signal Monte Carlo requires a reference production of correctional tables in tracking efficiency to be used with real data if we are to accurately estimate efficiency corrections on each track. These corrections take into account a small dependence on the SVT for improving track resolution, another dependence of SVT track efficiency on drift chamber tracking, and any unmatched SVT and drift chamber tracks. This data tracking efficiency has been studied as a function of momentum, polar and azimuthal angles and particle multiplicity in data sets that are separated by differing the drift chamber operating voltages [22] An overall efficiency correction for tracking per event is taken as the product of each efficiency correction per track in the event and averaged over every Monte Carlo event passing all

analysis selection criteria. Our assumptions on measuring the data efficiency contribute a systematic error estimation of 1.2% per track. The tracking charge asymmetry has also been studied with  $D^+ \rightarrow K_S^0 h^\pm$  [23] where  $h$  signifies a pion or kaon. This asymmetry may occur as a consequence of the magnetic field around the drift chamber charge detection wires deviating from a symmetrical pattern and hence causing an uneven distribution of charged tracks from decays. Results from the investigation indicate the tracking asymmetry is under 2% for each track and cancels when an even number of oppositely charged particles emerge from a  $B$  meson decay.

## 4.5 Event Shape Variables

Event shape variables are important in discriminating signal events from the dominant  $q\bar{q}$  continuum background.  $B$  mesons are produced at low momentum and so decay in a roughly isotropic manner in the  $\Upsilon(4S)$  rest frame, with little correlation between daughter directions from each of the two  $B$  mesons. Conversely a  $q\bar{q}$  continuum event generally has a back-to-back dual jet structure along some axis, with lower isotropy and a higher level of directional correlation between any daughter products of suspected  $B\bar{B}$  pairs. A number of factors must be considered in order to discriminate background from signal events by using the event shapes. Global event variables should be calculated in the  $\Upsilon(4S)$  rest frame while variables dependent on decay products use the  $B$  meson rest frame. The definition of the  $B$  meson decay axis in three-body decays depends on the existence of any resonance. In the case of non-resonant decay modes, the probability that decay product momenta are similar in magnitude and will lie on a plane in the  $B$  meson rest frame can prevent definition of any overall direction. Resonances enable consideration of a two-body decay and hence an unambiguous definition of  $B$  decay axis.  $h^\pm h^\mp h^\pm$  ntuple data and generic Monte Carlo data following preselection criteria will vary in distribution due to a selected variable's efficiency in discriminating continuum background from combinatorial events. For example  $\cos\theta_{TTB}$ , the cosine of the angle of the  $B$  candidate thrust axis to the thrust axis of the rest of the event, peaks at  $\pm 1$  due to an overwhelming contribution from the highly correlated jet-like continuum background events. Signal Monte Carlo indicates  $\cos\theta_{TTB}$  as an approximately flat distribution with a slightly increasing slope due to combinatorial background, reflecting the random direction of thrust of  $B$

candidates.

A composite set of functions calculate discriminatory variables and multivariate analysis tools for optimizing background suppression. A design emphasis has been ease-of-use for including and customizing variables specific to a particular channel. All distribution information for each of the generally employed variables and any additional variables requested by the user is packaged together for output as an ntuple.

The ntuples generated from the composite module can have internal variables compared in terms of discriminatory power. It is found that the  $B$  candidate mass and momenta provide highest discrimination, bearing in mind the pre-selection cuts are very loose. An iterative process was undertaken with the best performing variable combined with every other variable in separate processes to determine the pair giving best separation. These two were then tested alongside every other variable in sequence to find the maximum separation, and this process was continued until we had a list of optimal variables for background suppression. Correlation between variables can become a factor, so algorithms are developed to test every combination of variables. Such a procedure is known as training. It is found generally that many variables contain similar information, giving correlation. Pooling information from the iterative and combinational algorithmic studies put us in a position of deciding the best set of variables for use in background fighting.

Our temptation to include a large number of discriminating variables is offset by the knowledge that every extra variable adds a systematic error to the overall measurement. The approach of iterating parameter ranges performs poorly when large correlations exist between particular variables. A neural network method does not have this problem to the same extent at the expense of increased complexity. A wide number of these discriminating variables are deployed for identification purposes, and their proper use depends on the event subset characteristics. For example, the two-body decay direction defining the  $B$  decay axis unambiguously can be approximated in topology for three body decays that have particular resonances. A typical background event for a two body decay will have decay products in back-to-back jets more or less collinear with the rest of the event. In contrast a genuine signal event has a  $B$  decay axis unrelated to the other  $B$  meson which will comprise the rest of the event. Non-resonant three-body events, not

having an identifiable overall direction of decay momenta in the  $B$  rest frame, nevertheless have the sphericity of the decay. This sphericity geometry enables a useful separation between signal and the more jet-like continuum decay structures. Both the two- and three-body decays have a range of detailed kinematic information used extensively for background suppression.

## 4.6 Particle Reconstruction

Particle identification techniques come into play to distinguish pions, kaons and protons. A mixture of DIRC or combined SVT and drift chamber information is used to calculate likelihoods for a candidate to be a pion, kaon or proton and selection occurs according to the likelihood ratios and the BaBar-standard kaon selector *SMSKaonSelector* [24] on a tight cut configuration. This selector combines the  $dE/dx$  information from SVT or drift chamber tracks above  $0.7 \text{ GeV}/c$  momentum together with information on candidates with momentum surpassing  $0.6 \text{ GeV}/c$  when travelling through the DIRC. Controls are used to correct Monte Carlo modelling whereby particle ID performance is tested with sample data. Efficiencies vary with the channel under observation though typically we find when using the pion selector NOT(*SMSKaonSelector* tight) that selection efficiency is around the 95% and 97% mark for data and Monte Carlo samples respectively.

$B^\pm$  modes are formed from three charged tracks using the *BtaFastVertexer* algorithm at the analysis level, where every combination of pion and kaon mass hypotheses is used on each set of tracks. Only the Kalman fit [25] for default pion hypothesis is stored for tracks, and thus the only effect that different mass hypotheses will have is in the energy assignment:  $B$  vertex properties remain identical for the same tracks at this stage of partial reconstruction. Vertices are formed with two or more tracks and are an attempt to find points common to subsets of the tracks in an event. Any CP violation studies depend essentially on the difference in the decay position distribution between  $A$  and  $\bar{A}$  as found with vertexing. A vertex is first produced and then fitted with particular vertex constraints to make a  $B$  candidate, the tracks and also any  $\pi^0$  candidates being re-fitted onto the new vertex. It has been found that a  $\pi^0$  mass constraint has negligible impact in this context, and we use this fact to modify decay product characteristics so that they originate from the vertex.

Reconstruction of  $\pi^0$  particles is often important for study of contaminating channels on any

decay measurement, and the analysis of  $B^+ \rightarrow \rho^0 \pi^+, \rho^0 \rightarrow \pi^+ \pi^-$  requires a consideration of  $\pi^0$  detection for checks on background that may contain  $\pi^0$  contributions. An example possible contaminant in  $B^+ \rightarrow \rho^0 \pi^+, \rho^0 \rightarrow \pi^+ \pi^-$  could be  $B^+ \rightarrow \rho^0 \rho^+, \rho^0 \rightarrow \pi^+ \pi^-$  where  $\rho^+ \rightarrow \pi^0 \pi^+$ . In order to efficiently reconstruct B decays to three hadrons in the final state which may additionally include a  $\pi^0$ , we need to identify  $\pi^0$  candidates across the full EMC momentum range  $0.1 \text{ GeV}/c$  to  $\sim 4 \text{ GeV}/c$ . The  $\pi^0$  selection has candidates in which the constituent photons are fully resolved (two bumps in different clusters), partially resolved/merged (two bumps within the same cluster) or fully merged (cluster with a single bump). We handle cases of resolved and merged  $\pi^0$  differently to optimize use of available information. A cluster is the energy deposit caused by one or more particles interacting in the calorimeter, and a bump is created from a local maximum within the cluster such that it represents the fraction of the cluster energy deposit caused by a single particle interaction as described fully in the EMC section of the previous chapter.

Resolved  $\pi^0$  selection uses the “pi0Loose” list, formed from pairwise combinations of all bumps in the calorimeter which pass photon energy and with mass cuts and are not associated to a charged track. The invariant mass of a combination is formed assuming that the photons originated at the nominal origin, with the combination mass required to lie within the range  $80 - 200 \text{ MeV}/c^2$ . At this stage of the analysis we use a loose initial selection based on simple criteria and retain information provided by the  $\pi^0$  invariant mass distribution. Mass and photon energy cuts improve our ability to estimate background and purity in the distribution. Merged  $\pi^0$  candidates from the “pi0MergedDefault” list and are selected from calorimeter clusters with energy greater than  $0.9 \text{ GeV}$  which are not associated to a charged track. Additionally the second moment S of the cluster is used as a discriminating variable and is proportional to the mass of the incident particle. We define S for n crystals of distribution of energy E resulting from incidence angles  $\theta$  and  $\phi$  as

$$S = \frac{\sum_{i=0}^{i=n} E_i (\Delta\alpha_i)^2}{\sum_{i=0}^{i=n} E_i}, \text{ with } \Delta\alpha_i = \begin{pmatrix} \frac{(\sum_{i=0}^{i=n} E_i \theta_i)}{\sum_{i=0}^{i=n} E_i} - \theta_i \\ \frac{(\sum_{i=0}^{i=n} E_i \phi_i)}{\sum_{i=0}^{i=n} E_i} - \phi_i \end{pmatrix}.$$

A nominal  $\pi^0$  mass is applied as a constrained fit on  $\pi^0$  candidates.

The lists of candidates from the two selectors are combined into a single list and a checked for

the presence of any duplicates (candidates having all their calorimeter bumps in common) whereby partially-resolved/partially-merged candidates have been successfully reconstructed by both selectors. When a pair of duplicates is found, only the composite candidate is kept. Any candidates which partially overlap by sharing some, but not all, common bumps are legitimate combinations. This process effectively removes all two-bump merged  $\pi^0$ . The significance of including merged  $\pi^0$  in the selection is decay mode dependent: polarized resonances have a maximum in the  $\pi^0$  distribution at extreme ranges of momentum, which increases the likelihood of more fully-merged  $\pi^0$  signal particles than in the case of modes with no polarized resonances. Agreement in efficiency between data and Monte Carlo is within 5% over the full kinematic range.

In the case of  $B$  decays to final states formed from a pseudoscalar and a vector meson, the vector meson will be polarized. This fact can be used when studying the angular distribution of the vector meson decay products to distinguish between signal and background. The cosine of the angle  $\theta$  between the decay angle and the line of flight for the vector meson, known as the helicity angle, has signal events distributed according to  $\cos^2\theta$ , while background should be essentially flat. Thus a cut on  $|\cos\theta|$  has an effect on signal to background ratio for  $B$  meson decay modes involving an intermediate resonance.

The  $\rho$  candidates are reconstructed by combining pairs of appropriately charged tracks and/or  $\pi^0$  using the *BtaFastVertexer*, with the charged tracks assigned with a  $\pi^\pm$  mass and requiring that the combination have an invariant mass sufficiently close to the  $\rho$  Particle Data Group value. Precise requirements for the invariant masses are analysis-dependent though in general a narrow resonance has a nominal value extracted from data while wide resonances such as the  $\rho$  are referenced to the study group table values. A calculation of resonant mass results from 4-vector addition of candidate daughters, and this is then fitted with a Breit-Wigner or double Gaussian fit prior to any resolution constraints.

## 4.7 Background Characterization

Several methods exist that enable us to characterize background. It is possible to measure the number of events in the signal region for off-resonance data or light quark continuum Monte Carlo.

Both methods are useful as cross-checks though presently unlikely to give a sufficient estimation of background in the signal region: off-resonance data has not been produced in adequate quantities for characterization involving analyses with low branching fractions, and Monte Carlo does not model data to the required degree of accuracy. So we must count on-resonance event measurements in some sideband region of the  $\Delta E : m_{ES}$  plane and extrapolate to our signal region. Using the whole data set to conduct both background characterization and selection optimization induces a risk of biasing our results, which would happen if the optimization point occurred within a statistical fluctuation of the background and the implications were carried over to a branching ratio measurement. Therefore to bypass the problem that the selected events used in background characterization must not be used in the selection optimization process we use every odd event in the data sample for characterization and every even event for the optimization process.

Background can be separated into two categories. The dominant source is from random combinatorial processes, although it is the quantitatively smaller background from various B decay channels that ultimately requires greater consideration in our calculations.

We can estimate the level of combinatorial background that would be found in our blinded signal region by using the Grand Sideband (GSB). This GSB is a designated large region in the  $\Delta E - m_{ES}$  plane with an  $m_{ES}$  maximum value lower than the blind box  $m_{ES}$  value boundary.  $\Delta E$  and  $m_{ES}$  have a very low correlation, permitting the characterization of the background shape through separate  $\Delta E$  and  $m_{ES}$  fitting procedures. The number of background events in the GSB is counted and multiplied with the relative area ratio of signal region to GSB. This characterization gives an estimate of the amount of generalized background within the blinding box. The  $m_{ES}$  fits are checked in two distinct areas across the boundary  $5.2 < m_{ES} < 5.3 \text{ GeV}/c^2$ ; an *upper sideband* region between  $0.1 < \Delta E < 0.3 \text{ GeV}$ , and a *lower sideband* region within the range  $-0.3 < \Delta E < -0.1$ . A  $\Delta E$  fit is applied on the events that lie within the *GSB* area with defined boundaries of  $5.20 < m_{ES} < 5.27 \text{ GeV}/c^2$  and  $-0.3 < \Delta E < 0.3 \text{ GeV}$ . Most combinatorial background comes from continuum events, and we hence use continuum MC as well as off-resonance data for characterization. Both the MC and off-resonance data use the region  $5.2 < m_{ES} < 5.29 \text{ GeV}/c^2$  and  $-0.3 < \Delta E < 0.3 \text{ GeV}$  for the  $\Delta E$  and  $m_{ES}$  fitting procedures as the blind box limitation is only imposed for on-resonance data. A figure showing the areas in the

$\Delta E - m_{ES}$  plane considered for on-resonance background characterization can be seen below:

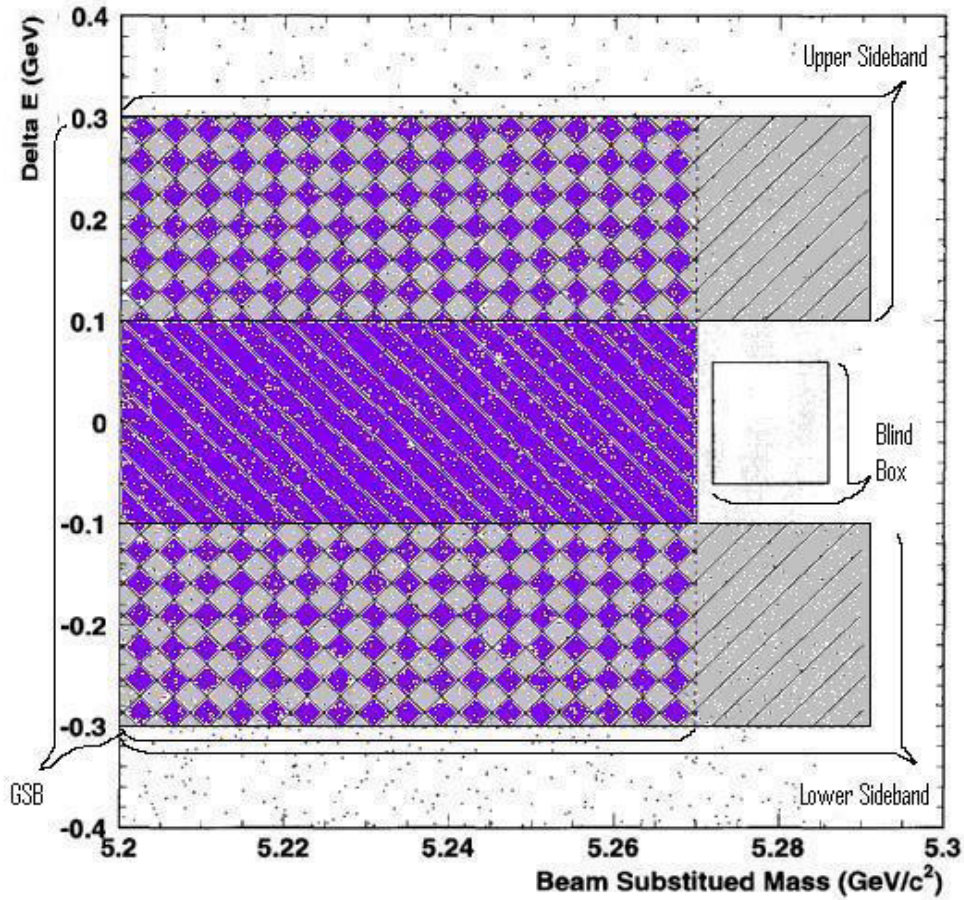


Figure 22: Forward-striped and backward-striped regions indicates areas used for  $m_{ES}$  and  $\Delta E$  characterization respectively.

Characterization of  $\Delta E$  background shape is usually achieved with a first or second order polynomial function. No significant difference between polynomials was found in the  $\Delta E$  fitting of the specific mode channel, and so a first order polynomial  $ax + b$  is used for the simplicity of avoiding possible asymmetry issues about the centre point in the fitting of the distribution.

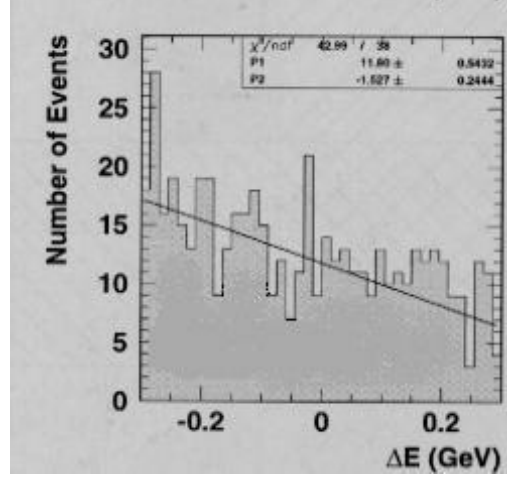
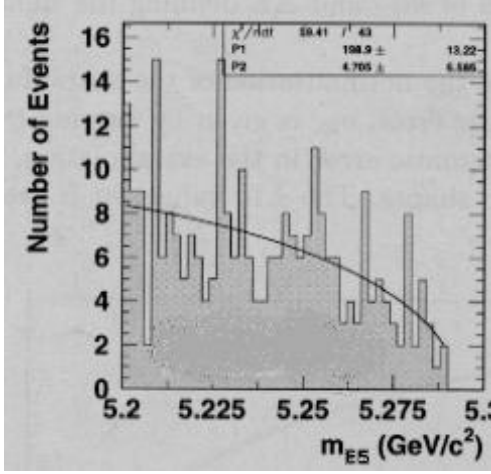
The Argus function [26] is

$$\frac{dN}{dx} = Ax\sqrt{1-x^2} \exp[-\varepsilon\sqrt{1-x^2}], \text{ with } x = \frac{m_{ES}}{m_{end}}$$

where  $m_{end}$  is the maximum possible mass point, with the normalization parameter  $A$  and background shape parameter  $\varepsilon$  determined by the fit. It is used as a fit for the  $m_{ES}$  upper, lower and combined distributions, and we can extract the useful parameters for a calculation of the combined ratio for both the  $\Delta E$  and  $m_{ES}$  fits. Figures 23 and 24 show fits applied to typical analysis distributions. The working equations follow the formats for the variables  $x_{Mes}$  and  $x_{\Delta E}$  signifying

the bin value in the  $m_{ES}$  and  $\Delta E$  planes respectively to calculate the combination ratio  $R$ :

$$\frac{\int_{SR_{leftmost}}^{SR_{rightmost}} Ax_{Mes} \sqrt{1-x_{Mes}^2} \exp[-\epsilon \sqrt{1-x_{Mes}^2}] dx_{Mes}}{\int_{GSB_{leftmost}}^{GSB_{rightmost}} Ax_{Mes} \sqrt{1-x_{Mes}^2} \exp[-\epsilon \sqrt{1-x_{Mes}^2}] dx_{Mes}} \times \frac{\int_{SR_{lowermost}}^{SR_{uppermost}} (ax_{\Delta E} + b) dx_{\Delta E}}{\int_{GSB_{lowermost}}^{GSB_{uppermost}} (ax_{\Delta E} + b) dx_{\Delta E}} = R$$



The figures 23 and 24 above show the relevant optimization fits applied on typical  $m_{ES}$  and  $\Delta E$  characterization regions.

Alterations in selection criteria are applied to improve these fits through increased statistics, although care must be taken to ensure the background shape remains consistent with that found from the optimization cuts. We check on-resonance data, off-resonance data and continuum MC for stability across varying conditions of  $\Delta E$  and  $m_{ES}$  fits. Specific  $B$  decays may peak in the sideband background and give a misleading fit for characterization extended to the signal region, and so we fit generic and non-charm (rare) MC  $B$  data alongside the continuum events in order to determine the extent of any specific channel effects.  $B$  meson background requires careful study because even small background contributions from other charmless hadronic decays can have a significant impact on a statistically low signal. If particular non-specific decay channel samples show events in the signal region after passing the specific decay mode criteria then we determine the selection efficiency for that mode and use a branching fraction recommended by the Particle Data Group [18] to approximate the number of channel events in the signal region of the on-resonance data set. These contamination events require subtraction from the total number of events found when we finally uncover the signal region.

We use positively and negatively charged events individually for background subtraction after

application of the standard selection and background criteria in order to give separate  $N_{signal}^+$  and  $N_{signal}^-$  charged signal event estimates. These latter values are essential for the determination of asymmetry  $A_{CP}$  in the charge conjugates of a channel, as calculated from the equation

$$A_{CP} = \frac{N_{signal}^+ - N_{signal}^-}{N_{signal}^+ + N_{signal}^-}$$

## 4.8 Selection Optimization

We maximize the signal to background ratio  $S/\sqrt{S+B}$  using only even events from the data set in order to remain unbiased. The number of signal events  $S$  we would estimate finding in the signal region are predicted using the formula  $S = \sigma L B_R \epsilon$ , where  $\sigma$  represents the  $B\bar{B}$  cross section,  $L$  the beam luminosity,  $B_R$  the reference branching fraction of the decay mode in question, and  $\epsilon$  is the efficiency of the mode specific MC in passing all the optimized selection cut criteria. Our background  $B$  in this case is the number of events counted in the GSB region multiplied by the scaling ratio value  $R$ . All of the selection criteria already covered in previous sections of this chapter is applied on a final ntuple production whereby the preselected datasets are processed with a selection optimization requiring three charged track candidates in order to further reduce the dataset size without incurring loss of any events of interest. We test cuts for:

- MC signalB truth match flag for B candidates where a reconstructed B candidate is matched to a "true" produced B meson.
- Cosine of the thrust angle  $\theta_{TTB}$  relative to the  $B$  direction
- Cosine of the helicity angle, the angle between the decay axis in the  $\rho^0$  rest frame and its momentum in the  $B$  meson rest frame.
- Fisher discriminant, an assignment of probability for each event to come from a  $b$  or  $\bar{b}$  quark and subsequent final event asymmetry likelihood.
- Energy over momentum ( $E/p$ ) ratio for electron veto
- Pion particle identification, a NOT(SMSKaonSelector Tight) veto with various subdetector criteria [27]
- Resonant mass width and charge combination
- Chi-squared value of B vertex fit

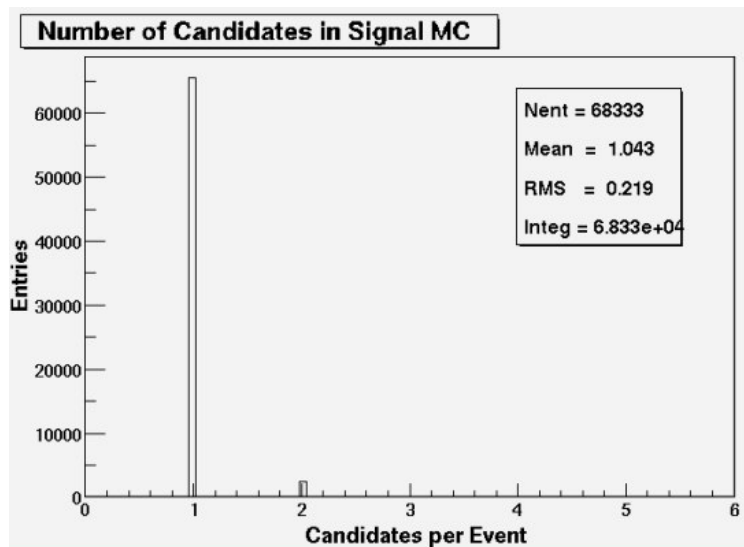
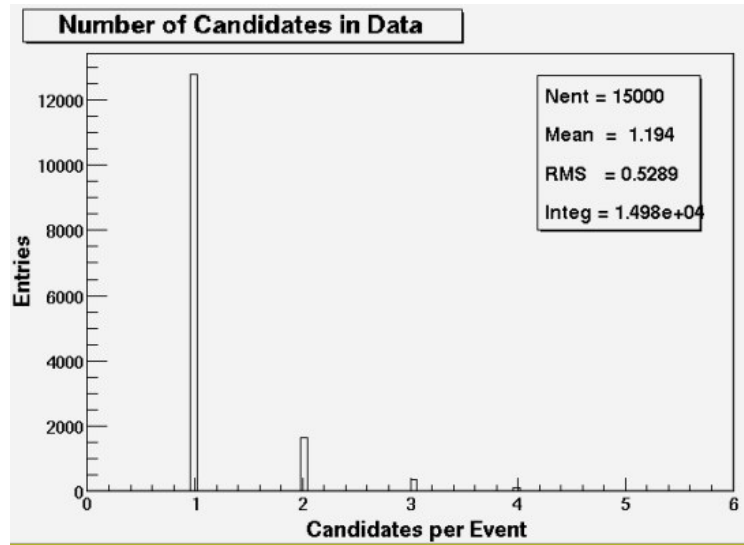
Initial optimization consists of looping selections over incremental values of a single cut and fine tuning the output  $S/\sqrt{S+B}$  optimal result. When optimal values of each cut are found then several cuts are varied simultaneously to assess their level of correlation. At this time there is a high likelihood of new optima being found for highly correlated variables. Care must be taken to not cut too harshly in spite of increases in the value of  $S/\sqrt{S+B}$ , since we have the dual purpose of keeping a maximal absolute number of signal candidates with the occasionally contradictory goal of an optimal  $S/\sqrt{S+B}$ . Cuts on the kinematic variables  $\Delta E$  and  $m_{ES}$  are not optimized due to the uncertainty in Monte Carlo modelling. A standard procedure for dealing with  $\Delta E$  and  $m_{ES}$  involves setting cuts of 3 standard deviations on the Monte Carlo signal distribution width in the  $\Delta E$  and  $m_{ES}$  plane. The size of these cuts is sufficient to maintain a low systematic error from the modelling uncertainty while inhibiting the inclusion of significant background events. Potential efficiency corrections arising from the kinematic cuts must be estimated with control samples. The control samples are decay modes similar in kinematics yet having a far larger branching fraction than the decay channel of interest. Applying all analysis cuts to the control channel under study will highlight any inconsistencies between the expected data and the Monte Carlo distributions, and the efficiency corrections found are then passed on to the main branching fraction analysis.

# Chapter 5

## Analysis Results

### 5.1 $B^+ \rightarrow \rho^0 \pi^+, \rho^0 \rightarrow \pi^+ \pi^-$ Initial Results

The analysis described in this chapter uses ntuples that are derived from BaBar processed datasets of  $81.402 \text{ fb}^{-1}$  on-resonance data corresponding to 88.9 million  $B\bar{B}$  events and  $9.579 \text{ fb}^{-1}$  off-resonance data of 10.5 million events  $40 \text{ MeV}/c^2$  below the  $\Upsilon(4S)$  resonance centre-of-mass energy, as concluded from a B counting study based on the procedure described in [28]. Loose selection cuts are used initially to determine the  $\Delta E$  and  $m_{ES}$  signal shapes. This required preparation of 329000 signal Monte Carlo events for the  $B^+ \rightarrow \rho^0 \pi^+, \rho^0 \rightarrow \pi^+ \pi^-$  specific analysis using the BaBar analysis 12.5.2b release. After some test analyses the on-resonance ntuples were reprocessed and reproduced following a  $\cos \theta_{TTB} < 0.70$  cosine of the thrust angle selection cut on all entries in order to further reduce the on-resonance data collection to a more manageable size. Each event contains at least one candidate, and any event that passes the selection criteria containing multiple candidates will have a sole candidate randomly picked for the subsequent analysis. Table 1 below shows the impact on selection efficiency from each successive analysis cut and gives a total overall efficiency. A mean number of candidates check after initial selection cuts gives a candidacy in Monte Carlo of 1.04, rising to 1.19 in data and thus demonstrating the need for candidate selection. Multiple candidates that pass all selections can occur in either a background or signal event. Needless to say that the presence of several passing candidates in a signal event gives an additional possibility of an incorrectly reconstructed  $B$  event, and this can distort our analysis measurements including those on  $\Delta E$  and  $m_{ES}$ . The number of events with more than one qualifying candidate were found to be of the order of several percent. It is seen from figures 25 and 26 of the candidacy histograms of candidates per event after initial cuts that the number of multiple candidate events quickly falls to zero with increasing multiplicity.



Figures 25 and 26: Multiplicity after initial cuts in on-resonance data and Monte Carlo events

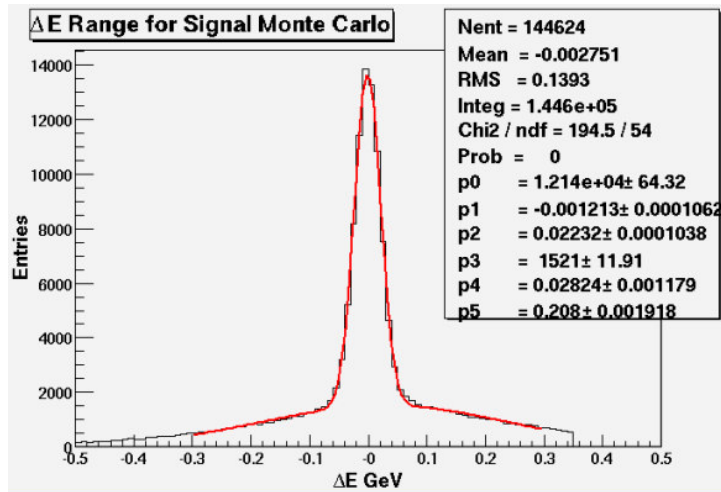
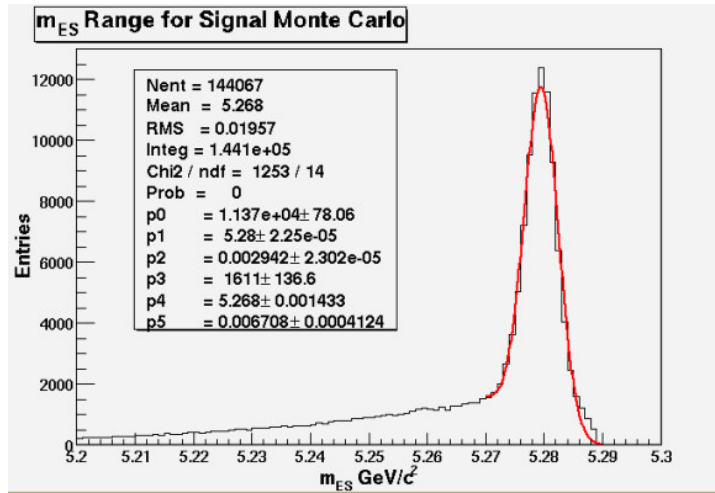
Efficiency here is obtained by dividing the total number of events containing at least one candidate that passes a specific selection cut by the total number of events used as input for the selection; for Monte Carlo these can lie within the signal region yet data studies follow the blind guidelines to exclude the signal region and thus give an indication of background efficiency. Several event shape variables are shown in figures 30 to 33 for comparison between the mode specific Monte Carlo and background events in the data sets. Table 1 below shows the effects on efficiency from a set of unoptimized cuts sourced from earlier cut and count studies [29]; these cuts are predicted to be conservative for the current dataset in question due to the far larger number of likely signal events although useful for comparison. Note several points: 1) On-resonance data has

the  $\Delta E : m_{ES}$  signal region background efficiencies of expected candidates extrapolated from the sidebands using area and fit ratios 2) Off-resonance data has the centre-of-mass beam energy decreased  $0.04 \text{ GeV}/c^2$  below the  $\Upsilon(4S)$  resonance, and so  $0.02 \text{ GeV}/c^2$  is added to  $m_{ES}$  off-resonance beam energy substituted mass of B candidates prior to counting events 3) Off-resonance data has the three charged track selector applied to an ntuple production while the on-resonance ntuples used were the full dataset for a more accurate selection comparison with Monte Carlo. We see the potential misleading effect on dataset correlation from preselected reduced ntuples where the off-resonance efficiency values in table 1 correspond reasonably only after several selection cuts 4) Multiple candidate selection takes place in both Monte Carlo and data *after* all other cuts have been successively applied as otherwise the random selection process is more likely to drop good signal candidates. It can be seen in the table that signal Monte Carlo has a preselection efficiency greater than 1 due to the presence of multiple candidates in a number of events. UDS Combinatorial refers to a generalized Monte Carlo production of the light quark pair production; useful as a check for the impact of the selection criteria on the dominant continuum background. Considerations must be taken into account due to the availability of extra data as compared to previous studies of this mode, and an early decision resulting from preliminary measurements was not to include the Monte Carlo "signalB" truth match. This truth match in Monte Carlo returns a positive or negative truth match result when a reconstructed  $B$  candidate is matched to a "true"  $B$  meson produced in the ntuple. The justification for this exclusion is that as we cannot require such a truth match in on-resonance data; the exclusion establishes a greater degree of correlation between Monte Carlo and data selection criteria. Including a signalB truth match increases the Monte Carlo  $\Delta E$  and  $m_{ES}$  cut efficiencies to around 94% and 98% respectively. Efficiency of events passing the selection criteria are shown in table 1.

Cut variable	Signal MC	UDS Combinatorial	On-res data	Off-res data
Reconstruction & preselection	1.807	0.989	0.021	0.223
$ \cos\theta_{thr}  < 0.6$	0.516	0.072	0.645	0.048
$\chi^2 < 25$	0.897	0.916	0.860	0.867
Has no tight Kaon	0.892	0.675	0.530	0.554
$E/p < 0.9$	0.959	0.936	0.870	0.882
FisherCrn < -0.2	0.808	0.476	0.518	0.473
$0.52 < mass_\rho < 1.02$	0.783	0.542	0.483	0.511
Helicity > 0.3	0.983	0.780	0.812	0.787
$ \Delta E  < 0.05$	0.600	0.089	0.044	0.089
$5.272 < m_{ES} < 5.286$	0.525	0.099	0.030	0.092
Overall efficiency	0.234	$8.416 \times 10^{-5}$	$5.150 \times 10^{-6}$	$7.744 \times 10^{-6}$

Table 1: Initial selection criteria for  $B^+ \rightarrow \rho^0 \pi^+, \rho^0 \rightarrow \pi^+ \pi^-$  detailing efficiencies of successive cuts

Monte Carlo  $\Delta E$  and  $m_{ES}$  distributions following selection prior to  $\Delta E$  and  $m_{ES}$  cuts are fitted to double Gaussians, and the standard deviation values of the narrower Gaussian (polynomial parameter p2) in each case are used to define the dimensions of a signal box for an on-resonance data veto. These fits are shown in figures 27 and 28. The signal box size is  $3\sigma$  from the peak point (polynomial parameter p1) in both  $\Delta E$  and  $m_{ES}$  planes, with the blind box overlapping at  $3.5\sigma$  in each direction. Hence the optimal signal region is bounded by  $|\Delta E| < 0.067$  and  $5.270 < m_{ES} < 5.288$ , the blind box dimensions are  $|\Delta E| < 0.078$  and  $5.267 < m_{ES} < 5.291$  while the grand sideband spans  $|\Delta E| < 0.300$  and  $5.200 < m_{ES} < 5.268$ . The resulting shapes are shown in the  $\Delta E : m_{ES}$  plane in figure 29 prior to the  $\Delta E$  and  $m_{ES}$  cuts alongside an appropriately sized grand sideband region.



Figures 27 and 28:  $m_{ES}$  and  $\Delta E$  signal Monte Carlo distributions for initial set of cuts

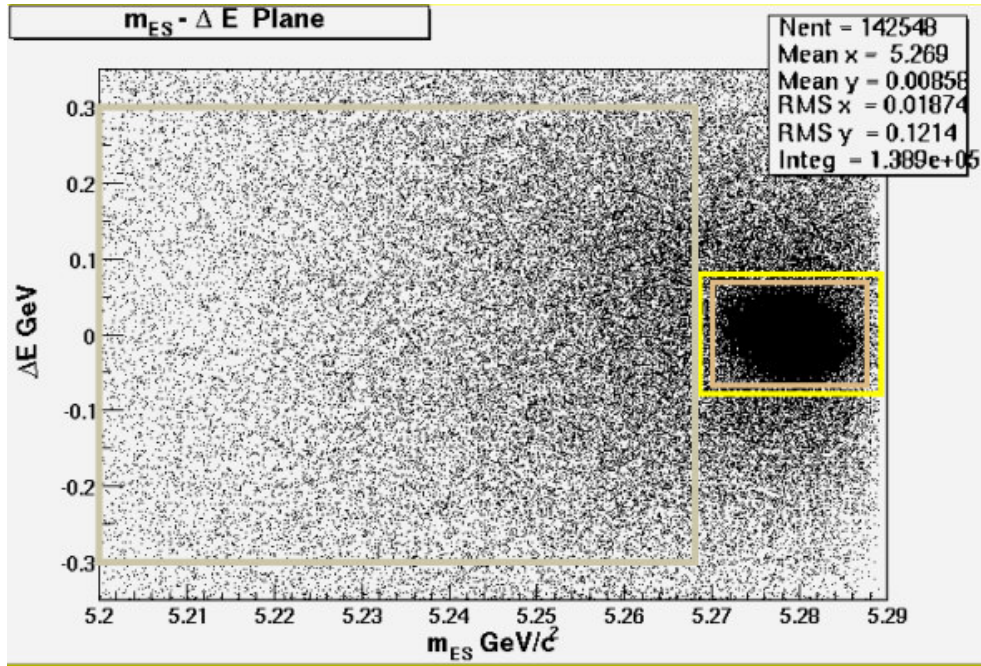


Figure 29:  $\Delta E : m_{ES}$  plane for signal Monte Carlo with signal, blind and GSB region boxes

Event shape distributions with initial cuts can provide us with some level of knowledge about the likely effects of our cuts, the discrepancies between data and signal Monte Carlo, and opportunities to focus on particular cuts or seek out further selection criteria. A number of these investigated event shape variables are shown here for comparison, with all selection criteria previous to the cut on this variable in question having been applied as seen in table 1. Note the cut-off point at 0.86 on the  $|\cos\theta_{TTB}|$  data values, a result of producing a reduced set of ntuples for quicker analysis with the production criterion that  $|\cos\theta_{TTB}| < 0.86$ .

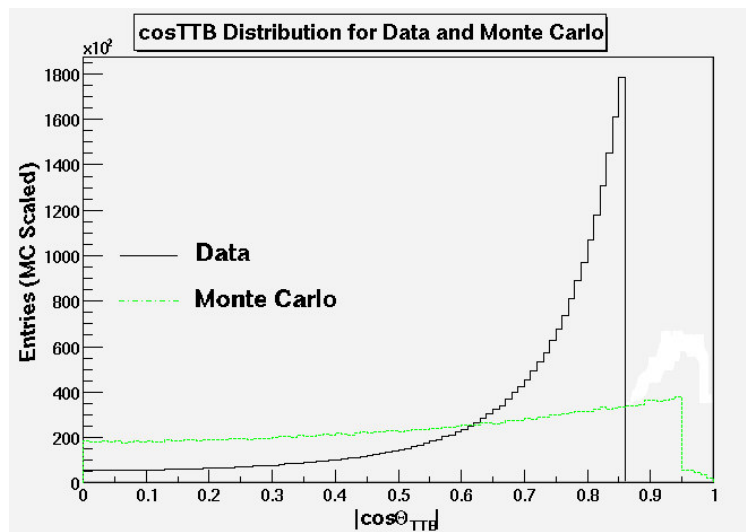


Figure 30:  $|\cos\theta_{TTB}|$  in signal Monte Carlo and data

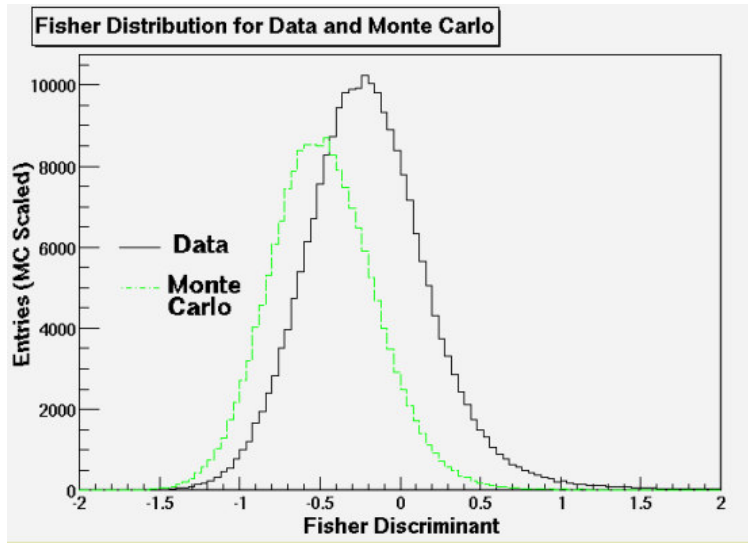


Figure 31: Fisher discriminant in signal Monte Carlo and data

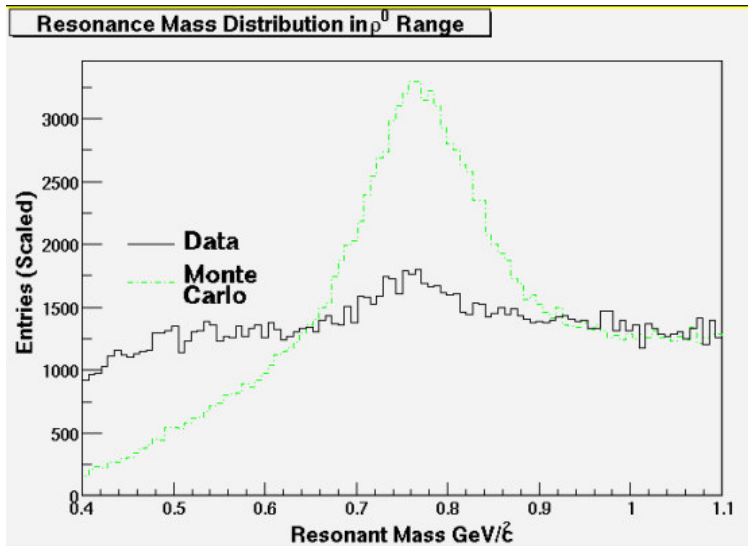


Figure 32: Mass of pion combination  $m_{\pi\pi}$  in signal Monte Carlo and data

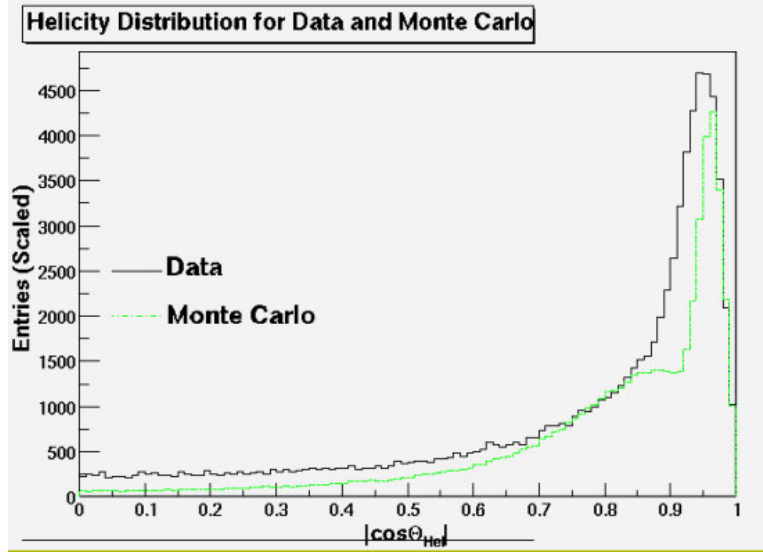


Figure 33: Helicity angle in signal Monte Carlo and data

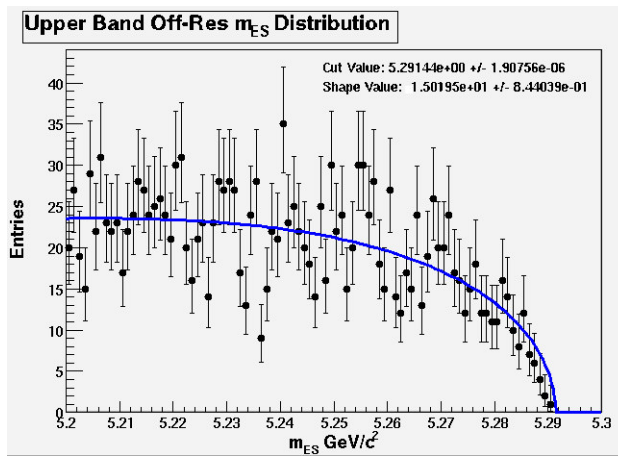
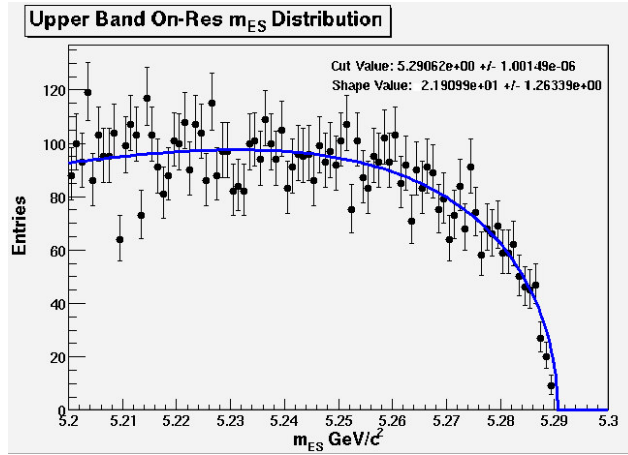
A first background characterization can be visualized in the two necessary fits for  $m_{ES}$  and  $\Delta E$ , whereby the Argus shape function is used to fit the  $\Delta E : m_{ES}$  plane upper and lower sidebands in  $m_{ES}$  and a first order polynomial is found sufficient to fit the  $\Delta E$  Grand Side Band. Section 4.7 explains in detail the product ratio calculation for estimating the level of background within the signal region. Here, the  $m_{ES}$  ratio fits for the upper sideband give

$$\frac{\int_{SR_{leftmost}}^{SR_{rightmost}} Ax_{Mes} \sqrt{1-x_{Mes}^2} \exp[-\epsilon \sqrt{1-x_{Mes}^2}] dx_{Mes}}{\int_{GSB_{leftmost}}^{GSB_{rightmost}} Ax_{Mes} \sqrt{1-x_{Mes}^2} \exp[-\epsilon \sqrt{1-x_{Mes}^2}] dx_{Mes}} = 0.199 \pm 0.011$$

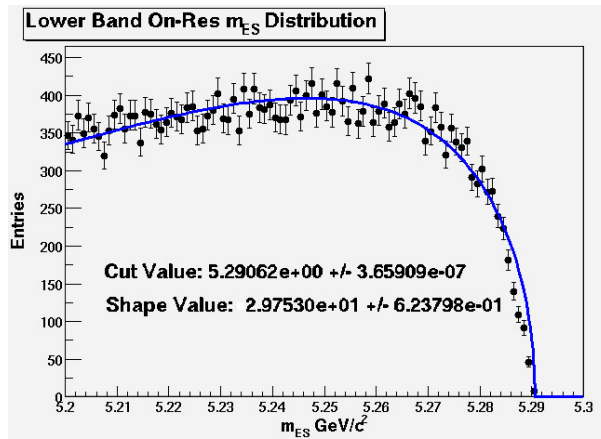
with an uncertainty given as one standard deviation from the fit, and it is this error on the shape parameter that dominates the uncertainty on the product ratio. The  $\Delta E$  fit information allows the ratio calculation

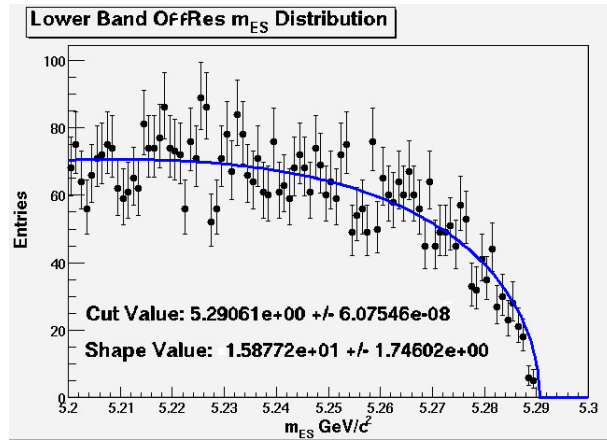
$$\frac{\int_{SR_{lowermost}}^{SR_{uppermost}} (ax_{\Delta E} + b) dx_{\Delta E}}{\int_{GSB_{lowermost}}^{GSB_{uppermost}} (ax_{\Delta E} + b) dx_{\Delta E}} = 0.223 \pm 0.002$$

which combines with the  $m_{ES}$  ratio fit to give the product ratio  $R = 0.044 \pm 0.003$ . We see the distributions in figures 34 to 41 for the upper, lower and combined sideband  $m_{ES}$  plots together with the  $\Delta E$  grand sideband plot fitted with their respective functions.

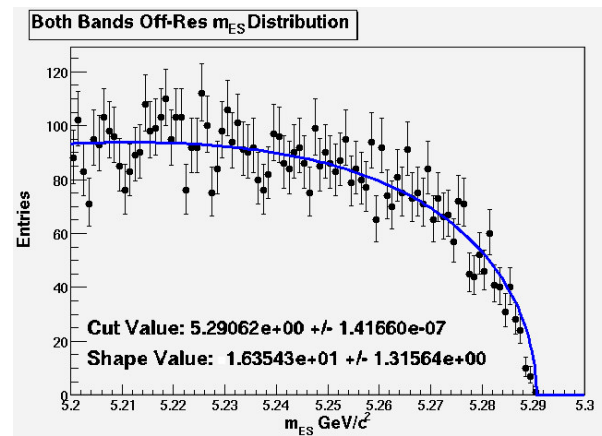
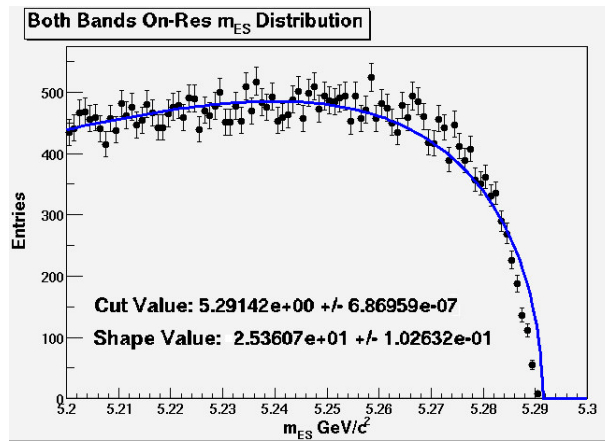


Figures 34 and 35:  $m_{ES}$  upper sideband with Argus shape for on-res and off-res data

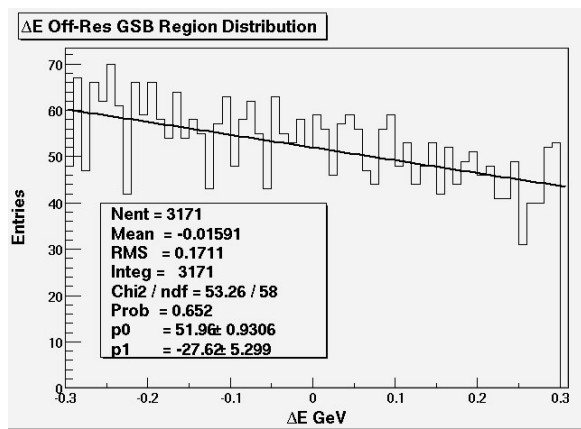
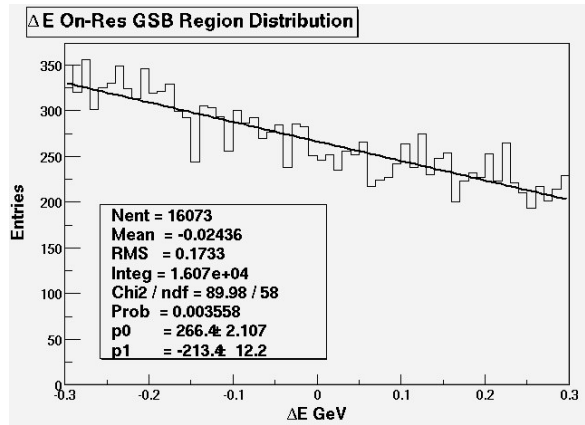




Figures 36 and 37:  $m_{ES}$  lower sideband with Argus shape for on-res and off-res data



Figures 38 and 39:  $m_{ES}$  combined upper and lower sidebands with Argus shape for on-res and off-res data



Figures 40 and 41:  $\Delta E$  distribution fitted with first order polynomial for on-res and off-res data

The Argus distributions for upper and lower bands invite an interesting comparison in that the distribution shapes are not broadly compatible even when taking the fit uncertainties into account. A dilemma is then whether to use the mismatched dual bands for determining an appropriate extrapolation fit to the signal region, or to use the upper band due to less likelihood of background contamination albeit with lower statistics. The best approximation to the expected background occurs with extrapolation from the upper band only, and as such this choice of Argus distribution for extrapolation will be carried on through the analysis.

## 5.2 Selection Optimization

Selection optimization involved extensive studies of a number of ntuple variables on which a selection criterion could have the possibility to aid separation of background and signal in an effective manner. Cuts were applied across a particular range of values per selected ntuple variable,

and then any correlation potentially affecting other likely optimization variables was checked by changing those ntuple variables in turn across a range of values while keeping the original selected variable fixed at a new optimal value. For example the Fisher discriminant is correlated with the  $|\cos(\Theta_{TTB})|$  value, and any change in one variable will require that the other variable is re-calculated to check the overall effect on sensitivity. This iterative process eventually reaches a point where the highest background to signal ratio in  $S/\sqrt{(S+B)}$  represents an approximate best estimation of sensitivity to mode-specific branching fraction events. Our optimization process entails the use of a branching fraction  $(8.6 \pm 2.0) \times 10^{-6}$  based on previous measurements [18] of  $B^+ \rightarrow \rho^0 \pi^+, \rho^0 \rightarrow \pi^+ \pi^-$  as an estimate in analysis. When we find a selection criteria to give a maximal  $S/\sqrt{(S+B)}$  sensitivity value then the branching fraction estimate should be in good agreement with that of the previous measurements. At this point it is possible to work from the selection values imparting this maximal sensitivity towards selection criteria that will give the best signal reconstruction efficiency.

Event variables investigated for the analysis:

- $|\cos(\Theta_{TTB})|$ , where  $\Theta_{TTB}$  is the angle between the thrust axes of the B candidate and the rest of the event. This variable is most effective for killing background, hence constitutes the initial cut.
- B vertex  $\chi^2$ .
- $\pi$  or  $K$  selector over a choice of four possible degrees on selection strictness.
- Fisher discriminant using the cornelius parameter optimization program.
- Resonance mass range for the  $\rho^0$ .
- $|\cos(\Theta_H)|$ , with  $\Theta_H$  the helicity angle.

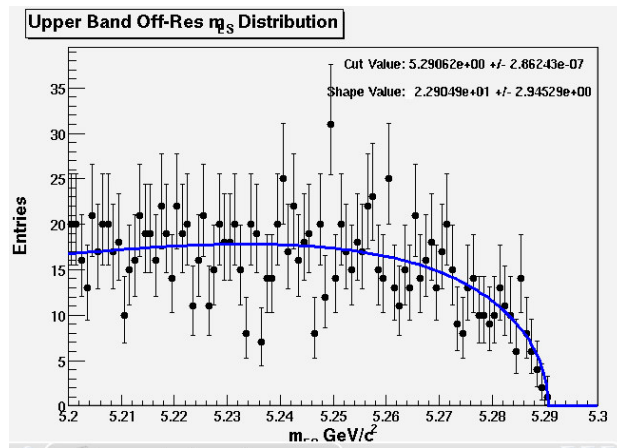
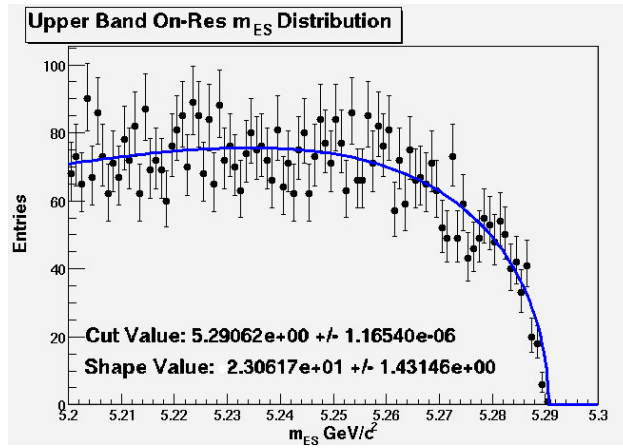
A table for efficiencies per successive cut is shown in table 2. The Fisher discriminant in particular can have a large impact on efficiency and it is possible to optimize further for a greater  $S/\sqrt{(S+B)}$  value. A danger preventing the application of this even tighter cut is that the optimization process at this point is harshly cutting on the number of signal events even though it is cutting on background to a larger extent. The Fisher data and Monte Carlo comparison shape plot in section 5.1 shows the Monte Carlo characteristics along with data, whereby we see the Monte Carlo signal events fall off beyond a particular point. A Fisher cut applied at low ranges would in

likelihood leave us with too few signal events to conduct a representative analysis, and the rapid variation in efficiency with low cut values on the shape parameter would cause fluctuations in efficiency that give an unreliable method of optimization.

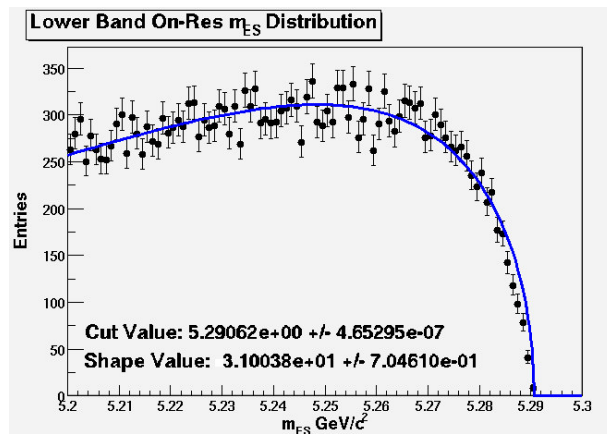
Cut variable	Signal MC	Combinatorial	On-res data	Off-res data
Reconstruction & preselection	1.807	0.989	0.021	0.223
$ \cos\theta_{thr}  < 0.59$	0.506	0.069	0.639	0.046
$\chi^2 < 25$	0.897	0.916	0.861	0.867
Has no tight Kaon	0.892	0.676	0.530	0.553
$E/p < 0.9$	0.959	0.937	0.870	0.882
FisherCrn < -0.1	0.879	0.601	0.635	0.594
$0.61 < mass_\rho < 0.93$	0.653	0.391	0.339	0.359
Helicity > 0.37	0.967	0.737	0.774	0.739
$\Delta E$ signal region	0.611	0.114	0.101	0.120
$m_{ES}$ signal region	0.538	0.012	0.016	0.015
Overall efficiency	0.209	$7.94 \times 10^{-5}$	$5.736 \times 10^{-5}$	$9.27 \times 10^{-6}$

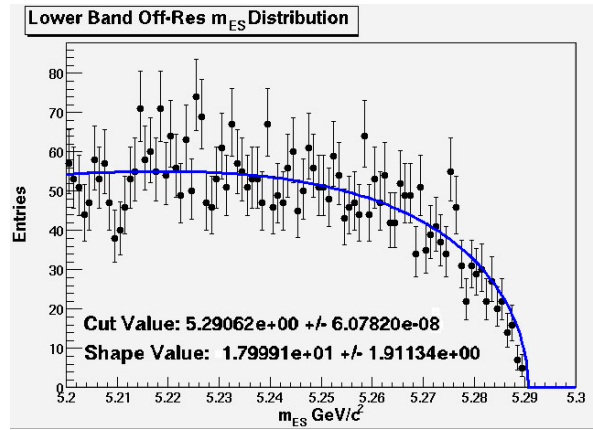
Table 2: Optimized selection criteria for  $B^+ \rightarrow \rho^0 \pi^+$ ,  $\rho^0 \rightarrow \pi^+ \pi^-$  detailing successive efficiencies

A recalculation of the R ratio of background characterization is necessary with these new optimized cut values. The new  $m_{ES}$  fit value was calculated at  $0.182 \pm 0.011$  and  $\Delta E$  fit value  $0.223 \pm 0.002$  with optimized cuts to give the product ratio  $0.041 \pm 0.003$ . Because there is an assumption of linear dependence and because both ranges are symmetrical about zero on the  $\Delta E$  range, the ratio is independent of the value of the fit parameters and thus carries no uncertainty from the fit. Here we can use off-resonance data again with the  $m_{ES}$  value shifted by +0.02, and fit the  $m_{ES}$  and  $\Delta E$  distributions to make a comparison check for background in the signal region since the blind analysis procedure forbids checking on-resonance data events in the signal region. The low amount of off-resonance data available does not have a sufficient number of events passing cuts to draw more than a general comparison agreement. Usage of light quark Monte Carlo is another means by which we can characterize the background. Although the Monte Carlo does not model the data perfectly it is useful as a comparison check.

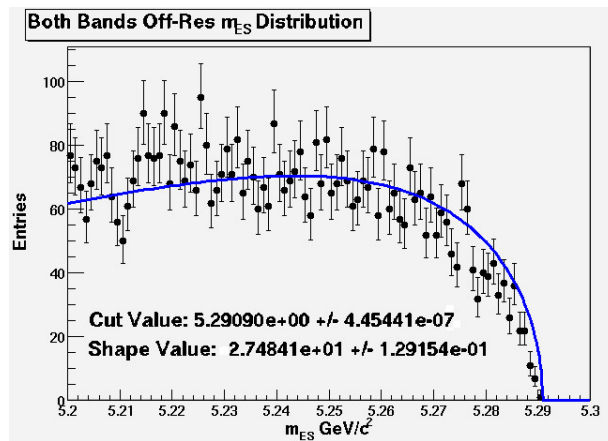
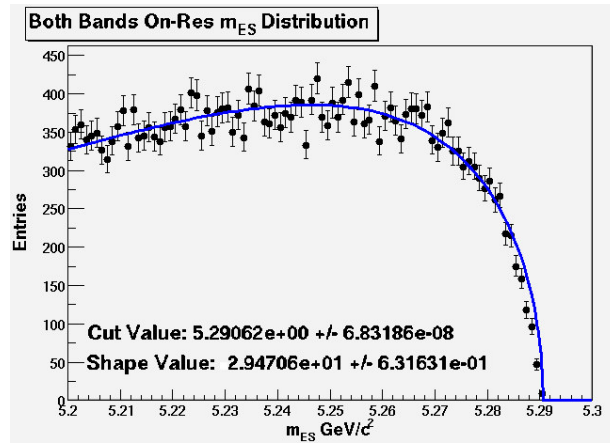


Figures 42 and 43:  $m_{ES}$  upper sideband with Argus shape for On- and Off- resonance data

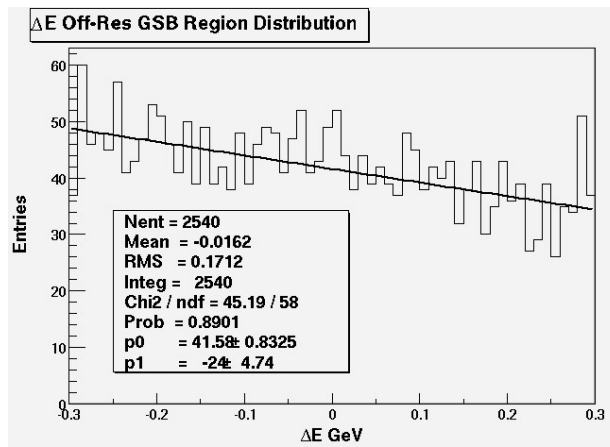
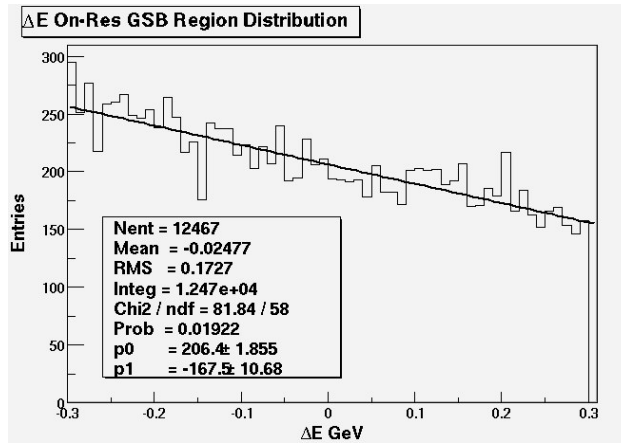




Figures 44 and 45:  $m_{ES}$  lower sideband with Argus shape for On- and Off- resonance data

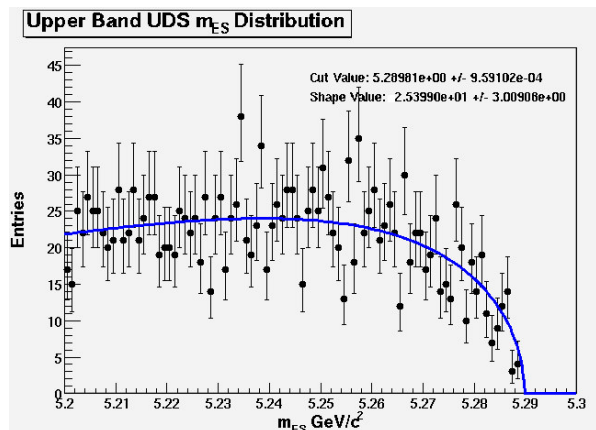


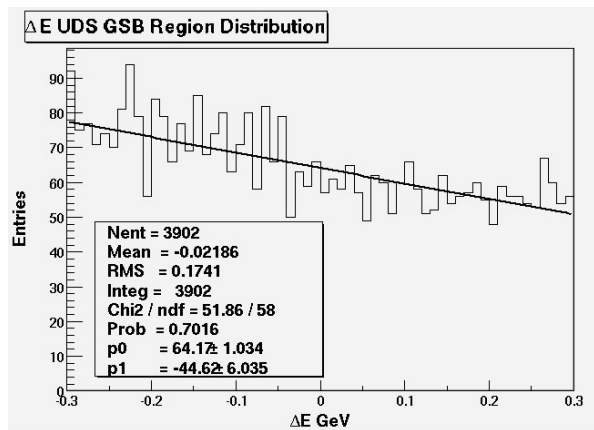
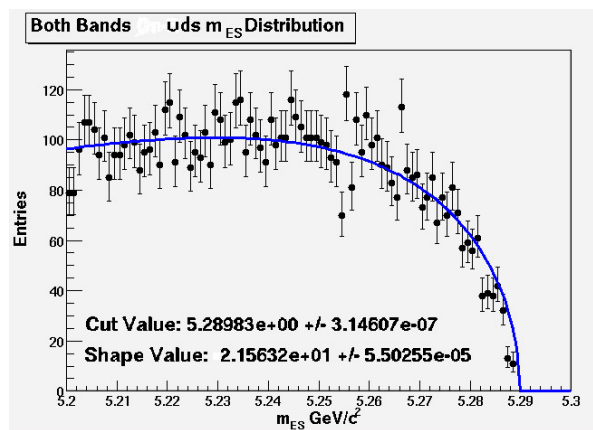
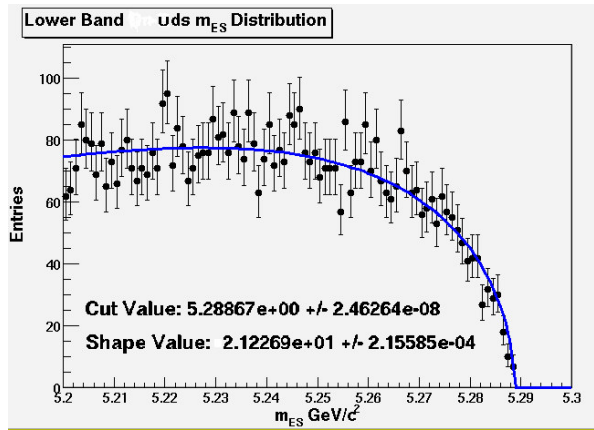
Figures 46 and 47:  $m_{ES}$  combined upper and lower sidebands with Argus shape for On- and Off- resonance data



Figures 48 and 49:  $\Delta E$  distribution fitted with first order polynomial for On- and Off- resonance data

The fit distortions resulting from the low amount of off-resonance data passing the optimized cut selection criteria may well not be an accurate comparison check to the on-resonance data. Hence a uds Monte Carlo sample underwent the same selection process, in turn leading to distributions as seen in the following plots:





Figures 50, 51, 52 and 53: The upper, lower and combined sideband distribution of  $m_{ES}$  in  $uds$  Monte Carlo, along with the GSB region  $\Delta E$   $uds$  distribution

## 5.3 Background Events

A number of Monte Carlo studies were undertaken to identify any significant sources of background from other  $B$  decay processes. Identified decays that appear as a significant factor to influence signal event counting can give cause to further considerations on selection criteria. A useful starting point for such an investigation is testing our selection criteria on generic charged  $B$  decays. MC truth particle identification variables are present within Monte Carlo ntuple structures and can give a specific particle match for each candidate. These particle ID records and other ntuple discriminants were used for investigating any candidate passing all selection cuts while lying within the  $\Delta E : m_{ES}$  plane signal region. Other generalized Monte Carlo employed for analysis include the  $B^0\bar{B}^0$  decays, light quark continuum  $e^+e^- \rightarrow u\bar{u}, d\bar{d}$  or  $s\bar{s}$  pair production, charm events  $e^+e^- \rightarrow c\bar{c}$  and rare charmless cocktail modes with two, three and four body final states. The neutral  $B$  ntuples allow us to check for potential background modes with characteristics similar to the  $B^+ \rightarrow \rho^0\pi^+, \rho^0 \rightarrow \pi^+\pi^-$ , for example decays involving neutral pions could conceivably pass selection criteria. The continuum Monte Carlo gives an indication of the continuum background we can expect in the signal region when using real data and should be in line with the estimates from the Argus and polynomial ratio fits in the  $\Delta E : m_{ES}$  plane sidebands. This continuum background is already accounted for from the sideband estimation. Charm events in Monte Carlo are used to determine whether charm decays pose any specific problems. Rare charmless cocktail modes can pinpoint problem contamination channels, though the wide mixture of decays producing finite numbers of signal events shows that even sophisticated selection criteria lets in rogue events. In such cases the only recourse may be to simply subtract a scaled number of events from the signal region before unblinding on data, although this approach assumes that the Monte Carlo branching fractions in question are accurate. Monte Carlo datasets enable us to make an accurate assessment for the impact of cut selections on on-resonance data, though these datasets must be scaled in size such that the number of generated events of interest correspond to those expected in the on-resonance dataset. The number of signal region events are counted from a Monte Carlo sample size of events produced, allowing a determination of the ratio of signal region events to produced events. This ratio factor is then used to indicate the integer number of signal region events found. In

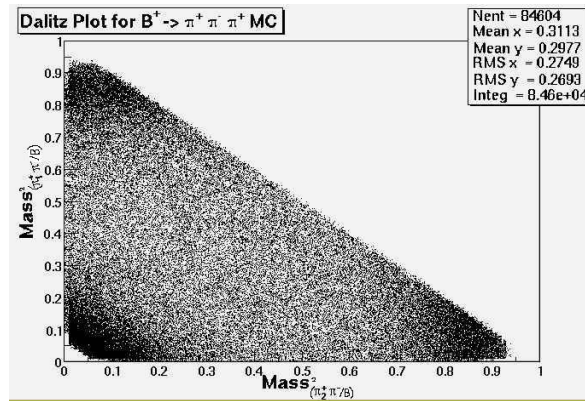
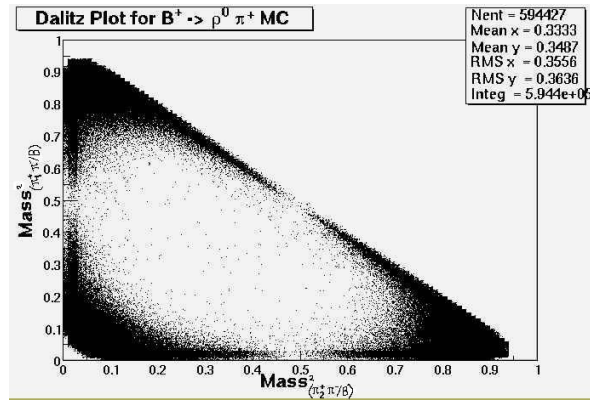
the case of the non-mode-specific dataset samples the Monte Carlo sample size is scaled to the size of the on-resonance dataset. For the case of each mode-specific channel cross checks, the number of produced events is scaled to the number of mode-specific events expected from the branching ratio when using the number of on-resonance dataset events. A table showing the results of contaminant checks for a number of generalized and mode specific Monte Carlo samples can be seen below in table 3:

	Events Produced	Events in Signal Region	Scaled Events
$B^+B^-$ generic	$3.957 \times 10^7$	583	259
$B^0\bar{B}^0$ generic	$3.433 \times 10^7$	122	47
$e^+e^- \rightarrow u\bar{u}, d\bar{d}$ or $s\bar{s}$	$2.388 \times 10^6$	6	234
$e^+e^- \rightarrow c\bar{c}$	954000	0	29
Cocktail of Rare Events	$1.2 \times 10^6$	1	92
$D^0\pi^-, D^0 \rightarrow K^-\pi^+$ Specific Mode	231000	446	32
$D^0\pi^-, D^0 \rightarrow \pi^-\pi^+$ Specific Mode	67000	1547	15
$B^\pm \rightarrow \pi^\pm\pi^\mp\pi^\pm$ Specific Mode	65000	844	30 (at 90% CL)

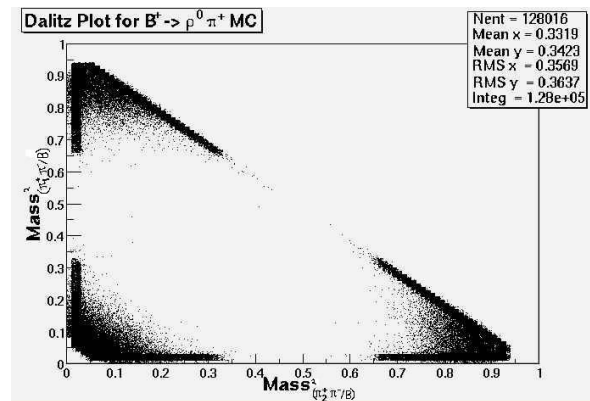
Table 3: Contaminant check with general and mode specific Monte Carlo scaled to data set size

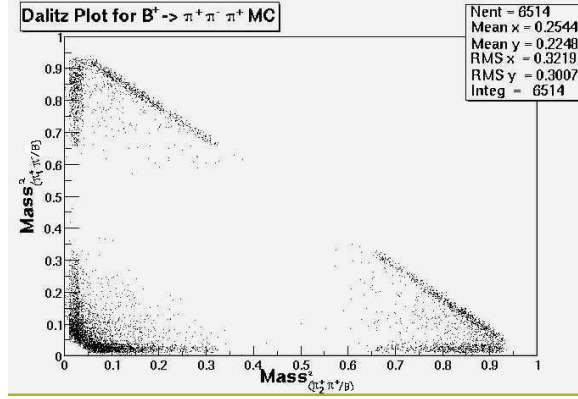
Further study into the contaminants of the general MC sets provided an indication of particular decay modes liable to contain candidates seen as erroneously belonging to the  $B^+ \rightarrow \rho^0\pi^+, \rho^0 \rightarrow \pi^+\pi^-$  mode of primary interest. In the case of three pion contaminant information several possible modes could in theory be responsible for cross channel contamination, and as such a number of mode specific MC data files were produced in order to identify the decay processes of these background events.

Monte Carlo results with the truth tags suggest the  $B^- \rightarrow D^0\pi^-, D^0 \rightarrow K^-\pi^+$  or  $\pi^+\pi^-$  decays are a background contribution in the main mode studies, and as such a decision was taken to veto the invariant mass combination of  $K^-\pi^+$  or  $\pi^+\pi^-$  corresponding to the  $D^0$  resonant range of 1.845 to 1.885 GeV/c<sup>2</sup>. The narrowness of this resonance cut should produce little signal candidate loss. Another potential source of background in our analysis appears in the form of  $B^\pm \rightarrow \pi^\pm\pi^\mp\pi^\pm$ , and for this mode the Dalitz plot comparisons in figures 54 to 57 show the overlapping distribution of  $B^\pm \rightarrow \pi^\pm\pi^\mp\pi^\pm$  into  $B^+ \rightarrow \rho^0\pi^+, \rho^0 \rightarrow \pi^+\pi^-$  signal region by virtue of its uniform distribution over the whole Dalitz plot.



Figures 54 and 55: Dalitz plots for  $B^+ \rightarrow \rho^0 \pi^+$ ,  $\rho^0 \rightarrow \pi^+ \pi^-$  and  $B^\pm \rightarrow \pi^\pm \pi^\mp \pi^\pm$  Monte Carlo prior to cuts





Figures 56 and 57: Dalitz plots for  $B^+ \rightarrow \rho^0 \pi^+$ ,  $\rho^0 \rightarrow \pi^+ \pi^-$  and  $B^\pm \rightarrow \pi^\pm \pi^\mp \pi^\pm$  Monte Carlo after applying cuts

While a number of selection criteria were considered, the conclusion is that the clearest way to neutralize the  $B^\pm \rightarrow \pi^\pm \pi^\mp \pi^\pm$  effect on signal region events is simply to subtract the expected number of  $B^\pm \rightarrow \pi^\pm \pi^\mp \pi^\pm$  decays from the final event counting. It is important to note the difficulty of measuring a  $B^\pm \rightarrow \pi^\pm \pi^\mp \pi^\pm$  branching fraction (due to uncertainties in confirming a direct three pion decay) means we must resort to using a PDG quoted 90% confidence upper limit of  $< 1.3 \times 10^{-4}$  branching estimate for  $B^\pm \rightarrow \pi^\pm \pi^\mp \pi^\pm$ . The uniformity of the  $B^\pm \rightarrow \pi^\pm \pi^\mp \pi^\pm$  distribution becomes useful in that it should be possible to accurately extrapolate any  $B^\pm \rightarrow \pi^\pm \pi^\mp \pi^\pm$  decays studied in a low density region of the Dalitz plot into an ratio expectation value within the  $B^+ \rightarrow \rho^0 \pi^+$ ,  $\rho^0 \rightarrow \pi^+ \pi^-$  signal region.

Other identified contaminants included the decays of  $B^+ \rightarrow \rho^0 K^+$ ,  $\rho^0 \rightarrow \pi^+ \pi^-$  and  $B^+ \rightarrow \rho^0 \rho^+$ ,  $\rho^0 \rightarrow \pi^+ \pi^-$ ,  $\rho^+ \rightarrow \pi^+ \pi^0$  and  $B^+ \rightarrow K^{*0} \pi^+$ ,  $K^{*0} \rightarrow K^+ \pi^-$ . In checking contaminants the combination of low branching fraction and little likelihood of kaon misidentification suggests the contribution of these modes to our signal region should be negligible.

## 5.4 Efficiency corrections

Small yet necessary corrections to the Monte Carlo signal efficiency arising from use of a number of the selection criteria are applied, and the errors involved provide an overall systematic uncertainty for the efficiency of selections. Tracking corrections are taken from the BaBar Tracking Efficiency Working Group recommendations [22], whereby the overall efficiency correction tables

for tracking are the correction per event (i.e. product of all  $B$  candidate track corrections) averaged for all Monte Carlo events passing analysis selection criteria. Here the tracking correction is found to be 0.975, with an 0.8% systematic error for each GoodTracksLoose track giving a total systematic error of 2.4% . We use the Particle ID corrections from the BaBar Particle Identification Action Working Group [30] for the Monte Carlo to more accurately reflect the data efficiency of particle selectors. The efficiency of the Kaon selector for kaons and pions is measured over a range of momentum bins and polar angles [24] that correspond to inside or outside the drift chamber acceptance, and efficiency tables are produced. Each mode will have different kaon or pion momenta and polar angles, resulting in different particle ID efficiencies. So in each case signal Monte Carlo is used to determine these differing efficiencies, and particle ID efficiency is the ratio of number of events in the signal region with and without particle ID cuts with all usual cuts for that mode analysis being applied in both cases. The efficiency correction for our analysis comes from the ratio between particle ID efficiency in data and particle ID efficiency in Monte Carlo. Results for the systematic uncertainty from PID corrections is 5% on the signal Monte Carlo efficiency, and statistical errors in the data are considered systematic errors in the efficiency corrections.

The method for assessing corrections using  $B^- \rightarrow D^0\pi^-, D^0 \rightarrow K^-\pi^+$  data is discussed at length in the following section; we will simply quote the calibration results here:  $\Delta E$  mean has a shift of -6.683 MeV with sigma a scale factor of 1.034, while the  $m_{ES}$  distribution has no significant shift and a sigma scaling factor of 1.117. Application of these  $\Delta E$  and  $m_{ES}$  corrections onto the signal Monte Carlo uses these new variations in mean and sigma sizes on functions fitted to the signal mode. Table 4 below shows the calibration channel Monte Carlo and data comparisons:

Fitted Parameter	$D^0\pi$ Data	$D^0\pi$ Monte Carlo
$\Delta E$ Mean (MeV)	$-8.143 \pm 0.857$	$-1.460 \pm 0.187$
$\Delta E$ Width (MeV)	$19.63 \pm 1.50$	$18.98 \pm 0.285$
$m_{ES}$ Mean ( $\text{GeV}/c^2$ )	$5.28 \pm 9.929 \times 10^{-5}$	$5.28 \pm 8.210 \times 10^{-5}$
$m_{ES}$ Width ( $\text{MeV}/c^2$ )	$2.441 \pm 0.188$	$2.186 \pm 0.083$

*Table 4: Resolutions and means of fits with the resultant shift and scaling factors*

If we let  $F(x, \sigma)$  be a double Gaussian distribution function for either uncorrected  $\Delta E$  or  $m_{ES}$

and  $G(x)$  the distribution function with the calibration shift added and scale factors, the efficiency correction over the signal box limits  $a$  and  $b$  is given by

$$\Delta E_{correction} = \frac{\int_a^b G(x, \sigma) dx}{\int_a^b F(x, \sigma) dx}$$

Errors found in the calibration check for  $\Delta E$  and  $m_{ES}$  have the Monte Carlo and data sections added in quadrature for the total mean and sigma errors in  $\Delta E$ ,

$$\pm \Delta E_{mean\ error} = \sqrt{(\Delta E_{error})_{MC}^2 + (\Delta E_{error})_{Data}^2}$$

$$\pm \Delta E_{sigma\ error} = \sqrt{(\sigma_{error})_{MC}^2 + (\sigma_{error})_{Data}^2}$$

and similarly for the  $m_{ES}$  kinematic variable. These upper and lower limits are applied separately to the original function  $F(x, \sigma)$  to give the efficiency correction total error for  $\Delta E$  mean and sigma

$$\pm Total_{mean\ error} = \left| \int_a^b F(x, \sigma) dx - \int_a^b F(x \pm \delta x, \sigma) dx \right|$$

$$\pm Total_{sigma\ error} = \left| \int_a^b F(x, \sigma) dx - \int_a^b F(x, \sigma \pm \delta \sigma) dx \right|$$

with same sign mean and sigma errors added in quadrature to give final upper and lower error boundaries for the efficiency correction.

A final set of efficiency corrections to be applied to our signal mode analysis efficiency is given in table 5. The asymmetry in correctional factors is a consequence of applying the upper and lower limits separately and then adding the systematic errors in quadrature to limits of different magnitudes.

Selector	Correction
Tracking	$0.975 \pm 0.023$
PID	$1.000 \pm 0.050$
$\Delta E$	$0.991 \pm 0.004$
$m_{ES}$	$0.976 \begin{smallmatrix} +0.007 \\ -0.014 \end{smallmatrix}$
Total	$0.943 \begin{smallmatrix} +0.056 \\ -0.057 \end{smallmatrix}$

*Table 5: Resultant corrections applied to overall Monte Carlo calibrated efficiency*

## 5.5 Calibration Checking

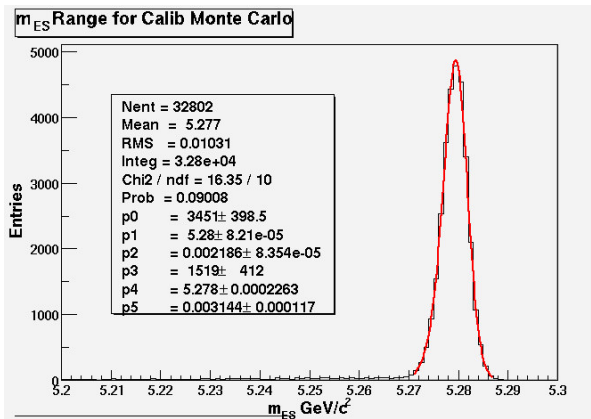
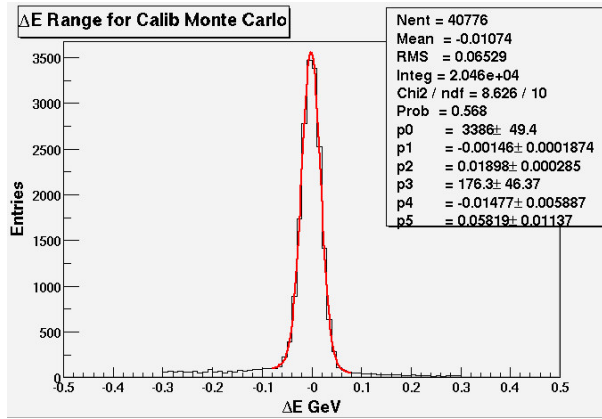
The channel  $B^- \rightarrow D^0\pi^-, D^0 \rightarrow K^-\pi^+$  was used as a calibration mode for  $B^+ \rightarrow \rho^0\pi^+, \rho^0 \rightarrow \pi^+\pi^-$  given the similarity of decay variables with comparable kinematics. Selecting these calibration channel decays and their charge conjugate provide the opportunity for important comparisons between the Monte Carlo and reconstructed data, in turn allowing us a careful correction of errors and efficiencies for the main analysis. The PDG [18] lists the branching fraction for the decay  $B^- \rightarrow D^0\pi^-$  as  $(4.98 \pm 0.29) \times 10^{-3}$  and  $D^0 \rightarrow K^-\pi^+$  as  $(3.8 \pm 0.09)\%$ , making a combined branching fraction for the channel  $B^- \rightarrow D^0\pi^-, D^0 \rightarrow K^-\pi^+$  given by  $(1.89 \pm 0.16) \times 10^{-4}$ . The higher branching fraction reduces statistical errors. Cuts applied during calibration are similar to those used in the determination of the actual decay channel of interest, the exception being the particle identification and selection variables chosen directly to distinguish the calibration channel events. The resonance mass selector cuts were changed in both their combined difference and average value. The isotropic decay of the  $D^0$  particle means the helicity cut would not indiscriminate signal from background, and so there is no helicity selector. Otherwise keeping the calibration analysis as close as possible to the desired channel analysis technique should provide the best cross-check possible.

A mode-specific Monte Carlo sample for the calibration decay mode contained 231,000 signal events and was prepared with the 12.5.2b release. Scatter plots of the  $\Delta E$  versus  $m_{ES}$  variables in both data and Monte Carlo are shown below. The figures 58 to 63 below show the  $\Delta E$  and  $m_{ES}$  distributions for the decay channel, and table 6 summarizes the cumulative succession of cuts applied. Column one gives Monte Carlo efficiency results without applying the truth B event tag in order to remain comparable to the main analysis. The second column provides an assessment of the combinatorial background. Our processed on-resonance dataset corresponds to 88.9 million  $B\bar{B}$  events as before, and similarly the off-resonance dataset size is 10.46 million events. Efficiencies of these data samples are represented in the third and fourth column of the table.

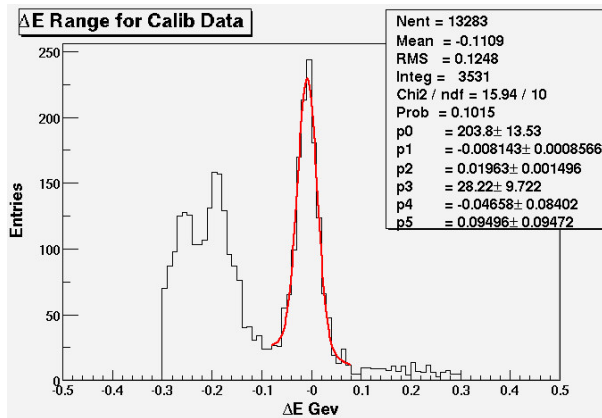
Cut variable	Signal MC	UDS Combinatorial	On-res data	Off-res data
Reconstruction & preselection	0.911	0.989	0.021	0.977
$\cos \theta_{TTB} < 0.59$	0.581	0.068	0.620	0.046
Has one tight Kaon	0.809	0.255	0.365	0.338
$E/p < 0.9$	0.957	0.935	0.869	0.889
$fisherCrn < -0.1$	0.686	0.632	0.680	0.608
$1.84 < D^0 \text{ mass} < 1.89$	0.948	0.086	0.178	0.126
$ \Delta E  < 0.06696$	0.969	0.801	0.064	0.067
$5.27017 < m_{ES} < 5.28783$	0.995	0.969	0.069	0.090
Overall efficiency	0.257	$6.764 \times 10^{-4}$	$2.207 \times 10^{-6}$	$6.238 \times 10^{-6}$

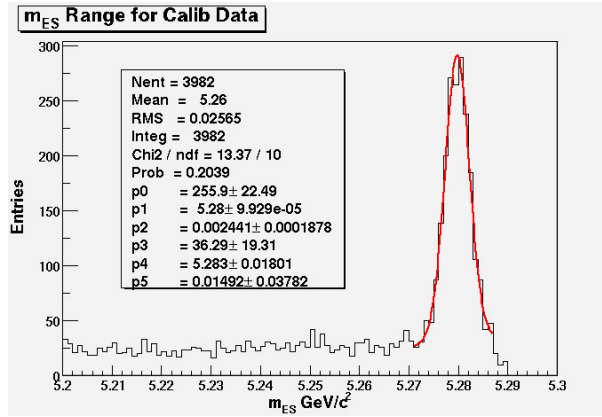
Table 6: Optimized selection criteria for  $B^- \rightarrow D^0 \pi^-, D^0 \rightarrow K^- \pi^+$  detailing successive efficiencies

A sum of two Gaussians was fitted to the  $\Delta E$  distribution of Monte Carlo showing the resultant narrower Gaussian to have a resolution of 18.98 MeV with uncertainty of 0.29 MeV. On-resonance data was also fitted with a double Gaussian, and this resolution of  $19.63 \pm 1.50$  MeV compares closely to that for the Monte Carlo generated distribution. Following earlier conventions in this calibration analysis the  $\Delta E$  range for the signal region box is taken as three times the  $B^+ \rightarrow \rho^0 \pi^+, \rho^0 \rightarrow \pi^+ \pi^-$  resolution. Another double Gaussian is used for the fit of the Monte Carlo  $m_{ES}$  distribution to give  $2.18 \pm 0.08$  MeV. The Monte Carlo and on-resonance data at  $2.44 \pm 0.18$  MeV for  $m_{ES}$  agree well. The  $m_{ES}$  signal region range is consistent with the convention of three times the resolution found for  $B^+ \rightarrow \rho^0 \pi^+, \rho^0 \rightarrow \pi^+ \pi^-$ . We see from the  $\Delta E$  vs.  $m_{ES}$  scatter plot for MC that almost all the signal lies within the signal region while some contaminants reside in the lower sideband of on-resonance data; the effect of these contaminants can clearly be seen in the on-resonance data sidebands shown below. The effect of these contaminants is to restrict results in background characterization to those from the upper sideband only; furthermore due to the leakage of this high level of background the size of the GSB region is reduced to  $5.22 < m_{ES} < 5.25$  and  $|\Delta E| < 0.15$ .

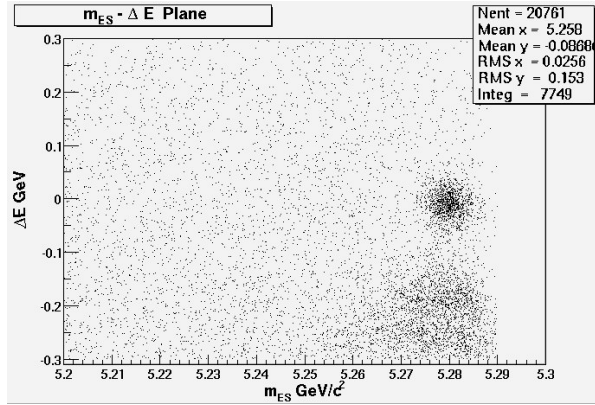
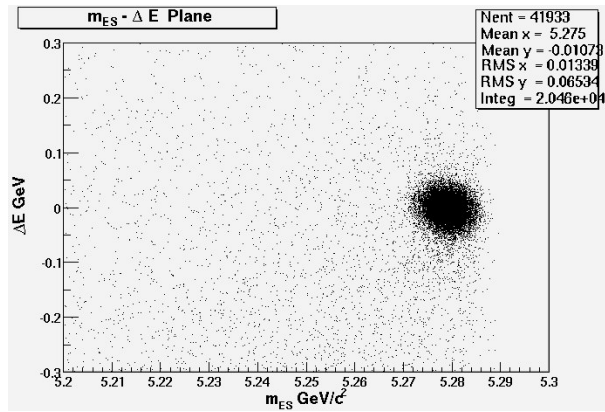


Figures 58 and 59:  $\Delta E$  and  $m_{ES}$  distributions for the  $B^- \rightarrow D^0 \pi^-$ ,  $D^0 \rightarrow K^- \pi^+$  Monte Carlo





Figures 60 and 61:  $\Delta E$  and  $m_{ES}$  distributions for the  $B^- \rightarrow D^0 \pi^-$ ,  $D^0 \rightarrow K^- \pi^+$  on-resonance data



Figures 62 and 63:  $\Delta E$  vs.  $m_{ES}$  distribution plots for Monte Carlo and on-resonance data

We calculate the corrections to the  $B^+ \rightarrow \rho^0 \pi^+$ ,  $\rho^0 \rightarrow \pi^+ \pi^-$  channel Monte Carlo selection using the results of the calibration channel as described in section 5.4. Using the  $B^+ \rightarrow \rho^0 \pi^+$ ,  $\rho^0 \rightarrow \pi^+ \pi^-$  channel range definition of the signal region the number of events observed within this region,  $N_{sig}$ , was 2108. An estimation of the number of background requires an extrapolation of the number  $N_{GSB}$  found in the grand sideband area. As described more fully in

the previous chapter, such an extrapolation uses the calculation of the product ratio for both the Gaussian fitted  $\Delta E$  and Argus function fitted  $m_{ES}$  fits for scaling into the signal region. This R value was found to be  $0.0453 \pm 0.005$  where the uncertainty is due to the one standard deviation error from the Argus fit. 2787 candidates observed in the GSB region give 126 background in the signal region. Using the formula

$$B^- \rightarrow D^0\pi^-, D^0 \rightarrow K^-\pi^+ \text{ Branching Fraction} = \frac{N_{sig}}{\epsilon_{MC}N_{\bar{B}\bar{B}}}$$

we estimate the branching fraction to be  $(1.960 \pm 0.043 \pm 0.210) \times 10^{-4}$ , where the first error is statistical and the second error is systematic uncertainty in the extrapolation of background events to the signal region box. Efficiency correction factors are taken to be the same as for the main analysis mode. The calibration value is in good agreement with the PDG branching fraction given as  $(1.89 \pm 0.16) \times 10^{-4}$  for this decay channel.

The  $B^- \rightarrow D^0\pi^-, D^0 \rightarrow \pi^-\pi^+$  channel was also investigated as a calibration channel due to the similarity of reconstruction to  $B^+ \rightarrow \rho^0\pi^+, \rho^0 \rightarrow \pi^+\pi^-$ , although the  $(7.58 \times 10^{-6})$  branching fraction of this calibration channel is of the same order of magnitude as that of our main channel of investigation. Despite this effect on statistics, the channel was analyzed with a result of  $(7.41 \pm 0.22) \times 10^{-6}$  that matched the  $(7.58) \times 10^{-6}$  PDG value well.

GSB Events	2787
Ratio R	0.0453
Background in SR	126
MC Efficiency (corrected)	0.242
SR Events Counted	2108
Expected Events in SR	2159
Branching Fraction	$1.960 \times 10^{-4}$

Table 7: Summary of Analysis for  $B^- \rightarrow D^0\pi^-, D^0 \rightarrow K^-\pi^+$

## 5.6 $B^+ \rightarrow \rho^0\pi^+, \rho^0 \rightarrow \pi^+\pi^-$ Branching Fraction

Our optimized selection criteria gives 24912 events in the Grand Sideband. The extrapolation ratio  $A = 0.041 \pm 0.003$  then allows us to predict the amount of background in the signal region

using the product of GSB Events and background ratio fit to give the background events expected in the signal region area at  $1011 \pm 6.5$  (statistical)  $\pm 74.0$  (systematic) events. Statistical errors are determined with the root square value of the number of data entries, and a total systematic error found by adding in quadrature the fractional errors for the calibration selectors (see section 5.4) with the extrapolation ratio and dataset entries uncertainties. The number of charged  $B$  mesons in the on-resonance data set is  $(88.9 \pm 0.2) \times 10^6$ . The  $B^+ \rightarrow \rho^0 \pi^+, \rho^0 \rightarrow \pi^+ \pi^-$  branching fraction is  $(8.6 \pm 2.0) \times 10^{-6}$ , and a Monte Carlo efficiency of  $0.197^{+0.010}_{-0.013}$  takes into account the correction factor  $0.943^{+0.056}_{-0.057}$  (described in section 5.4) applied to the optimised signal Monte Carlo efficiency of 0.207 in table 2. Using the equation

$$B^+ \rightarrow \rho^0 \pi^+, \rho^0 \rightarrow \pi^+ \pi^- \text{ Branching Fraction} = \frac{N_{sig}}{\epsilon_{MC} N_{B\bar{B}}}$$

gives  $150.6 \pm 35.0$  (total uncertainty) expected signal events  $N_{sig}$  in the signal region. The analysis method previously described with optimal cut selection gives the number of events counted in the signal region as  $1190 \pm 34.5$  (statistical) after unblinding. Subtracting the expected number of background events from the unblinded total of events counted gives  $179.0 \pm 35.1$  (statistical)  $\pm 74.0$  (systematic) events. This value is the new  $N_{sig}$  signal events in the signal region, and then fed back into the branching fraction equation to produce a new branching fraction measurement of  $(10.22 \pm 2.00 \pm 4.22) \times 10^{-6}$  for the  $B^+ \rightarrow \rho^0 \pi^+, \rho^0 \rightarrow \pi^+ \pi^-$  charmless hadronic decay. The number of signal region events estimated as  $B \rightarrow \pi^+ \pi^- \pi^+$  decay events can be expected to have a maximal 30 contamination events following on from an assessment using the PDG quoted  $B \rightarrow \pi^+ \pi^- \pi^+$  branching fraction of  $< 1.3 \times 10^{-4}$  upper limit.

GSB Events	24912
Ratio of Background in Signal Region from GSB Extrapolation Fit	$0.041 \pm 0.003$
Expected Background in Signal Region	$1011 \pm 6.5 \pm 74.0$
Signal MC Efficiency	$0.197^{+0.010}_{-0.013}$
Events in Signal Region Counted after Unblinding	$1190 \pm 34.5$
Expected $B^+ \rightarrow \rho^0 \pi^+, \rho^0 \rightarrow \pi^+ \pi^-$ Events in Signal Region	$150.6 \pm 35.0$
Background Subtracted Events in Signal Region	$179.0 \pm 35.1 \pm 74.0$
Branching Fraction	$(10.22 \pm 2.00 \pm 4.22) \times 10^{-6}$

Table 8: Summary of Analysis for  $B^+ \rightarrow \rho^0 \pi^+, \rho^0 \rightarrow \pi^+ \pi^-$

We see that the measured value agrees well with the PDG branching fraction value for this

decay channel even when allowing for the maximal contribution of 30 background subtracted events being  $B \rightarrow \pi^+\pi^-\pi^+$  decay events. The unresolved difficulties of reliably vetoing  $B \rightarrow \pi^+\pi^-\pi^+$  decay contamination from a cut and count analysis into the  $B^+ \rightarrow \rho^0\pi^+, \rho^0 \rightarrow \pi^+\pi^-$  decay means that the measurement value in table 8 is an upper limit on the branching fraction. The unblinded  $\Delta E - m_{ES}$  plane distribution of events is shown in figure 64. It is possible to see an increased distribution density in the signal region, and also the contaminant along the area of the lower sideband region.

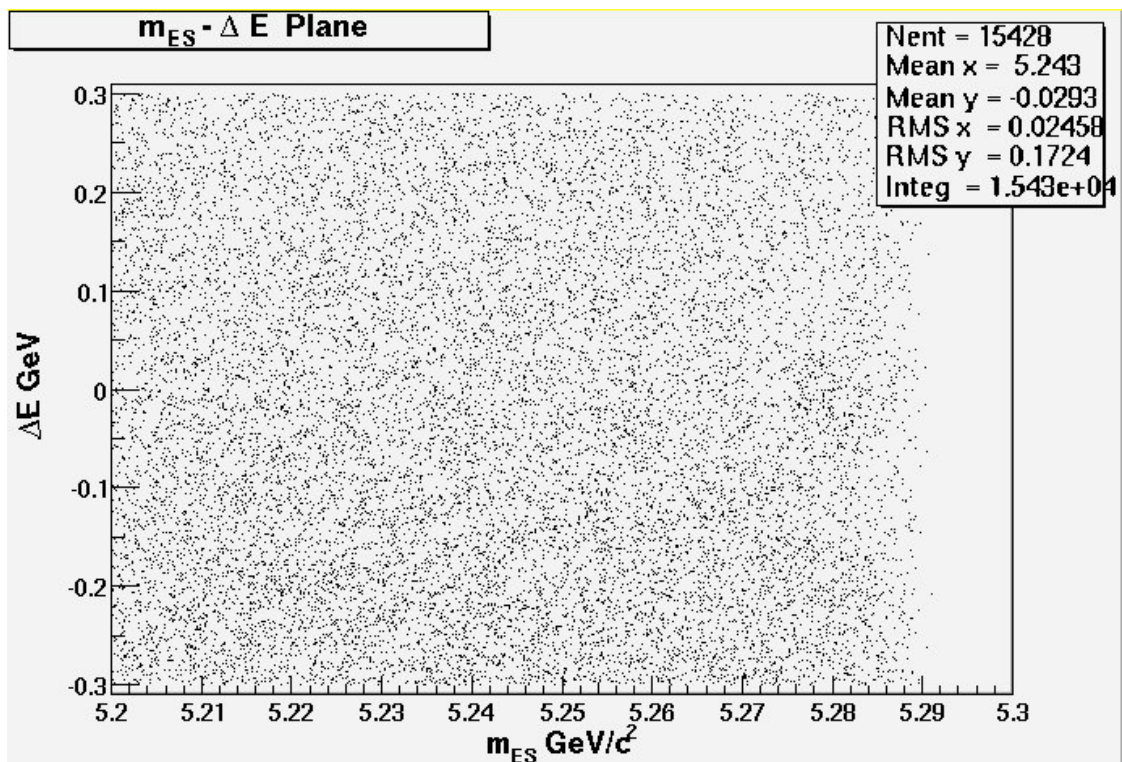


Figure 64:  $\Delta E$  vs.  $m_{ES}$  distribution plot for unblinded on-resonance data

## 5.7 Charge Asymmetry Measurement

Charge asymmetry was investigated alongside the main analysis of a branching fraction measurement for the  $B^+ \rightarrow \rho^0\pi^+, \rho^0 \rightarrow \pi^+\pi^-$  decay. Signal region events following optimised selection, in parallel to the analysis of section 5.6, are counted as 613 (51.51%) decaying from a  $B^+$  meson and 577 (48.49%) from a  $B^-$  meson. In the GSB region the number of these charged decays increases to 12718 (51.05%) decaying from a  $B^+$  meson and 12194 (48.95%) from a  $B^-$  meson.

We calculate background charge asymmetry in the signal region by scaling in the asymmetric charges found in the grand sideband and then subtracting from the counted signal region asymmetric charges. Our extrapolation of charge asymmetry from the GSB region to background in the signal region yields  $1190 \pm 34.5$  charged signal region events, of which the continuum background is estimated to account for  $516 \pm 4.6$  (statistical)  $\pm 37.8$  (systematic) positive charge events and  $495 \pm 4.5 \pm 36.2$  negative charge events. The subtraction leaves  $97 \pm 34.8 \pm 37.8$  positive charge signal events and  $82 \pm 34.8 \pm 36.2$  negative charge signal events in the signal region. Thus the asymmetry for the  $B^+ \rightarrow \rho^0 \pi^+, \rho^0 \rightarrow \pi^+ \pi^-$  decay channel can be calculated using the equations

$$A_{SR} = \frac{A_{+ve} - A_{-ve}}{A_{+ve} + A_{-ve}} \text{ signal events in the signal region}$$

$$A_{BG} = \frac{A_{+ve} - A_{-ve}}{A_{+ve} + A_{-ve}} \text{ background in the signal region,}$$

whereby we find that  $A_{SR} = 0.084 \pm 0.389$  (statistical)  $^{+0.044}_{-0.018}$  (systematic) and  $A_{BG} = 0.021 \pm 0.009$  (statistical) with negligible systematic uncertainty. The statistical errors are uncorrelated between positive and negative events. The systematic error on the background subtraction is due to the background ratio fit uncertainty, and the fact that this systematic is completely correlated between positive and negative events means the systematics on the background subtraction are common between positive and negative samples, and so almost cancel in the numerators but not in the denominators. Most systematics such as particle ID and tracking efficiency will cancel in asymmetry calculations although the 2% tracking charge asymmetry described in section 4.4 is a systematic on the overall charge asymmetry and added in quadrature. Nevertheless the size of statistical errors for the low statistics precludes the possibility of declaring determinable results for charge asymmetry measurements in the  $B^+ \rightarrow \rho^0 \pi^+, \rho^0 \rightarrow \pi^+ \pi^-$  decay channel.

## 5.8 Conclusions

Chapter one of this thesis introduced the historical idea of separate particles constituting everyday matter, and the later experimental verifications of this idea prompting scientists to attempt a consistent theory of the properties and interactions of particles. The next chapter discussed

symmetry transformations, and how a force interaction acts on the mixing matrix of the fundamental quarks can give rise to asymmetric transformations. This asymmetry is CP violation, with effects that can be observed in differing rates of particular particle decays with the equivalent anti-matter particle decays. The effects of CP violation can be examined through constraining the CKM quark mixing matrix and expressed in terms of the parameter angles on mixing relational unitarity triangles. B meson particles have a high number of decays corresponding to mixing parameters and are favourable for studies of the various forms of CP violation. Charmless hadronic decays are seen as important in these studies. Chapter three shows the outcome of the need for a large volume of data on B meson decays: a "B meson factory" producing millions of B mesons at the PEP-II electron-positron collider facility, and the dedicated BaBar particle detectors. The component arrangement and numerous considerations in the design of the detector are explained in this chapter. Chapter four describes the analysis techniques and considerations necessary for successful calculation of a decay branching ratio using the BaBar collaboration analysis software and datasets. Analysis procedure, successful selection criteria and the cut and count analysis method results for the particular channel  $B^+ \rightarrow \rho^0 \pi^+, \rho^0 \rightarrow \pi^+ \pi^-$  are presented in chapter five. These results give a branching decay ratio that agrees well with the PDG value although any implications arising from the asymmetry measurement appear to be inconclusive due to the effects of uncertainties. On a positive note BaBar is gathering data at a fast pace and the statistical uncertainties are being reduced to enable description of measurements with an ever-growing level of confidence, which in turn leads us ever closer to fulfilling the particle physicist's thirst for uncovering the subtle mechanisms responsible for the way that our universe evolves and endlessly continues to fascinate humankind.

## List of References

1. W. C. Haxton and B. R. Holstein, hep-ph/9905257 (1999)
2. P. F. Harrison and H. R. Quinn (Editors), The BaBar Physics Book: Physics at an Asymmetric B Factory SLAC-R-504 (1998)
3. J. W. Herb et al. Phys. Rev. Lett. 39 (1977)
4. K. Lingel et al., Penguin Decays of  $B$  Mesons, SLAC-PUB-7796 (1998)
5. R. Aleksan, Quark Mixing and CP Violation, <http://www.slac.stanford.edu/~roy/virgin.ps> (1998)
6. The CPLEAR Collaboration, Measurement of CP Violation Parameters and Test of CPT Invariance with  $K^0$  and  $\bar{K}^0$  at LEAR (1995)
7. C. S. Wu et al. Phys. Rev. 105, 1413 (1957)
8. J. H. Christenson et al. Phys. Rev. Lett. 13 (1964)
9. The NA48 Collaboration, A Precision Measurement of Direct CP Violation in the Decay of Neutral Kaons into Two Pions, Phys. Lett. B 544 (2002)
10. N. Cabibbo, Phys. Rev. Lett. 10 (1963)
11. M. Kobayashi and T. Maskawa, CP Violation in the renormalizable Theory of Weak Interactions, Prog. Theor. Phys. 49 (1973)
12. L. Wolfenstein, Phys. Rev. Lett. 51 (1983)
13. C. Jalskog, Phys. Rev. Lett. 55 (1985)
14. B. Renk, Status of the Cabibbo-Maskawa-Kobayashi Quark Mixing Matrix, 2002 Review of Particle Physics (2002)
15. Y. Grossman, Y. Nir, S. Plaszczynski, and M-H. Schune, review on  $B^0\bar{B}^0$  Mixing by H. Quinn, SLAC-PUB-7622, hep-ph/9709288 (1997)
16. The CDF Collaboration, Measurement of the  $B^0\bar{B}^0$  Oscillation Frequency using  $\pi - B$  Meson charge-flavor correlations in  $p\bar{p}$  collisions at  $\sqrt{s} = 1.8$  TeV, hep-ex/9712004 v1 (1997)
17. W. T. Ford, Measurements of  $\sin 2\beta$  in  $B$  decays, hep-ex/0309001 (2003)
18. Particle Data Group Particle Physics Booklet (2003)
19. W. T. Ford, Choice of Kinematic Variables in  $B$  Meson Reconstruction, BaBar Analysis

Document #53 Version 5

20. Blind Analysis Task Force, Draft Guidelines for Blind Analyses in BaBar, BaBar Analysis

Document #91 Version 2

21. E. Varnes et al., Measurements of the GoodTrackLoose Efficiency using SVT Tracks, BaBar

Analysis Document #157 Version 6

22. Tracking Efficiency Task Force,

<http://www.slac.stanford.edu/BFROOT/www/Physics/TrackEfficTaskForce/TrackingTaskForce>

23. G. Bellodi and P. Harrison, Detector charge bias using charged D decays, BaBar Analysis

Document #241 Version 1

24. G. Mancinelli and S. Spanier, Kaon Selection at the BaBar Experiment, BaBar Note #116

Version 1

25. D. Brown et al., The BaBar Track Fitting Algorithm,

[http://chep2000.pd.infn.it/long\\_p/lpa\\_a328.pdf](http://chep2000.pd.infn.it/long_p/lpa_a328.pdf)

26. H. Albrecht et al. / The Argus Collaboration, Exclusive Hadronic Decays of  $B$  Mesons, *Z.*

*Phys.* C48 (1990)

27. G. Mancinelli and S. Spanier, Kaon Selection at BaBar, BaBar Analysis Document 116

(2001)

28. C. Hearty, Measuring the Number of  $\Upsilon(4S)$  Mesons produced in Run 1, BaBar Analysis

Document #134 (2001)

29. T. J. Champion et al., Studies of Three-Body Charmless Hadronic  $B$  decays, BaBar Analysis

Document #36 Version 4 (2000)

30. BaBar Particle Identification Action Working Group,

<http://www.slac.stanford.edu/BFROOT/www/Physics/Tools/Pid/pid.html>